Multiscale Modeling of Silicon Heterojunction Solar Cells

by

Pradyumna Muralidharan

A Dissertation Presented in Partial Fulfillment
of the Requirements for the Degree
Doctor of Philosophy

Approved June 2019 by the
Graduate Supervisory Committee:

Dragica Vasileska, Co-Chair
Stephen M. Goodnick, Co-Chair
Christian Ringhofer
Christiana Honsberg

ARIZONA STATE UNIVERSITY

August 2019

ABSTRACT

Silicon photonic technology continues to dominate the solar industry driven by steady improvement in device and module efficiencies. Currently, the world record conversion efficiency (~26.6%) for single junction silicon solar cell technologies is held by silicon heterojunction (SHJ) solar cells based on hydrogenated amorphous silicon (a-Si:H) and crystalline silicon (c-Si). These solar cells utilize the concept of carrier selective contacts to improve device efficiencies. A carrier selective contact is designed to optimize the collection of majority carriers while blocking the collection of minority carriers. In the case of SHJ cells, a thin intrinsic a-Si:H layer provides crucial passivation between doped a-Si:H and the c-Si absorber that is required to create a high efficiency cell. There has been much debate regarding the role of the intrinsic a-Si:H passivation layer on the transport of photogenerated carriers, and its role in optimizing device performance. In this work, a multiscale model is presented which utilizes different simulation methodologies to study interfacial transport across the intrinsic a-Si:H/c-Si heterointerface and through the a-Si:H passivation layer. In particular, an ensemble Monte Carlo simulator was developed to study high field behavior of photogenerated carriers at the intrinsic a-Si:H/c-Si heterointerface, a kinetic Monte Carlo program was used to study transport of photogenerated carriers across the intrinsic a-Si:H passivation layer, and a drift-diffusion model was developed to model the behavior in the quasi-neutral regions of the solar cell. This work reports de-coupled and self-consistent simulations to fully understand the role and effect of transport across the a-Si:H passivation layer in silicon heterojunction solar cells, and relates this to overall solar cell device performance.

DEDICATION

To my ma

ACKNOWLEDGMENTS

There are many people that played significant roles for this dissertation to finally take a form that is vaguely coherent. Most importantly, I would like to thank my advisors Dr. Dragica Vasileska and Dr. Stephen M. Goodnick. The work presented in this dissertation would not have been possible without their guidance. I am indebted to them for all the mentorship and support that they provided down the years. Also, I would also like to thank Dr. Christiana Honsberg and Dr. Christian Ringhofer for being part of my PhD committee.

I deeply appreciate the funding that was provided by QESST (EEC-1041895) which supported most of the research presented in this dissertation. I would also like to thank Dr. Joseph Palais for awarding me graduate fellowships which provided financial support towards the end of my PhD.

I would like to express my gratitude towards Dr. Ashling Leilaeioun for reaching out to me and being the focal point for the contact resistivity project. Also, I would like to thank Will Weigand and Dr. Zachary Holman for the collaborative work on the contact resistivity project.

I would like to thank Dr. Kunal Ghosh for all the philosophical and scientific conversations regarding solar cell physics. I would like to thank Josh and Natasa for their invaluable feedback on my presentations, especially their strong opinions on color schemes.

I would like to thank all my colleagues in Dr. Vasileska's research group for all their input, suggestions, and brain storming sessions. In particular, I would like to express my gratitude to Da Guo and Yi Fang, with whom I shared some great times at various

conferences. I would like to thank Abdul Rawoof Shaik for many scientific discussions and brain storming sessions.

Finally, I will always be indebted to all my friends for all the support, advice and good times over the years. I would like to thank Dr. Raghuraj Hathwar and Dr. Sindhu Anand for all their advice on life in and after graduate school, Robin for all the adventures and laughs in the outdoors, Devina for always keeping my spirits high and telling me that it'll be alright, and Maha for making the end of graduate school enjoyable.

And finally, I would like to thank my mother, for pestering me to get out of bed and do something great.

TABLE OF CONTENTS

Page

LIST OF FIGURES x

CHAPTER

1. INTRODUCTION 1

1.1 Introduction to Solar Energy 1

1.2 Silicon Solar Cell Technologies 4

1.3 Introduction to Carrier Selective Contacts 6

1.4 This Work 10

2. DRIFT-DIFFUSION MODEL 15

2.1 Poisson's Equation 18

2.2 Band Offsets 21

2.3 Normalization and Scaling 22

2.4 Finite Difference Approach 22

2.5 Continuity Equation 23

2.6 Generation and Recombination Mechanisms 24

2.7 Gummel Iteration Scheme 25

2.8 Technology Computer Aided Design (TCAD) tools 26

2.9 Conclusion 27

3. CONTACT RESISTIVITY MODELING 28

3.1 Theoretical Model 31

3.1.1 Interface Physics 33

CHAPTER Page

3.1.2 TLM Theory 35

3.1.3 Recombination 36

3.1.4 Temperature 36

3.2 Results and Discussion 37

3.2.1 Variation of a-Si:H(i) Layer Thickness 37

3.2.2 Variation of Interface State Defect Density at the a-Si:H(i)/c-Si(p) Interface . 42

3.2.3 Variation of ITO Doping 43

3.2.4 Fill Factor Variation with Contact Resistivity 45

3.3 Conclusion 47

4. ENSEMBLE MONTE CARLO 51

4.1 Bandstructure 52

4.2 Acoustic Scattering 54

4.3 Non-Polar Optical Phonon Scattering 55

4.4 Selection of Final States 56

4.5 Drift Velocity 57

4.6 Theoretical Model 57

4.7 Results and Analysis 62

4.8 Conclusion 66

5. KINETIC MONTE CARLO 68

5.1 Defect Assisted Transport 71

CHAPTER Page

5.2 Band-Tail Defects 72

5.3 Mid Gap Defects 73

5.4 Initialization of the Carrier Distribution 74

5.4.1 Maxwellian Distribution 75

5.4.2 Gaussian Distribution 76

5.5 Transition Mechanisms 76

5.5.1 Tunneling 77

5.5.2 Elastic Injection and Emission from Traps 78

5.5.3 Inelastic Injection and Emission from traps 81

5.5.4 Defect to Defect 84

5.5.5 Poole Frenkel Emission 85

5.6 KMC Algorithm 86

5.6.1 Transition Table 87

5.6.2 Algorithm 90

5.7 Results and Discussion 92

5.7.1 Variation of a-Si:H(i) Layer Thickness 92

5.7.2 Injection and Extraction Analysis 96

5.7.3 Carrier Decay Simulations 98

5.7.4 Effect of the Band Tail Density of States 102

CHAPTER Page

5.7.5 Effect of the Optical Phonon Energy 104

5.7.6 Effect of Mid-Gap States and Interface Recombination 107

5.7 Conclusion 108

6. MULTISCALE MODELING 111

6.1 Drift-Diffusion Coupled with a Monte Carlo 114

6.1.1 Injection Boundary 115

6.1.2 Current Injection Boundary Conditions 116

6.1.3 Half Maxwellian Charge Injection 119

6.1.4 Extraction Boundary (placed at the contact) 119

6.1.5 Extraction Boundary (placed away from the contact) 120

6.1.6 Current Matching 121

6.1.7 Robin Boundary Conditions (RBC's) 121

6.1.8 Gummel Loop 123

6.1.9 Mesh 125

6.2 Results and Analysis 126

6.2.1 Collecting Boundary at the Contact 127

6.2.2 Weighted Carriers 138

6.2.3 Collecting Boundary Away from the Contact 139

6.3 Conclusion 143

CHAPTER Page

7. CONCLUSIONS AND FUTURE WORK 146

REFERENCES ……. 150

LIST OF FIGURES

Figure Page

1.1. Energy Consumption in the United States (Taken from www.eia.gov) …..…… 1

1.2. Renewable Energy Consumption in the United States (Taken from www.eia.gov) ... 2

1.3. Efficiency Chart for Various Technologies (Taken from www.nrel.gov) …...……... 3

1.4. Schematic Diagram of a Solar Cell. This Diagram Depicts the Collection of Photogenerated Electrons and Holes by Specialized Contacts …….…….. 7

2.1. Schematic Diagram of a Heterostructure ……...……. 21

2.2. Gummel Loop Flowchart for the Drift Diffusion Model …… 26

3.1. Schematic Diagram of a SHJ Solar Cell ……..……... 29

3.2. Schematic Diagram of a TLM Pattern for a SHJ Solar Cell …..……..... 32

3.3. Simulated Equilibrium Band Diagram of the a-Si:H(i)/c-Si Interface …….. 34

3.4. Simulated Equilibrium Band Diagram of the ITO(n+)/a-Si:H(p) Heterointerface. (Inset) A Zoomed in Look at the Heterointerface where Band to Band Tunneling Occurs ……..….. 35

3.5. a) Simulated *I-V* Curve Obtained by Conducting a Voltage Sweep for a Pair of Contacts. b) Simulated Total Resistance (Slope of *I-V* Curve in Fig. 4a) vs. Contact Pad Spacing ……..….... 37

3.6. a) Simulated Contact Resistivity vs. a-Si:H(i) Layer Thickness where the ITO is Treated as a Schottky Contact (dashed green lines) and as a Semiconductor (Solid Blue Line) b) Simulated (Blue) and Experimental (Red) Contact Resistivity vs. a-Si:H(i) Thickness …….…. 40

Figure Page

3.7. Simulated Contact Resistivity for Different a-Si:H(i) Layer Thicknesses vs. a-Si:H(p) Layer Doping ……..……..……... 41

3.8. a) Simulated Contact Resistivity (Red Lines) vs. a-Si:H(i) Layer Thickness at Different Temperatures. b) Simulated Contact Resistivity (Blue Lines) and Experimental Contact Resistivity (Red Line) vs. Temperature for a a-Si:H(i) Layer Thickness = 8 nm. Simulated Results Treat the ITO as a Semiconductor ……..... 42

3.9. Simulated Contact Resistivities for Different Interface State Defect Densities at the a-Si:H(i)/c-Si(p) Heterointerface vs. a-Si:H(i) Layer Thickness ……..……..... 43

3.10. Simulated Contact Resistivity vs. ITO Doping. The Simulated Results Treat the ITO as a Semiconductor …….…….. 44

3.11. a) Equilibrium Energy Band Diagram at the ITO(n^+)/a-Si:H(p) Junction for an ITO(n^+) Doping = 10^{18} cm^{-3}, ϕ_{ITO} = 4.5 eV. b) Equilibrium Energy Band Diagram at the ITO(n^+)/a-Si:H(p) Junction for a ITO(n^+) Doping = 10^{21} cm^{-3}, ϕ_{ITO} = 4.32 eV. (Inset) A Close Up of the ITO(n^+)/a-Si:H(p) Heterointerface ……..……..... 46

3.12. a) Simulated Contact Resistivities for Different Interface State Defect Densities at the a-Si:H(i)/c-Si(p) Hetero-interface vs. a-Si:H(i) Layer Thickness. b) Simulated Fill Factor (for Different Interface State Defect Densities) vs. a-Si:H(i) Layer Thickness …….……. 47

Figure Page

4.1. Schematic Diagram for Three Band Model for the Valence Band ……..…….. 53

4.2. a) Schematic Diagram of SHJ Solar Cell with the Simulation Domains. The EMC Solution is Applied in the c-Si Region Near the a-Si:H(i)/c-Si Heterointerface. b) Simulated Band Diagram at Maximum Power Point ~ 0.65 V …….…….. 58

4.3. Electric Field at the Front Contact for a Strongly Inverted a-Si:H(i)/c-Si Heterointerface in a SHJ Solar Cell at Maximum Power Point Voltage ~ 0.65 V ……..... 59

4.4. Flow of Information Between the Drift-Diffusion Solver and the EMC Solver. Also Shown in this Figure are the Corresponding Physical Processes Incorporated in the Theoretical Models of the Corresponding Solvers ……..…. 60

4.5. Visualization of the Boundary Conditions of the EMC Domain …..……...……... 61

4.6. Ensemble Monte Carlo Simulation Results for Warped Non-Parabolic Bands: a) Velocity vs. Time for Different Electric Fields. b) Population of Carriers in Each Band …….…… 62

4.7. Energy Distribution Function of Photogenerated Carriers at the a-Si:H(i)/c-Si Heterointerface for an Interface State Defect Density of a) 10^{10} cm^{-2}, b) and c) $>10^{11}$ cm^{-2} …… 64

4.8. a) EDF of the Photogenerated Carriers at the Heterointerface for a Weakly Inverted Device. b) EDF in the Quasi-Neutral Region ……..... 65

4.9. a) EDF Using the Three-Band Approach. b) EDF Using a Single Parabolic Band Approach .....…….... 66

Figure Page

5.1. a) Schematic Diagram of the SHJ Solar Cell Indicating the Drift-Diffusion and KMC Simulation Domains and b) the Energy Band Diagram of a SHJ Solar Cell at Equilibrium at the Front Contact ……...……..... 71

5.2. Density of Mid Gap States Calculated by the Defect-Pool Model (Implemented in Matlab). a) Density of Defect States in Intrinsic Amorphous Silicon. b) Density of Defect States in n-type Silicon ……...……...…….……... 74

5.3. Schematic Diagram of the Various Transport Mechanisms that Assist the Photogenerated Holes Across the Barrier Layer. We Consider Multi-Phonon Injection (MPI) for Transitions into the *a*-Si:H(*i*) Passivation Layer, Defect to Defect (Hopping) Mechanisms for Transport Within the Layer, and Poole-Frenkel and Multi-Phonon Defect Emission for Emission from the Layer ……..…… 76

5.4. Transmission Coefficient Across a Piecewise Linear Barrier Calculated by the WKB Method and Transfer Matrix Method ….……... 78

5.5. Elastic Tunneling from Conduction Band to Defect Level …...……...….. 79

5.6. Wavefunction Description of Elastic Tunneling …….……...……..... 80

5.7. Injection and Extraction of Carriers via Multi-Phonon Tunneling …...……. 82

5.8. a) Elastic Defect to Defect Transition. b) Inelastic Defect to Defect Transition …..... 85

5.9. Barrier Lowering Due to High Fields in the Poole-Frenkel Mechanism ……..... 87

5.10. Schematic Diagram of the Transition Tables for Selecting the Final Mechanism for (a) Multi-Phonon Injection, and (b) Extraction Mechanisms which Include Poole-Frenkel Emission, Thermionic Emission, Direct Tunneling and Defect Emission ….……... 89

Figure Page

5.11. Flow of Information Between the Drift-Diffusion Solver and the KMC Solver. Also Shown in this Figure are the Corresponding Physical Processes Incorporated in the Theoretical Models of the Corresponding Solvers ……..……... 91

5.12. Maximum Power Point vs. a-Si:H(i) Layer Thickness for a High Fill Factor and Low Fill Factor Device ……. 94

5.13. Average Transit Time (τ) for the Photogenerated Holes to Cross the a-Si:H(i) Barrier Layer vs. a-Si:H(i) Layer Thickness ……. 94

5.14. Electric Field (V/m) at the a-Si:H(i)/c-Si Heterointerface vs. a-Si:H(i) Layer Thickness …...……... 95

5.15. Percentage of Phonons Required for Injection into the a-Si:H(i) Layer vs. a-Si:H(i) Layer Thickness for a) High Fill Factor Device and b) Low Fill Factor Device …...….. 96

5.16. Percentage of Poole-Frenkel (Solid Lines) and Multi-Phonon Defect Emission (Dashed Lines) as Extraction Mechanisms vs. a-Si:H(i) Layer Thickness for a High Fill Factor (Black) and Low Fill Factor Device (Red) ……...…….. 97

5.17. Carrier Decay of a Normalized Carrier Population of Holes at the a-Si:H(i)/c-Si Heterointerface for Different a-Si:H(i) Thicknesses vs. Time …...……... 99

5.18. Carrier Decay of a Normalized Carrier Population of Holes at the a-Si:H(i)/c-Si Heterointerface Various Temperatures vs. Time …...……. 100

5.19. Average Transit Time of Photogenerated Holes Across a 10nm Thick a-Si:H(i) Layer vs. Average Carrier Energy of Photogenerated Holes ……...…….. 101

Figure Page

5.20. Carrier Decay of a Normalized Carrier Population of Holes at the a-Si:H(i)/c-Si Heterointerface for Different Average Carrier Energies for Photogenerated Holes vs. Time ……...…. 101

5.21. Transit Time vs. Characteristic Decay Energy (E_{vt}) for a 10 nm *a*-Si:H(*i*) Passivation Layer ……... 103

5.22. Defect Energy Space in the *a*-Si:H(*i*) Passivation Layer for an E_{vt} of a) 20 meV and b) 80 meV ……... 104

5.23. Transit Time vs. Optical Phonon Energy for a 10 nm *a*-Si:H(*i*) Passivation Layer ……... 105

5.24. Tracking Carriers Through a 10 nm a-Si:H(i) Passivation Layer ……...…..... 106

5.25. The KMC Domain (i-aSi) with Localized and Mid Gap States …..……...……..... 107

6.1. Schematic Diagram of the Hierarchy of Simulation Models. The Boxes Shaded in Green (Monte Carlo and Drift-Diffusion) are Coupled to Form a Relatively Accurate and Computationally Efficient Solution to a High Field Transport Problem ……..... 112

6.2. Visualization of the Interaction of the Three Solvers in a Multiscale Framework ….113

6.3. Schematic Diagram Describing the Coupling of the Drift-Diffusion and EMC Solver …….. 114

6.4. Visualization of the Simulation Domains in SHJ Solar Cell. The EMC Domain that Operates at the Heterointerface (Red) must be Coupled to the Drift-Diffusion Domain in the Low Field Regions (green) ……...……. 116

6.5. Visualization of the MC Domain …….……. 119

Figure Page

6.6. Visualization of MC Domain where the Collecting Boundary is Placed Away from the Contact …… 120

6.7. Flowchart Describing How to Current Match a MC Solver to a Drift-Diffusion Solver …….. 122

6.8. Visualization of the Coupled DDMC Solution, where the Continuity Equation Solves (Green) for Charge Density Outside the EMC Domain (Red) and Poisson's Equation is Solved Over the Entire Device Domain. C_1 and C_2 are the Contacts of the Device, and B_1 and B_2 are the Shared Boundaries of the Drift-Diffusion and EMC Domains ……. 123

6.9. Flow Chart of the Gummel Loop Employed by the Multiscale Solver ……. 125

6.10. A *pn* Junction Test Structure to Study the Coupling of the Drift-Diffusion and EMC Solvers where: a) the EMC Extraction Boundary is Placed at the Contact, and b) the EMC Extraction Boundary is Placed Away from the Contact …….. 126

6.11. Charge Density Profile of the Test Structure Under a 1000 Suns Illumination 127

6.12. Electron and Hole Current Density Profile. The Dashed Line Indicates the Monte Carlo/Drift-Diffusion Boundary ……..... 128

6.13. Cell Population for Every Cell in the Monte Carlo Domain ……... 129

6.14. EMC Charge Characteristics Corresponding to an Injection of 100 mA/cm^2. a) Cumulative Charge Extracted at the Front Contact vs. Time. b) Total Charge Density in the EMC Domain vs. Time. c) Flux Extracted at the Front Contact per Δt (0.2 Femto Seconds) vs. Time ……..……..... 130

Figure Page

6.15. EMC Characteristics for an Injection Level of 50 mA/cm^2. a) Cumulative Charge Extracted at the Front Contact vs. Time. b) Total Charge Present in the EMC Domain vs. Time ……...…. 131

6.16. A Moving Average Filter can be Applied to the Noisy Cumulative Charge Data. a) Cumulative Charge vs. Time after Using a Moving Average Filter …..…….. 132

6.17. Charge Density Profile Given by the Self-Consistent DDEMC Solver ……...….... 133

6.18. a) Total Current Density Profile Calculated by Drift-Diffusion. b) Total Current Density Profile Calculated by the DDMC …..……. 135

6.19. a) Electron and Hole Current Density Calculated by Drift-Diffusion. b) Electron and Hole Density Calculated by the DDEMC (from the Edge of the DDEMC Window) …. 136

6.20. Hole Current Density Injected into the EMC Domain vs. Gummel Index (The Index on the x Scale Represents the i^{th} Iteration of the Gummel Loop) ……..... 137

6.21. a) Cumulative Charge Density vs. Time for i^{th} Gummel Cycle. b) Total Charge in the Monte Carlo Domain vs. Time for i^{th} Gummel Cycle ……. 137

6.22. Visualization of Charge Enhancement in Regions with Low Charge Density …... 138

6.23. Cumulative Charge (a) and Total Device Charge (a) vs. Time when the Collecting Boundary is Placed Away from the Contact ….……... 139

6.24. Hole Injection Current vs. i^{th} Gummel Iteration ……. 140

6.25. Charge Density Profile Using a Collecting Boundary Placed Away from the Contact. The Monte Carlo Domain Lies Between the Black Dashed Lines, Whereas the Green Circles Indicate the Drift-Diffusion Regions ……...……... 140

Figure Page

6.26. Band Diagram at the Front Contact of a SHJ Under Short Circuit Conditions as Calculated by the Drift-Diffusion Solver. The Figure also Indicates the Region in Which the EMC is Implemented ……..……... 141

6.27. a) Hole Charge Density as Calculated by the Drift-Diffusion (Blue) and DDEMC (Red). b) Hole Current (Red) and Electron Current (Blue) as Calculated by the DDEMC ……..142

CHAPTER 1

INTRODUCTION

1.1 Introduction to Solar Energy

With the continuous increase in population and growth in industry, the world's energy needs continue to rise. This rise puts an enormous strain on all primary sources of energy such as petroleum, natural gas, coal, nuclear, and renewable energy to meet the world's energy demands. In 2017, the total energy produced in the United States was ~ 87.5 quadrillion British thermal units (btu); of which 77.6% was produced by fossil fuels, and 12.7% was produced by renewable energy (shown in Fig 1.1).

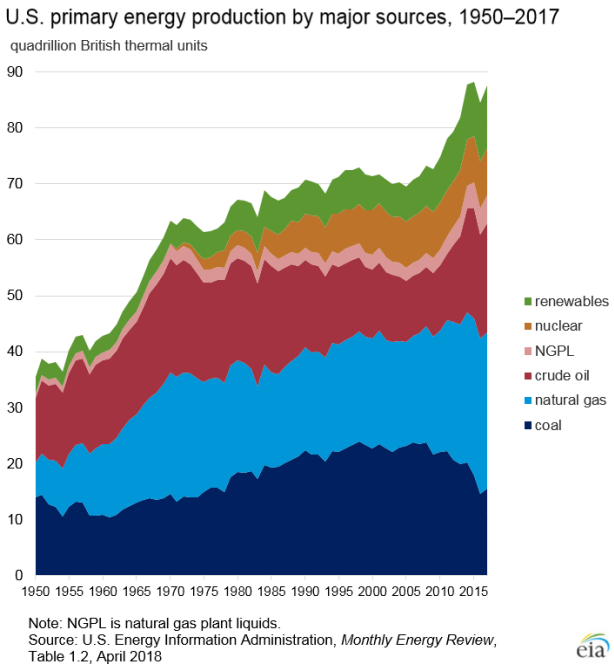

Figure 1.1. Energy consumption in the United States (taken from www.eia.gov).

The extensive use of conventional sources such as petroleum, natural gas and coal, and its effect on the environment has created a global conversation about alternative sources of energy. In recent times there has been a conscious effort by the world at large to create and consume a cleaner form of energy. In 2017, consumption of energy from renewable sources was 11% of the total energy consumed (see Fig. 1.2), of which the energy consumed from solar resources was only 6% of the total energy consumed from renewable sources.

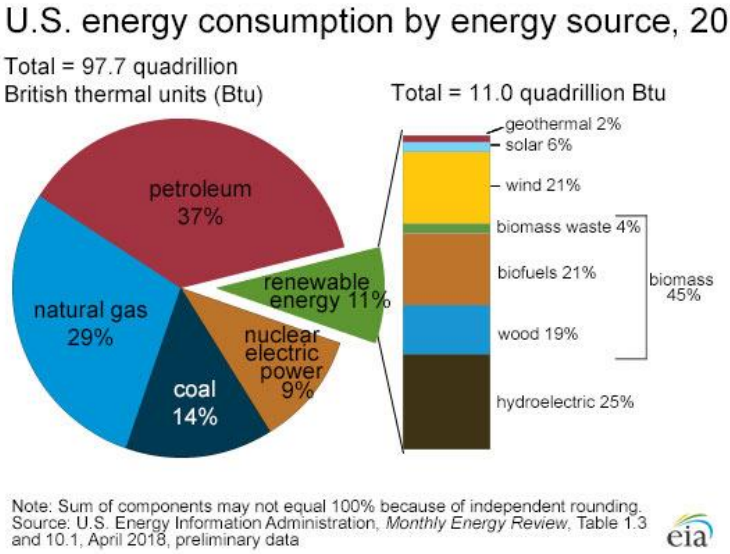

Figure 1.2. Renewable energy consumption in the United States (taken from www.eia.gov).

Solar energy is predominantly produced by utilizing the concept of photovoltaic cells. A photovoltaic cell, more commonly known as a solar cell, utilizes the photoelectric effect to generate current. The photoelectric effect, proposed by Albert Einstein in 1905, theorized that the absorption of light (photons) by a material leads to the emission of photogenerated electrons [1]. If harvested correctly, these photogenerated electrons can be converted into current. Historically, the first practical silicon solar cell was demonstrated

by Bell Labs in 1954 [2]. These solar cells used were based on silicon (Si) *pn* junctions. Most first-generation designs of solar cells are based on semiconductor *pn* junctions. Briefly, when light shines upon a semiconducting material, the photons which have an energy larger than the bandgap are absorbed. These photons can then dislodge electrons from the lattice to create free carriers (electrons and holes). Traditionally, a built-in electric field is used to collect the photogenerated carriers. The built-in electric field is created by introducing impurities (doping) into the material.

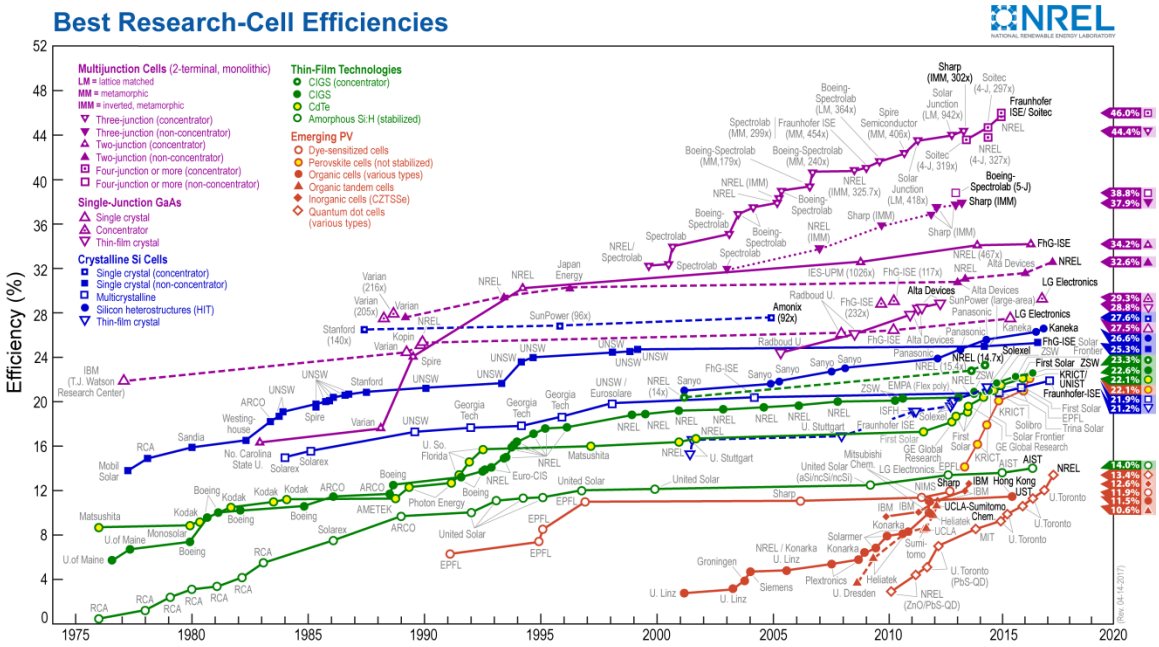

Figure 1.3. Efficiency chart for various technologies (taken from www.nrel.gov).

Over the past decade, there has been tremendous effort to not only develop new solar technologies but also to maximize the efficiency of existing technologies. Figure 1.3 (NREL efficiency chart) shows the increase in efficiencies for various solar cell technologies. It is evident that many different material systems have been explored in order to obtain high efficiency solar cells.

1.2 Silicon Solar Cell Technologies

Solar cells based on crystalline silicon currently hold a very strong presence in the photovoltaic industry with global market share over 90%. The use of crystalline silicon as a photo-absorber has some inherent advantages, i.e. it is stable, abundant and very well understood. Previously, the microelectronics industry spent decades after the invention of the transistor to understand the properties of silicon. Consequently, solar cells based on silicon can reap the benefits of the lessons learnt by the microelectronics industry. In general, crystalline silicon solar cells generate power by absorbing sunlight, generating electron hole pairs, and collecting the photogenerated carriers. According to the Shockley-Queisser limit based on the detail-balanced theory, a single junction solar cell limited by radiative recombination can achieve a maximum conversion efficiency ~ 33 % for the AM1.5 spectrum [3]. However, since crystalline silicon is an indirect bandgap material, it is limited by Auger recombination and theoretical predictions suggest that it can achieve a maximum conversion efficiency ~ 29.43% [4]. Therefore, the goal of creating novel device structures using crystalline silicon is to obtain or exceed the theoretical efficiency. There are several unique device structures that have led to high efficiency silicon solar cell technologies, such as the passivated rear emitter cell (PERC), which was developed by Green et al. at UNSW [5]. This structure optimizes the passivation of the rear contact, which improves the electrical properties and thus the overall conversion efficiency. PERC technology is highly compatible with existing PV production lines, and thus is a staple high efficiency silicon solar cell technology. Currently in 2019, LONGi solar holds the world record device conversion efficiency for PERC technology with an efficiency ~ 24.06%

with a bifacial monocrystalline silicon solar cell. The passivated emitter, rear locally diffused (PERL) structure is another high efficiency silicon technology which purportedly offers benefits over the PERC structure by using boron diffusions under the contact areas [6].

To further maximize photogenerated carrier collection and improve device efficiencies, passivating and carriers selective contact structures are being utilized. These structures generally tend to use heterostructures to optimize collection of photogenerated electrons and holes, and utilize passivation layers in order to reduce recombination at heterointerfaces. One such technology is the tunnel oxide passivated contact (TOPCon) technology which uses ultrathin SiO_x layers on top of highly doped silicon to achieve passivation and selectivity; these cells consistently achieve high efficiencies [7]. Another relevant technology that utilizes the carrier selectivity and passivation concept is the silicon heterojunction solar cell technology, which is also the primary focus of this thesis. This technology was pioneered by Sanyo in the early 1990's as the heterojunction with intrinsic thin layer (HIT) [8] cell, which used amorphous silicon layers on a crystalline silicon photo-absorbers. Since the early days, this technology has consistently delivered high efficiency single junction cells (>20%). In 2014, Panasonic reported world record efficiencies for their HIT technology with 24.7% and 25.6% [9,10]. Currently, the world record efficiency for this technology is held by Kaneka with an efficiency of 26.7% [11]. Liu et al. provides a good overview of the various silicon solar cell technologies [12].

1.3 Introduction to Carrier-Selective Contacts

It is imperative to minimize all sources of recombination to achieve a high efficiency solar cell. Considering that the bulk lifetime of crystalline silicon wafers has improved continuously over the last few years, a limiting loss mechanism that degrades solar cell performance is recombination at the contacts and surfaces. Popular silicon homojunction cell technologies such as PERC, PERL etc. minimize the losses due to recombination at the contact by reducing direct contact between the crystalline silicon and the metal, while the non-contacted area is passivated with a dielectric layer. However, such a strategy increases the process complexity; also, lateral transport becomes crucial in determining the overall performance. Glunz *et al.* have previously shown that there is a trade-off between open-circuit voltage (V_{oc}) and fill factor (FF) due to resistive losses that are induced by lateral transport [13].

Figure 1.4 shows a schematic diagram of a solar cell interacting with light. The incident light on the solar cell creates electron-hole pairs in the absorber layer. In a traditional solar cell architecture, the built-in electric field of the solar cell separates the photogenerated electrons and holes, which are then collected by the contacts. The photogenerated carriers can be lost due to recombination in the absorber layer or at the contacts. As mentioned earlier, the high lifetime (~ ms) crystalline silicon wafers facilitate a large diffusion length, which ensures that photogenerated carriers can reach the contact. However, recombination at the contacts can be a major factor in the degradation of solar cell performance. The reduction of recombination at the contacts enables the solar cell to support a higher photogenerated carrier population, and thereby a higher quasi-fermi level separation. The

quasi-fermi level separation is an indication of the open-circuit voltage of the solar cell. Kerr *et al.* have previously shown that, assuming all the photons can be trapped in a thin silicon wafer, thinning a silicon wafer from 200 μm to 20 μm can lead to an increase in open-circuit voltage from 750 mV to 790 mV [14].

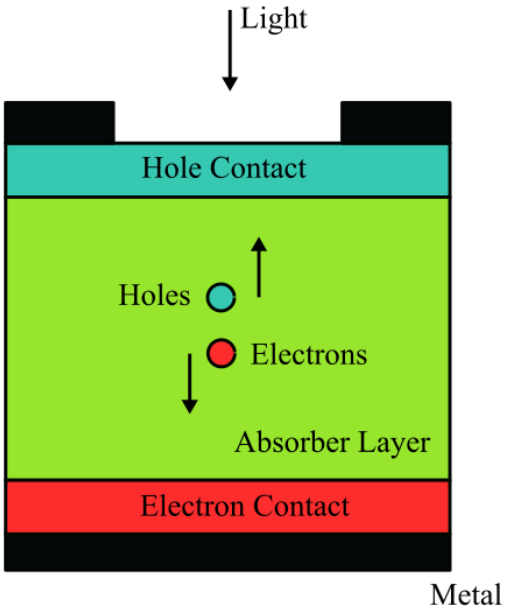

Figure 1.4. Schematic diagram of a solar cell. This diagram depicts the collection of photogenerated electrons and holes by specialized contacts.

Modern solar cell architectures utilize passivating contacts to reduce recombination losses at the contact [15]. Passivating contacts are material structures that are placed on top of crystalline silicon (or any other absorber layer) which effectively suppresses carrier recombination. Ideally, a passivating contact not only suppresses recombination, but also facilitates efficient extraction of photogenerated carriers. Contacts to silicon solar cells can be quantitatively characterized by considering two parameters. Firstly, the recombination

current density 'J_0', which is a measure of the current in the solar cell due to recombination processes. Cuevas *et al.* have previously studied the true meaning of the J_0 parameter under equilibrium and under non-equilibrium condition (i.e. illumination) [16]. Secondly, the contact resistivity 'ρ_c' describes the resistive losses associated with the contact to the solar cell. In crystalline silicon solar cell technology, trade-offs between J_0 and ρ_c are often made in order to obtain high efficiency solar cell designs. A pertinent example of this type of trade-off is the contact structure used in PERC cells, where the contact area is reduced to compensate for a relatively high J_0 [17].

As mentioned above, reducing losses due to recombination is an effective strategy to enhance the performance of solar cells. In particular, passivation schemes aim to suppress minority carrier recombination. It is important to note that solar cells generate power by collecting majority carriers. The recombination current density (J_0) is a measure of minority carrier recombination which not only depends on the defect state densities, but also on the conductivity of minority carriers. On the other hand, ρ_c is directly related to conductivity, i.e. a higher conductivity of carriers will lead to lower ρ_c's. Therefore, to create an efficient charge collecting contact with low J_0 and ρ_c, it is imperative to improve passivation while also creating asymmetry in the conductivities of the majority and the minority carriers. The asymmetry in conductivities or charge transport conditions of majority and minority carriers defines the selectivity of the contact. Electron selective contacts are contacts that collect electrons as majority carriers; they have a high electron conductivity and low hole conductivity. Hole contacts are vice versa. Therefore, carrier selective contacts are also specifically referred to as electron and hole contacts. Cuevas *et al.* have previously

explained the necessity and considerations required to create specialized contacts for solar cells [18].

There are several strategies that have been implemented to achieve selectivity. For homojunction technologies, selectivity is achieved by heavily doping the contact layers. Heavy doping reduces the minority carrier concentration and consequently reduces the conductivity, as σ (conductivity) = q (charge) $\times$ μ (mobility) $\times$ n (carrier concentration). The J_0 is reduced due to the low minority carrier concentration and ρ_c is reduced due to high majority carrier conductivity (and concentration). Another approach to induce selectivity is by using a high or low workfunction metal (oxide) on the absorber layer to modulate surface carrier concentrations.

The formation of a heterojunction between the crystalline silicon absorber and a wide bandgap material can be used to from carrier-selective contact that offers multiple levels of selectivity. The wide bandgap layer is very effective in reducing minority carrier conductivity as it strongly suppresses minority carrier concentration. In theory, the formation of a heterojunction can also offer another level of selectivity by creating favorable band offsets, i.e. a potential barrier for minority carriers and no potential barrier for majority carriers. For the purposes of silicon heterojunction solar cells (which is the main focus of this dissertation), layers of doped and intrinsic hydrogenated amorphous silicon are placed on the crystalline silicon absorber to form the carrier selective contact [19]. The hydrogenated amorphous silicon has a wider bandgap (~1.7 eV) than the crystalline silicon (~1.12 eV) and therefore can reduce minority carrier conductivity. The formation of the heterojunction between p-type doped amorphous silicon and n-type

crystalline silicon leads to sharp band bending in the n-type crystalline silicon. This band bending leads to the heterointerface to be strongly inverted, i.e. the concentration of minority carrier holes ≫ the concentration of the majority carrier electrons. The strongly inverted nature of this heterointerface and its effect on the performance of the silicon heterojunction solar cell will be discussed at various points in this dissertation. Finally, selectivity can also be achieved by introducing a thin dielectric layer (like SiO_x) which presents asymmetrical tunneling probabilities for the carriers [20].

The use of carrier-selective contact structures can be used to further optimize solar cell designs for maximizing device performance. As mentioned earlier in this section, the reduction of J_0 can lead to a gain in V_{oc}, and a reduction in ρ_c can maximize the FF of the solar cell. However, the design of solar cells must also consider optical constraints. Therefore, the design of the carrier-selective contacts will involve tradeoffs in terms of doping and thickness of layers to ensure that the contact is optically transparent while ensuring efficient carrier extraction.

1.4 This Work

In this work, silicon heterojunction (SHJ) solar cell structures consisting of hydrogenated amorphous silicon (a-Si:H) and crystalline silicon (c-Si) are considered. These cells use specialized structures known as carrier-selective contacts to maximize the collection of photogenerated carriers. In the case of SHJ solar cells, the carrier-selective contact consists of doped (p or n type) hydrogenated amorphous silicon [a-Si:H(p/n)] and intrinsic hydrogenated amorphous silicon [a-Si:H(i)] on a c-Si absorber. This structure is designed to selectively collect electrons or holes; hence the carrier-selective contact is often

also known as an electron or hole contact. The a-Si:H(i) layer is a crucial component in this structure as it passivates defect states at the a-Si:H/c-Si heterointerface, which also improves the selectivity of the contact and is instrumental in achieving high open circuit voltages (V_{OC}'s) [21]. Thus far, there have not been many detailed studies that rigorously study the effect of the a-Si:H(i) passivation layer on the transport of photogenerated carriers. In this work, the transport and collection of photogenerated holes through the hole contact in a SHJ solar cell structure is studied. In particular, the effect of the a-Si:H(i)/c-Si heterointerface and the a-Si:H(i) passivation layer on transport of photogenerated holes is analyzed.

The novel structure of the SHJ solar cell introduces several complications in terms of understanding the transport of photogenerated carriers. The presence of high electric fields at the a-Si:H(i)/c-Si heterointerface affects the energy distribution function (EDF) of photogenerated carriers which leads to deviations from equilibrium assumptions. Also, there has been considerable debate on the role of defect assisted transport of photogenerated holes across the a-Si:H(i) passivation layer. There have been some studies in the literature that have attempted to investigate this issue, however, thus far no rigorous analysis has been undertaken to understand the role of microscopic physical mechanisms that assist photogenerated carrier collection in the SHJ structure. Simulation studies often employ the drift-diffusion model to study the electrical characteristics of solar cells. This is an efficient and accurate approach if the transport is near equilibrium; thus, quantum and non-semi-classical effects may be neglected. However, modern solar cells utilize novel device structures and new materials that lead to scenarios where the physics of transport is

no longer truly near-equilibrium. In the case of SHJ solar cells there are two crucial regions that require a detailed analysis. Firstly, the high field region at the a-Si:H(i)/c-Si heterointerface which is ~ 100 nm's and can affect the energy distribution function of the photogenerated carriers at the interface. Traditionally, high field transport is described by scattering properties of the bulk material which is of the order of $10^{-15} \rightarrow 10^{-12}$ seconds. Secondly, the a-Si:H(i) passivation layer, carrier transport through this layer involves defect assisted transport. This layer is only a few nm's thick, where the transport is limited by defect capture and emission, which is of the order of $10^{-9} \rightarrow 10^{-3}$ seconds. A single theoretical framework is unable to provide resolution on the physics of transport due to the vast variation in length and times scales of the limiting physical mechanisms.

In this work, a multiscale simulation methodology is presented that rigorously studies transport and device behavior of the solar cell. The multiscale solver operates on three primary domains: 1) The drift-diffusion domain in the low field regions of the device. The drift-diffusion model is coupled to a global Poisson solver which calculates the electric fields and potentials in the device, 2) The ensemble Monte Carlo (EMC) domain, which describes transport in the high electric field region at the a-Si:H(i)/c-Si heterointerface. Theoretical models used by commercial simulators usually ignore the non-Maxwellian behavior of carriers under high fields, and lastly, 3) a KMC domain which describes defect assisted transport carriers through the a-Si:H(i) layer. Simulations conducted using commercial TCAD tools (Silvaco) are also used to supplement work presented in this thesis. The research work presented in this thesis offers a unique perspective and understanding of transport in a SHJ solar cell.

In Chapter 2, the drift-diffusion model is introduced. In particular, the derivation and the numerical implementation of the drift-diffusion method using finite difference methods is discussed. Also, the limitations of this approach are highlighted to set the stage for the need of advanced modeling approaches discussed in subsequent chapters.

In Chapter 3, drift-diffusion modeling (using Silvaco) is used to study the contact resistivity behavior in hole contacts of SHJ solar cells. This is done by simulating the transmission line measurement experiment. The simulations and experimental results presented in this chapter help in the understanding of the considerations that must be made to optimize the various layers of the hole contact of a SHJ solar cell to maximize device performance.

In Chapter 4, the ensemble Monte Carlo method is applied to study the energy distribution function of photogenerated carriers at the a-Si:H(i)/c-Si heterointerface. The results presented in this chapter illustrate that high field behavior leads to conditions that cannot be described by low-field semi-classical physics.

In Chapter 5, the kinetic Monte Carlo method is applied to study defect assisted transport of photogenerated carriers through the a-Si:H(i) passivation layer. Also described here are the various physical mechanisms that are involved in the transport of photogenerated carrier across the a-Si:H(i)/c-Si heterointerface. The results presented in this chapter describe the conditions that are required for efficient transport of photogenerated holes across the a-Si:H(i)/c-Si heterointerface and the a-Si:H(i) passivation layer.

In Chapter 6, a strategy to self-consistently couple the drift-diffusion and ensemble Monte Carlo solvers is outlined. The results presented in this chapter depict the various challenges and strategies involved in coupling a drift-diffusion and an ensemble Monte Carlo solver for a bipolar device, i.e. a solar cell.

In Chapter 7, a summary of conclusions is presented pertaining to the various methodologies that were used to analyze transport in a silicon heterojunction solar cell. Also, several strategies are suggested to improve and extend the capabilities of the numerical simulators that have been developed as part of this dissertation.

CHAPTER 2

DRIFT-DIFFUSION MODEL

A cornerstone of semi-classical transport theory is the Boltzmann transport equation (BTE), which for parabolic bands is given by

$$\frac{df}{dt} + v.\nabla_r f + \frac{qE}{\hbar}.\nabla_k f = \sum_{k'} \begin{Bmatrix} S(k',k)\, f(r,k',t)\left[1 - f(r,k,t)\right] \\ -S(k,k')\, f(r,k,t)\left[1 - f(r,k',t)\right] \end{Bmatrix} \tag{2.1}$$

where f is the distribution function which gives the probability of occupancy of a state (r,k,t), v is the group velocity, and E is the electric field. The LHS of Eq. 2.1 describes the evolution of the distribution function. The first term describes the time-dependent change of the distribution function, the second term describes the change in the distribution function due to spatial variation, and the third term describes the change in the distribution function due to internal and external electric fields. The right hand side of the equation tells us how collision terms that describes scattering events change the distribution function; $S(k,k')$ describes the transition probability from state k → k' and $[1-f(k',t)]$ is the probability of the state k' being unoccupied.

Even with continuous improvement in computational platforms and mathematical methods, the direct numerical solution of the full 3D BTE can be computationally extremely expensive, as it is a 7-dimensional (3 in momentum, 3 in space and 1 in time) equation in nature. Therefore, it is not uncommon for many device simulators to use approximate solutions that are then coupled to Poisson's equation for self-consistency.

For simplicity, the 1D BTE is considered in Eq. 2.2, which can be simplified to a certain extent by utilizing the relaxation time approximation [22]. In steady state it leads to

$$\frac{qE}{m^*}\frac{df}{dv}+v\frac{df}{dx}=\frac{f_0-f(v,x)}{\tau} \tag{2.2}$$

where q is the elementary charge, m^* is the effective mass and f_0 is the equilibrium distribution function. Equation 2.2 assumes a parabolic bandstructure ($m^*v=\hbar k$).

Various transport models that can be derived from the BTE utilize "moments" of the BTE. Let us consider the first moment of the BTE by multiplying Eq. 2.2 with v (velocity) and integrating

$$\int v\frac{qE}{m^*}\frac{df}{dv}dv+\int v^2\frac{df}{dx}dv=\int v\left(\frac{f_0-f}{\tau}\right)dv \tag{2.3}$$

The current density can be given by

$$J(x)=q\int v\ f(v,x)\,dv \tag{2.4}$$

The RHS of Eq. 2.3 can also be written as

$$\frac{1}{\tau}\left[\int v\ f_0 dv-\int v\ f(v,x)\,dv\right]=-\frac{J(x)}{q\tau} \tag{2.5}$$

By using Eq. 2.5 into Eq. 2.3 we get

$$J(x)=-q\frac{q\tau}{m^*}E\int v\frac{df}{dv}dv-q\tau\int v^2\frac{df}{dx}dv \tag{2.6}$$

We evaluate the integral for the first term on the RHS by using integration by parts to get

$$\int v\frac{df}{dv}dv=v\ f\Big|_{-\infty}^{\infty}-\int f(v,x)\,dv \tag{2.7}$$

As the distribution function is zero for v going to plus or minus infinity, the first term is zero and the second term gives us electron density $n(x)$.

$$\int f(v,x)\,dv=n(x) \tag{2.8}$$

The second term in Eq. 2.6 can be given by

$$\frac{d}{dx}\int v^2 f\left(v,x\right)dv = n(x)\left\langle v^2 \right\rangle \tag{2.9}$$

Now Eq. 2.6 can be written as

$$J\left(x\right) = q\left(\frac{q\tau}{m^*}\right)En\left(x\right) - q\tau\frac{dn\left(x\right)}{dx}\left\langle v^2 \right\rangle \tag{2.10}$$

The drift diffusion equation is obtained by introducing a mobility 'μ', a diffusion coefficient 'D' (Eq. 2.11), assuming low-field transport conditions and using the Einstein's relation (Eq. 2.12).

$$\mu = \frac{q\tau}{m^*}; \qquad \left\langle v^2 \right\rangle = \frac{k_B T}{m^*} \tag{2.11}$$

$$\frac{D}{\mu} = \frac{k_B T}{q} \tag{2.12}$$

Thus, we obtain the current density equation for electrons

$$J_n\left(x\right) = q\mu En\left(x\right) + qD_n\frac{dn\left(x\right)}{dx} \tag{2.13}$$

Similarly, the current equation for holes is given by

$$J_p\left(x\right) = q\mu Ep\left(x\right) - qD_p\frac{dp\left(x\right)}{dx} \tag{2.14}$$

Thus far we have been able to derive the current equations using the first moment of the BTE. Similarly, we can obtain the continuity equations from the BTE by using the zeroth moment. In this case we consider a time dependent BTE within the relaxation time approximation (Eq. 2.15) and then integrate it with respect to *dv* (Eq. 2.16).

$$\frac{df}{dt}+\frac{qE}{m^*}\frac{df}{dv}+v\frac{df}{dx}=\frac{f_0-f\left(v,x\right)}{\tau} \tag{2.15}$$

$$\int\frac{df}{dt}dv+\frac{qE}{m^*}\int\frac{df}{dv}dv+\int v\frac{df}{dx}dv=\int\frac{f_0-f\left(v,x\right)}{\tau}dv \tag{2.16}$$

The first integral term on the left-hand side gives us the change of concentration *w.r.t* time.

$$\int\frac{df}{dt}dv=\frac{d}{dt}\int f dv=\frac{dn}{dt} \tag{2.17}$$

The second integral goes to zero as the distribution function is zero for *v* integrated between plus or minus infinity. The third integral gives the time dependent continuity equation for electrons and holes to be of the form

$$\begin{aligned}\frac{dn}{dt}&=\frac{1}{q}\nabla\bullet J_n+G-R\\ \frac{dp}{dt}&=-\frac{1}{q}\nabla\bullet J_p+G-R\end{aligned} \tag{2.18}$$

where, G - R are the generation recombination mechanisms such as Shockley-Read-Hall (SRH), Auger, radiative etc. The continuity equations and current density equations combined with Poisson's equation form the backbone of the drift-diffusion model.

2.1 Poisson's Equation

Poisson's equation describes the relation between the electrostatic potential and the charge density in the device for quasi-static conditions. In general, for spatially varying permittivity, it equals to

$$\nabla\bullet\left(\varepsilon\nabla\phi\right)=-\rho \tag{2.19}$$

where, ε is the permittivity of the material and ρ is the charge density. For homogeneous systems, Eq. 2.20 can be written as

$$\nabla^2\varphi = -\frac{\rho}{\varepsilon} \tag{2.20}$$

The term ρ represents all sources of charge in the system. In most devices, the charge is significantly affected by the presence defects. Thus, a more complete version of the Poisson's equation in 1D is of the form

$$\begin{aligned} &\frac{\delta}{dx}\varepsilon(x)\left(\frac{\delta}{\delta x}\varphi(x)\right) = -q\left(p(x) - n(x) + N_D(x) - N_A(x)\right) + \sum \rho(x), \\ &\sum \rho = \sum \rho_{DB} + \sum \rho_{Donor} + \sum \rho_{Acceptor} \end{aligned} \tag{2.21}$$

where ρ represents the charge contribution due to acceptors, donors and dangling bonds. The expression for dangling the bond (mid gap) defects is given by Eq. 2.22 and the donor/acceptor type defects are given by Eq. 2.23

$$\rho_{DB}(x) = q\int\left[f^{DB}_{+,trap}(E,x) - f^{DB}_{-,trap}(E,x)\right]N_{DB}(E,x)\,dE \tag{2.22}$$

$$\begin{aligned} \rho_{Donor}(x) &= q\int f_{Donor}(E,x)N_{trap}(E,x)\,dE \\ \rho_{Acceptor}(x) &= -q\int f_{Acceptor}(E,x)N_{trap}(E,x)\,dE \end{aligned} \tag{2.23}$$

where $N(E,x)$ is the density of states of the defects, $f_{+/-}(E,x)$ is the probability of occupation for positively/negatively charged amphoteric dangling bond (DB) states, and $f(E,x)$ is the probability of occupation. In the context of SHJ solar cells which uses a-Si:H, the trap density function is used to describe the band-tail states (Eq. 2.24) which exist below the band edge, and the mid gap states (Eq. 2.27) [23]

$$N(E) = N_{VBT}\exp\left(\frac{-(E - E_V)}{E_0}\right) \tag{2.24}$$

where N_{VBT} is the density of states of the localized defects, E_V is band edge and E_0 is the characteristic decay/Urbach energy. The probability of occupation for the localized states in equilibrium can be calculated by using the Fermi-Dirac distribution function

$$f_1(E) = \frac{1}{1 + e^{\frac{E - E_F}{kT}}} \tag{2.25}$$

Thus, the probability of a defect being unoccupied (f_0) can be given by the relation

$$f_1(E) + f_0(E) = 1 \tag{2.26}$$

The midgap states, which are caused due the dangling bonds, are defined by a Gaussian distribution

$$N_{Midgap}(E) = \frac{N_{DB}}{\sigma_{DB}\sqrt{2\pi}} e^{-\frac{(E - E_{DB})^2}{2\sigma_{DB}^2}} \tag{2.27}$$

The midgap states are amphoteric in nature and their occupational probability is given by

$$\begin{aligned} f_+(E) &= \frac{1}{1 + 2e^{\frac{E_F - E}{kT}} + e^{\frac{2E_F - 2E - U}{kT}}} \\ f_0(E) &= \frac{2e^{\frac{E_F - E}{kT}}}{1 + 2e^{\frac{E_F - E}{kT}} + e^{\frac{2E_F - 2E - U}{kT}}} \\ f_-(E) &= \frac{e^{\frac{2E_F - 2E - U}{kT}}}{1 + 2e^{\frac{E_F - E}{kT}} + e^{\frac{2E_F - 2E - U}{kT}}} \end{aligned} \tag{2.28}$$

where E_F is the Fermi energy and U is the correlation energy. The nature of the defect states, their distribution, and their effect are discussed in greater detail in 0.

To accurately calculate carrier densities for general degenerate semiconductors, we use

$$n = N_C f_{\frac{1}{2}}\left[\frac{E_F - E_C}{kT}\right]$$
$$p = N_V f_{\frac{1}{2}}\left[\frac{E_V - E_F}{kT}\right] \tag{2.29}$$

where $N_{C,V}$ is the effective conduction/valence band density of states, $E_{C,V}$ is the conduction/valence band edge and E_F is the Fermi level. The $f_{1/2}$ function is the Fermi integral of order ½ that can easily be calculated using analytical approximations.

2.2 Band Offsets

To compute the electrostatic potential in homojunctions, one can use the simplified version of the Poisson's equation (Eq. 2.20) which assumes constant spatial permittivity and electron affinity levels. However, for the case of heterojunctions, these assumptions are no longer valid. Due to the spatial variation of various parameters, the energy band diagram (shown in Fig. 2.1) of heterostructure devices will exhibit discontinuities.

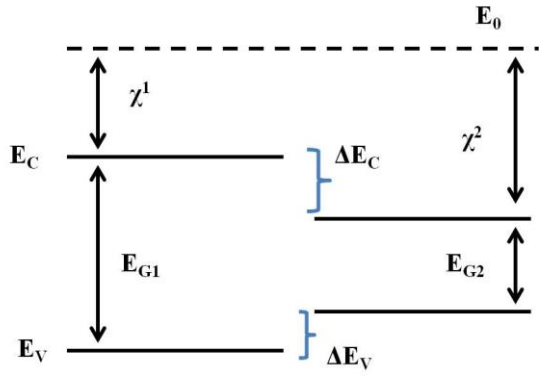

Figure 2.1. Schematic diagram of a heterostructure.

The origin and exact determination of the band offset is still a matter of debate; however most simulation methods follow Anderson's model [24]

$$\begin{aligned} \Delta E_C &= \chi_2 - \chi_1 \\ \Delta E_V &= E_{g1} - E_{g2} - \Delta E_C \end{aligned} \tag{2.30}$$

In order to include the effect of the spatial variation of parameters while calculating the potential, a 'band parameter' approach [16,17] was adopted, which takes into consideration the discontinuity in the intrinsic Fermi level of the device

$$\theta = \frac{\chi_2 - \chi_1}{q} + 0.5\frac{E_{g2} - E_{g1}}{q} \tag{2.31}$$

where χ is the electron affinity and E_g is the band gap of the material. The subscript '1' denotes the reference material.

2.3 Normalization and Scaling

The variables in the drift diffusion model are usually implemented in a normalized form. Normalized variables make the algorithm more efficient and prevents issues like numerical overflow. The length is scaled by the Debye length (l_{Debye}), the carrier density by the intrinsic carrier concentration (n_i), and potential by the thermal voltage (V_t)

$$dx = \frac{dx}{l_{Debye}}; \mathrm{n,p} = \frac{n, p}{n_i}; \varphi = \frac{\varphi}{V_t} \tag{2.32}$$

2.4 Finite Difference Approach

The drift-diffusion model is a decoupled solution to a set of differential equations. These equations are solved over a spatial domain as boundary value problems. In this thesis, the finite difference method was used to approximate and solve the partial difference

equations. Poisson's equation, which is a 2nd order partial differential equation can be approximated using the central difference scheme, which in 1D can be given by

$$
\begin{aligned}
&a_i\varphi_{i+1}^{n+1} + b_i\varphi_i^{n+1} + c_i\varphi_{i-1}^{n+1} = -(p_i - n_i + C_i) - (p_i + n_i)\varphi_i^n \\
&a_{i+1} = \left(\frac{\varepsilon_{i-1} - \varepsilon_{i+1}}{dx_i + dx_{i-1}} - \frac{2\varepsilon_i}{dx_{i-1}} \right) / \left(dx_i + dx_{i-1} \right) \\
&b_i = -\left(p_i + n_i - \frac{2\varepsilon_i}{dx_{i-1}dx_{i-1}} \right) \\
&c_i = \left(\frac{\varepsilon_{i+1} - \varepsilon_{i-1}}{dx_i + dx_{i-1}} - \frac{2\varepsilon_i}{dx_i} \right) / \left(dx_i + dx_{i-1} \right)
\end{aligned}
\tag{2.33}
$$

where *dx* is the spacing between node points, and '*i*' is the node point index.

2.5 Continuity Equation

Earlier in this chapter, a time dependent continuity equation (Eq. 2.18) was briefly derived from the BTE. Equation 2.18 can also be utilized to derive a steady state continuity equation, which is given by

$$
\begin{aligned}
&\frac{1}{q}\nabla \bullet J_n = -(G - R) \\
&\frac{1}{q}\nabla \bullet J_p = G - R
\end{aligned}
\tag{2.34}
$$

These steady-state continuity equations can discretized using finite differences. Equations 2.35 and 2.36 show the discretized forms of the electron and hole continuity equations

$$
\begin{aligned}
&\frac{D_{i+1/2}^n}{\Delta^2} n_{i+1} B\left(\frac{\varphi_{i+1} - \varphi}{V_T} \right) - \left[\frac{D_{i-1/2}^n}{\Delta^2} B\left(\frac{\varphi_{i+1} - \varphi_i}{V_T} \right) + \frac{D_{i+1/2}^n}{\Delta^2} B\left(\frac{\varphi_i - \varphi_{i-1}}{V_T} \right) \right] n_i \\
&+ \frac{D_{i-1/2}^n}{\Delta^2} B\left(\frac{\varphi_{i-1} - \varphi_i}{V_T} \right) n_{i-1} = G_i
\end{aligned}
\tag{2.35}
$$

$$\frac{D_{i-1/2}^{n}}{\Delta^2} p_{i-1} B\left(\frac{\varphi_i - \varphi_{i-1}}{V_T}\right) - \left[\frac{D_{i-1/2}^{n}}{\Delta^2} B\left(\frac{\varphi_{i-1} - \varphi_i}{V_T}\right) + \frac{D_{i+1/2}^{n}}{\Delta^2} B\left(\frac{\varphi_{i+1} - \varphi_i}{V_T}\right)\right] p_i + \frac{D_{i+1/2}^{n}}{\Delta^2} B\left(\frac{\varphi_i - \varphi_{i+1}}{V_T}\right) p_{i+1} = G_i \tag{2.36}$$

where B is the Bernoulli function that arises due to the Scharfetter-Gummel discretization scheme, Δ is the distance between nodepoints, and 'i' is the nodepoint index. To include the effect of varying parameters across different materials, a band-parameter approach is used where θ_n and θ_p are band parameters for electron and holes respectively

$$\theta_n = \left(\chi(x) - \chi_r\right) + \frac{kT}{q} \ln\left(\frac{N_c(x)}{N_{cr}}\right) \tag{2.37}$$

$$\theta_n = \left(\chi(x) - \chi_r\right) + \frac{kT}{q} \ln\left(\frac{N_c(x)}{N_{cr}}\right) \tag{2.38}$$

where $\chi(x)$ is the spatially varying electron affinity, $N_{c,v}$ is the effective conduction/valence band density of states, and the subscript '*r*' denotes the reference material. The band-parameters are included as in the continuity equation solution to account for varying material parameters. For electrons, $\varphi=\varphi+\theta_n$, and for holes, $\varphi=\varphi-\theta_p$

2.6 Generation and Recombination Mechanisms

The term on the right-hand side of Eq.'s 2.35 and 2.36 represents all the generation and recombination in the system. These mechanisms play a pivotal role in determining how the charge density varies within a device. For a solar cell, these mechanisms have great significance, as the recombination mechanism affects the dark current. The generation term determines the charge generated due to illumination which has a direct impact on the short circuit current calculations. The generation rate in 1D can be calculated by

$$G(x) = \frac{\alpha(\lambda)(1-R)P_{OPT}}{Ah\nu} \exp\left[-\alpha(\lambda)x\right] \tag{2.39}$$

where α is the wavelength dependent absorption, R is the reflectivity, P is power density of incident light, A is the cross-sectional area of the device, and hυ is the energy of the incident light.

The main recombination methods that are considered are Shockley-Read-Hall (SRH) recombination, radiative recombination and auger recombination

$$R_{SRH} = \frac{pn - n_i^2}{\tau_p(n + n_i) + \tau_n(p + n_i)} \tag{2.40}$$

where p and n are carrier densities, n_i is the intrinsic carrier density, and τ is the lifetime

$$R_{Radiative} = B\left(pn - n_i^2\right) \tag{2.41}$$

where B is the radiative coefficient

$$R_{Auger} = C_n n\left(np - n_i^2\right) - C_p p\left(np - n_i^2\right) \tag{2.42}$$

where $C_{n,p}$ are the Auger coefficients.

2.7 Gummel Iteration Scheme

Gummel's method solves the electron and continuity equations along with Poisson's equation in a decoupled manner (shown in Fig. 2.2). At first, the nonlinear Poisson equation is solved to provide an initial guess (potential, carrier densities) for the continuity equations. The solution of the continuity equations provides values of the carrier densities which are used by the linear Poisson equation to calculate new potentials. The new

potentials are then fed back into the continuity equations. This process is repeated until the solution for the potential using the linear Poisson equation converges.

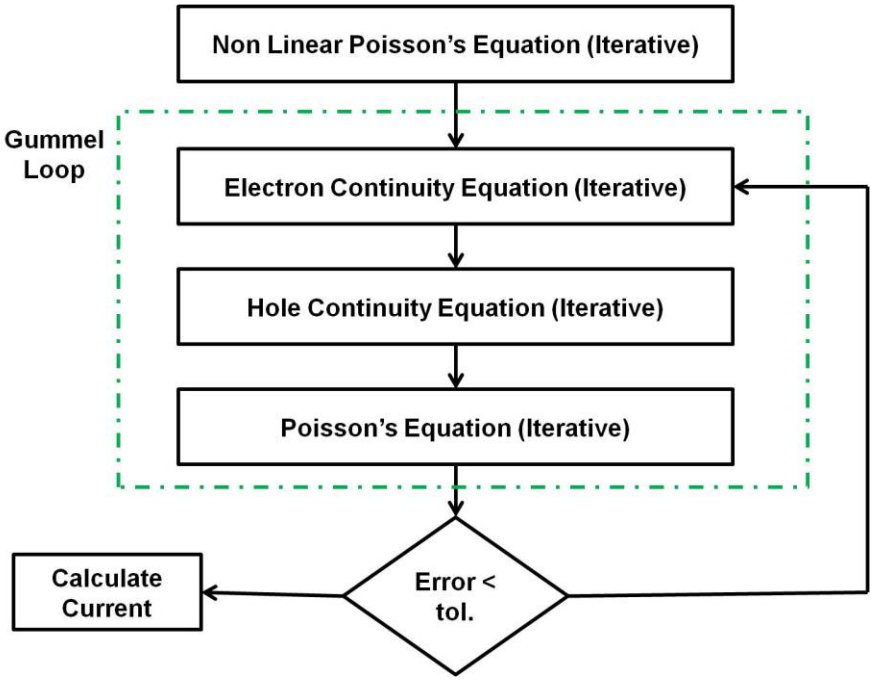

Figure 2.2. Gummel loop flowchart for the drift diffusion model.

The partial differential equations used to form the drift diffusion model represent an $Ax=b$ problem. The successive over relaxation (SOR) method has been used to solve this matrix problem. Each set of equations in the drift diffusion model must be solved iteratively until convergence to obtain stable charge densities and current density profiles.

2.8 Technology Computer Aided Design (TCAD) tools

Some of the work presented in this dissertation (most notably in Chapter 3) uses the Atlas device simulator of the commercially available TCAD tool Silvaco. The drift-diffusion model in Atlas solves Poisson's equation along with the continuity equations to determine device level properties. Atlas uses the finite-element method (FEM) to solve the

partial differential equations (PDE's) as opposed to the finite-difference method that was implemented to solve the PDE's for the in-house drift-diffusion solver described earlier in this chapter.

The recombination mechanisms taken into account by using Atlas are the same as described in Section 2.6. Due to the nature of the heterointerfaces in the SHJ solar cell, thermionic emission and band to band tunneling (local and non-local) models were used to describe transport. The in-house drift-diffusion solver was calibrated with Atlas to ensure consistency of results.

2.9 Conclusion

The drift-diffusion model is an ideal method to study low-field, semi-classical transport. However, many modern devices have novel structures and materials due to which the physics of transport cannot be captured completely with low-field semi-classical transport theory. The drift-diffusion model has many underlying assumptions. In general, the model does not take into consideration the non-idealities and non-local behavior that arises due to high fields. It assumes that the charge carriers are always in thermal equilibrium. Extensions to the model have been made for high-field behavior by the ad-hoc introduction of a field-dependent mobility and diffusion coefficient. In SHJ solar cells, relatively high electric fields exist at the a-Si:H(i)/c-Si heterointerface. To understand the behavior of photogenerated carriers at the heterointerface, a theoretical formulation is required that can treat the non-local behavior of the energy distribution function that arises due to high fields. The ensemble Monte Carlo method is an ideal tool to study such behavior, as discussed in Chapter 4.

CHAPTER 3

CONTACT RESISTIVITY MODELING

Silicon heterojunction (SHJ) solar cell architectures consisting of hydrogenated amorphous silicon [a-Si:H] and crystalline silicon [c-Si] have emerged as commercially viable solar cell technologies due to their high cell efficiencies [19]. In part, high efficiencies are achieved by using device structures that use carrier selective and passivating contacts in order to efficiently collect photogenerated carriers, which in the case of SHJ solar cells are heterojunction stacks placed on the c-Si absorber (see Fig. 3.1). Simply put, carrier selective contacts are designed to collect majority carriers while blocking minority carriers. The principle of creating selective transport in contacts has previously been described by Würfel *et al.* and Cuevas *et al.* [19,20]. Selectivity is established by creating a large asymmetry in the conductivities of majority vs. minority carriers, i.e. high conductivity of holes and low conductivity of electrons for a hole contact and vice versa for an electron contact. In addition, a reduction in the surface recombination velocity of minority carriers also contributes to the increase in selectivity of a contact, as it reduces minority carrier recombination current. It would be ideal if a single material could offer multiple levels of selectivity; however, in reality this is difficult to achieve with just a single material on top of an absorber layer. In the SHJ solar cell structure investigated in this thesis, selectivity is achieved by depositing a combination of doped (n or p type) hydrogenated amorphous silicon [a-Si:H(n/p)] and intrinsic hydrogenated amorphous silicon [a-Si:H(i)] on an n-type c-Si absorber layer (see Fig. 3.1). In this structure, the doped a-Si:H creates the large asymmetry in the carrier conductivity between electrons and holes,

whereas the a-Si:H(i) provides crucial passivation at the a-Si:H(i)/c-Si heterointerface. It is also important to note that the contact structure includes an n-type indium tin oxide [ITO(n^+)] layer that is placed over the doped a-Si:H. Even though this layer does not affect the selectivity of the contact, it does add another layer of complexity to the transport of photogenerated carriers through the contact structure.

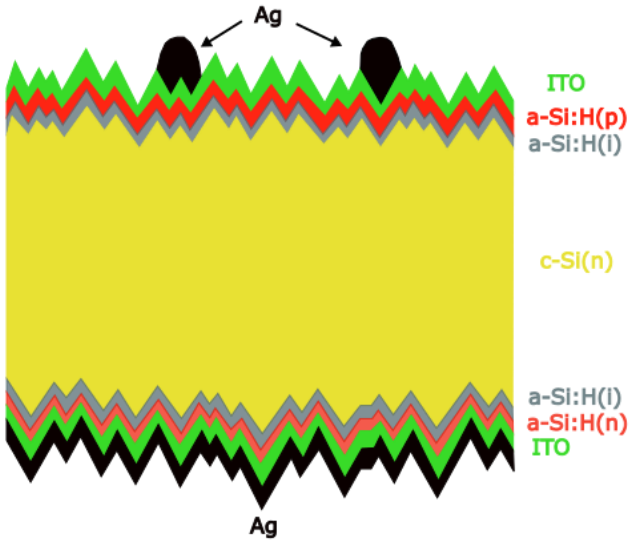

Figure 3.1. Schematic diagram of a SHJ solar cell.

Previously, Brendel and Peibst described a parameter S (selectivity) (Eqn. 3.1) as a quantitative metric to evaluate the effectiveness of a contact [28]

$$S = \log\left(\frac{V_{th}}{J_c \rho_c}\right) \tag{3.1}$$

where, V_{th} is the thermal voltage, J_c is the recombination current due to minority carriers, and ρ_c is the contact resistivity. The transfer length method (TLM) can be used to measure the contact resistivity and other resistive loss parameters in contact structures for solar cells [29]. In this chapter we consider a hole contact for a SHJ solar cell which consists of an a-

Si:H(i)/a-Si:H(p)/ITO(n^+)/Ag stack on a c-Si absorber. This method allows the analysis of a simpler device structure while capturing all the representative physics of the contact stack. Previously, several authors have attempted to characterize the behavior of hole contacts for SHJ solar cells. Lachenal *et al.* reported a contact resistivity as low as 0.24 Ω-cm^2 for an a-Si:H(i)/a-Si:H(p)/ITO(n^+) stack for a SHJ cell with an efficiency of 22.4% [30]. Lee *et al.* obtained a contact resistivity as low as 0.38 Ω-cm^2 for c-Si(p)/a-Si:H(i)/a-Si:H(p)/ITO/Ag contact stack for a SHJ cell with an efficiency of 20.5% [31]. While these studies quantify resistive losses in various layers of the hole contact stack, they do not provide an insight on the transport mechanisms that contribute to these resistive losses.

The hole contact structure being investigated in this chapter consists of two hetero-interfaces, namely ITO(n^+)/a-Si:H(p) and a-Si:H(i)/c-Si, that act as barriers and impede carrier transport, thus contributing to the overall increase in resistance of the contact stack. These resistive losses are detrimental to the overall fill factor (FF) and performance of the solar cell [32]. Several studies have been previously conducted to understand carrier transport at the a-Si:H(i)/c-Si heterointerface. Crandall *et al.* characterized hole collection through the a-Si:H(i) layer by transient capacitive experiments [33]. These studies concluded that photogenerated holes are collected via a 'hopping' mechanism rather than direct tunneling. Muralidharan *et al.* also concluded that holes are collected via 'hopping' by conducting simulations using the kinetic Monte Carlo method [34]. Taguchi *et al*. conducted temperature dependent dark J-V experiments on HIT cells and concluded that multi-step tunneling is the dominant mechanism for transport across the a-Si:H(i) at low voltages [35]. Even though there are several studies that focus on the transport across the

a-Si:H(i)/c-Si interface, the ITO(n^+)/a-Si:H(p) hetero-interface has not been explored in any great detail. Simulations conducted by Kanevce *et al.* concluded that tunneling through the ITO(n^+)/a-Si:H(p) junction has a significant effect on the *J-V* curves of a SHJ solar cell [36]. However, most simulation studies have thus far treated the ITO as a Schottky contact whilst studying cell level properties [37]–[39].

The simulations presented in this chapter complement experiments that were previously conducted by Leilaeiloun *et al.* who used the TLM technique to measure the contact resistivity of an a-Si:H(i)/a-Si:H(p)/ITO(n^+) stack on a p-type c-Si wafer, and measured a contact resistivity as low as 0.1 Ω-cm^2. Corresponding simulations calculated the contact resistivity (while treating the ITO as a semiconductor) by varying the a-Si:H(i) layer thickness and obtained agreement with experimental values [40]. This chapter describes a thorough analysis of transport through a hole contact stack [a-Si:H(i)/a-Si:H(p)/ITO(n^+)] on p-type c-Si. This is done by varying parameters such as the a-Si:H(i) layer thickness, a-Si:H(p) layer doping, ITO(n^+) layer doping, temperature and defect densities at the a-Si:H(i)/c-Si interface. By considering a hole contact placed on a p-type c-Si wafer, the resistance of the contact structure can be accurately measured without having any losses due to minority carrier (electron) recombination.

3.1 Theoretical Model

A TLM structure (shown in Fig. 3.2) of the SHJ hole contact on p-type c-Si was recreated using the Silvaco (Atlas). The simulations are based on the drift-diffusion model shown in Chapter 2. However, instead of simulating the entire structure with all the contact pads, the simulation domain only consists of the pair of contacts that need to be probed to

determine resistance. This is done in order to reduce the size of the simulation domain and reduce simulation time. This reduction is a valid assumption as long as the effective transfer length (L_T) is much lesser than the length of the contact pad. The simulations swept the *I-V* for a pair of contacts while increasing the pad spacing to create the total resistance (R_T) vs. contact pad spacing (L) plot (see Fig. 3.5). The contact resistivity can be obtained from this plot using Eq.'s 3.5, 3.6 and 3.7. The simulations assume the length of the contact pads to be 2 mm, and the contact pad spacing is varied from 250 to 2000 μm. All simulations and experiments were conducted in the dark, and the simulations assume the ITO/Ag interface to be perfectly ohmic. Experiments have shown that the resistive loss form the ITO/Ag interface is negligible.

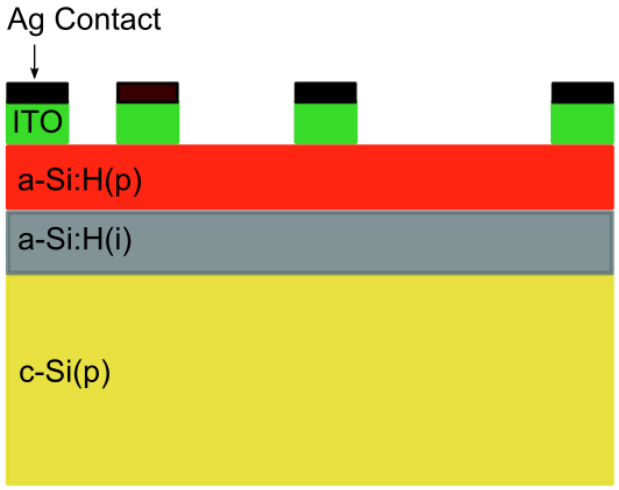

Figure 3.2. Schematic diagram of a TLM pattern for a SHJ solar cell.

3.1.1 Interface Physics

The heterojunction contact stack we are analyzing consists of an a-Si:H(i)/a-Si:H(p)/ITO(n^+) stack on a p-type c-Si wafer. In this structure, carriers encounter potential barriers at the a-Si:H(i)/c-Si(p) heterointerface and the ITO(n^+)/a-Si:H(p) heterointerface. The simulated equilibrium band diagram in Fig. 3.3 shows the potential barrier that impedes carrier transport at the a-Si:H(i)/c-Si(p) heterointerface. We include direct tunneling to model transport through the barrier and, thermionic emission to model transport over the barrier. The aforementioned models are built in the Silvaco software.

The ITO(n^+)/a-Si:H(p) junction (shown in Fig. 3.4) requires careful consideration as it forms the final barrier between the photogenerated carriers and the metal contact. In most simulation studies, the ITO has been considered to be a metallic contact with a workfunction, ϕ^{ITO}. Kanevce *et al.* have previously shown that tunneling through the ITO(n^+)/a-Si:(p) junction has a significant effect on the *J-V* characteristics of solar cells [18], and that the consideration of the ITO layer as a n-type semiconductor places stringent restrictions on parameters that can be used to conduct simulations to replicate realistic scenarios. It has already been established that the ITO is a semiconductor with a well-defined optical bandgap [41]. For the purposes of a SHJ solar cell, the ITO is heavily n doped. The inclusion of the ITO as an n-type semiconductor forms a *pn* junction with the a-Si:H(p) emitter. Therefore, when positive bias is applied on the SHJ cell, the ITO(n^+)/a-Si:H(p) junction is reverse biased. The consequences of including the ITO as a semiconductor is discussed in greater detail in the results and discussion section.

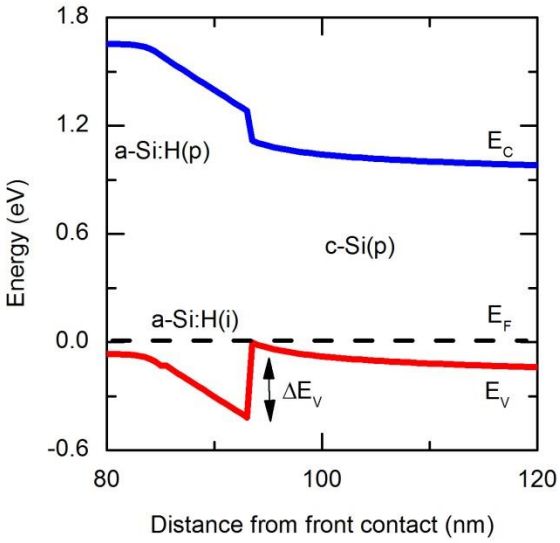

Figure 3.3. Simulated equilibrium band diagram of the a-Si:H(i)/c-Si interface.

The defect states in the a-Si:H are considered by including exponentially decaying states below the band edges [5] and mid gap states which are included by using the defect pool model [42]. The effect of chemical passivation is also considered by including defects at the a-Si:H(i)/c-Si heterointerface. This is done by adding a defect density at a single energy (midgap) at the heterointerface. All simulations consider an interface defect density ~ 10^{10} cm^{-2} unless mentioned otherwise. A complete list of the base parameter set used for the simulations can be found in Table I.

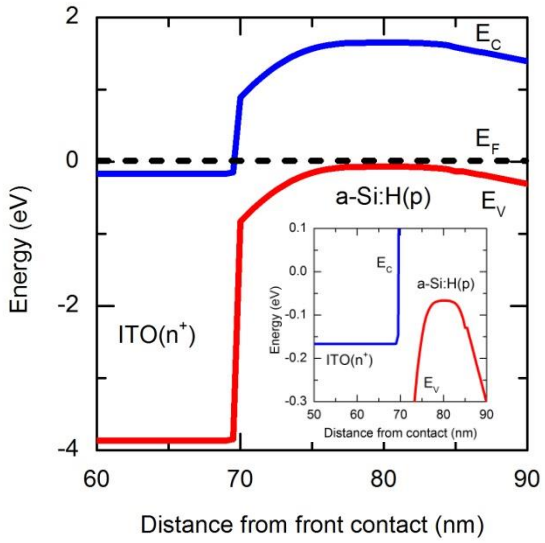

Figure 3.4 Simulated equilibrium band diagram of the ITO(n+)/a-Si:H(p) heterointerface. (Inset) A zoomed in look at the hetero-interface where band to band tunneling occurs.

3.1.2 TLM Theory

The current transport in the TLM structure (shown in Fig. 3.2) is two dimensional. The current travels vertically across the ITO(n^+)/a-Si:H(p) and a-Si:H(i)/c-Si(p) heterointerfaces, and laterally through the accumulation layer that is formed at the a-Si:H(i)/c-Si(p) interface. Since, the hole contact is placed on p-type c-Si, the current path approximates a resistor which is modulated by the ITO(n^+)/a-Si:H(p) and a-Si:H(i)/c-Si(p) heterointerfaces. The *I-V* characteristics for different contact pad spacings are calculated by conducting a voltage sweep. Total resistance (R_T) for various contact pad spacings is obtained from Fig. 3.5a by calculating the slope from the *I-V* curve at 0 V. Several useful parameters can be extracted from Fig. 3.5b. The sheet resistance (R_s) can be extracted by calculating the slope and multiplying it with the contact width (W) (see Eq. 3.5). The y-

intercept in Eq. 5 is used to calculate the contact resistance (R_C). The x-intercept is used to calculate the effective transfer length, as shown in Eq. 3.6. The contact resistivity (ρ_c) can then be calculated by using R_C, L_T and W (see Eq.'s 3.5, 3.6 and 3.7). By following this procedure, the simulations closely mimic the experimental extraction of parameters as done by the TLM method

$$R_T = \frac{R_S}{W} L + 2R_C \tag{3.2}$$

$$L_T = \frac{R_C}{2 \times \text{Slope}} \tag{3.3}$$

$$\rho_C = R_C \times L_T \times W \tag{3.4}$$

3.1.3 Recombination

The defect recombination in the bulk is modeled using traditional forms of the Shockley-Read-Hall (SRH), the radiative, and the Auger mechanisms (see Chapter 2). However, since the a-Si:H and c-Si layers are both p-type doped, bulk recombination plays a minimal role in affecting transport in the unipolar TLM structure.

3.1.4 Temperature

Contact resistivity variation was analyzed w.r.t to temperature in order to understand the limiting behavior of various transport mechanisms. For this purpose, a thermionic emission model [43] is included to describe the transport of carriers over the energy barriers. The effect of temperature on contact resistivity is further discussed in Section 3.2.

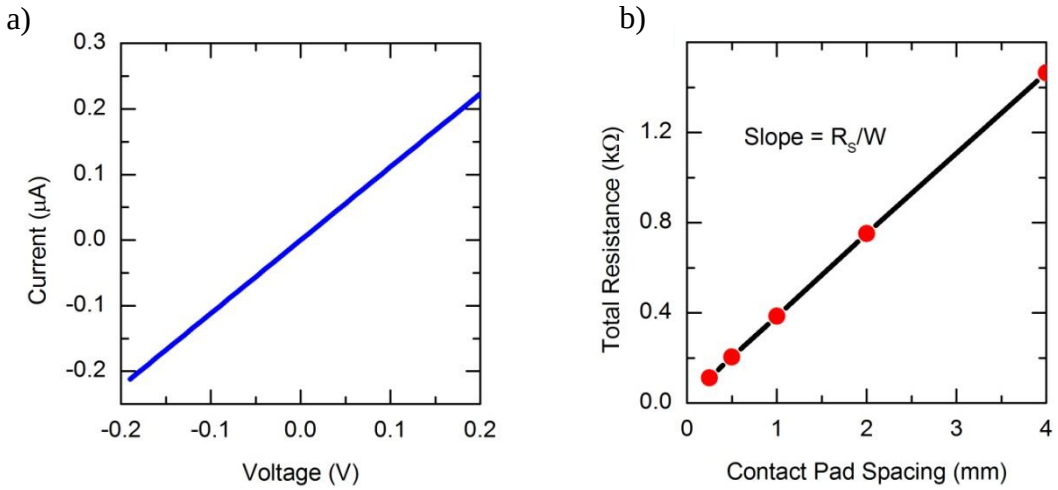

Figure 3.5. a) Simulated *I-V* curve obtained by conducting a voltage sweep for a pair of contacts. b) Simulated total resistance (slope of *I-V* curve in Fig. 4a) vs. contact pad spacing.

3.2 Results and Discussion

3.2.1 Variation of a-Si:H(i) Layer Thickness

Figure 3.6a shows the simulated contact resistivity vs. the a-Si:H(i) layer thickness, where the green lines treat the ITO as a metallic contact with a workfunction. To treat the metallic contact, a Schottky barrier tunneling model [26,27] is included to describe transport through the barrier at the ITO/a-Si:H(p) interface. As can be seen in Fig. 3.6a, when $\phi^{ITO} > 5.0$ eV, contact resistivities as low 10^{-2} Ω-cm^2 (for a 4 nm thick a-Si:H(i) layer) are obtained. However, when ϕ^{ITO} is reduced to 4.8 eV, the contact resistivity increases by almost an order of magnitude. This increase in contact resistivity can be attributed to the increase in the barrier offset at the ITO/a-Si:H(p) interface. Simulations indicate that when $\phi^{ITO} < 4.8$ eV, a large barrier is created at the ITO/a-Si:H(p) interface which completely suppresses the current unless we resort to unrealistic doping levels (>10^{21} cm^{-3}) in the a-

Si:H(p) layer. Experimental measurements have shown ϕ^{ITO} to be ~ 4.7 eV [Refs. 28,22,23]. In the case of the a-Si:H(p) layer, Bivour *et al.* [49] and Psych *et al.* [50] demonstrated through experiment and simulation that a diborane (B_2H_6) gas phase doping ~ 2100 ppm (~10^{19} cm^{-3}) was required to achieve high fill factors. Thus, a low workfunction ITO on top of a high workfunction a-Si:H(p) layer will lead to a barrier offset resulting in photocurrent suppression at the ITO/a-Si:H(p) heterointerface.

In Fig. 3.6a, the blue line represents the ITO being treated as an n-type semiconductor. The heavily doped ITO(n^+) layer forms a *np* junction with the a-Si:H(p) layer. The electron affinity (χ^{ITO}) for the ITO(n^+) is equal to 4.5 eV, and as the ITO(n^+) is doped ≈ 10^{20} cm^{-3}, the Fermi-level lies ~ 0.12 eV above the conduction band which results in $\phi^{ITO} < 4.5$ eV. As discussed before, a low workfunction ITO is detrimental for carrier transport across the ITO(n^+)/a-Si:H(p) heterointerface. However, high doping in the ITO(n^+) layer is crucial as it causes steep band bending at the ITO(n^+)/a-Si:H(p) interface, which facilitates band to band tunneling (see Fig. 3.4). This approach gives a better match with experiments while using realistic parameters. Table I shows the base parameters that were used in the simulation.

Figure 3.6b shows the simulated (blues lines) and experimental (red) contact resistivity vs. a-Si:H(i) layer thickness for various a-Si:H(p) layer dopings. In Fig. 3.6b, the simulations (blue lines) treat the ITO as a semiconductor. As can be seen, the experimental results are best matched by a a-Si:H(p) doping = 1.8×10^{19} cm^{-3}. Figure 3.6b also shows that increasing the a-Si:H(p) layer doping leads to lower contact resistivities. This can be attributed to increased tunneling current due to steeper band bending at the ITO(n^+)/a-

Si:H(p) heterointerface caused by the increase in doping. The simulated ρ_c increases from 0.50 Ω-cm^2 → 2.1 Ω-cm^2 for an increasing a-Si:H(i) layer thickness from 4 nm → 16 nm. In comparison, the experimental ρ_c showed an increase from 0.48 Ω-cm^2 → 1.9 Ω-cm^2. The corresponding experimental series resistance increased from 1.2 Ω-cm^2 → 2.7 Ω-cm^2 as a result of increasing the a-Si:H(i) layer thickness [22]. The experiments also observed that the difference between the series resistance and ρ_c remained constant (within statistical error) with increasing a-Si:H(i) layer thickness. This indicates that all other contributions to series resistance remain the same as the a-Si:H(i) layer thickness increases, and the increase in series resistance is mainly due to the increase in ρ_c. Increasing a-Si:H(i) layer thickness increases contact resistivity for a combination of reasons. Firstly, the increase in the a-Si:H(i) layer thickness increases the transport distance for the carriers across the a-Si:H(i) layer. Secondly, the carrier density in the accumulation at the a-Si:H(i)/c-Si(p) heterointerface reduces by almost an order of magnitude as the a-Si:H(i) layer is increased from 4 nm to 16 nm. This causes the lateral transport through the accumulation layer to become more resistive.

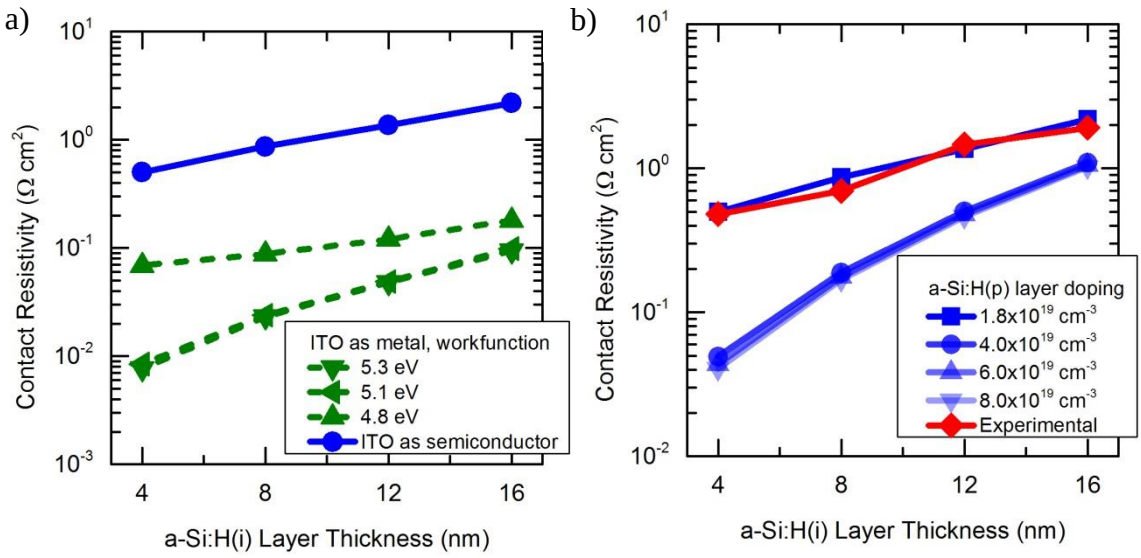

Figure 3.6. a) Simulated contact resistivity vs. a-Si:H(i) layer thickness where the ITO is treated as a Schottky contact (dashed green lines) and as a semiconductor (solid blue line) b) Simulated (blue) and experimental (red) contact resistivity vs. a-Si:H(i) thickness.

Figure 3.7 shows the same data plotted as a function of the a-Si:H(p) layer doping. It is observed that the contact resistivity decreases sharply as doping in the a-Si:H(p) layer increases. However, the decrease in contact resistivity is negligible at higher doping ($>10^{20}$ cm^{-3}). The decrease in contact resistivity can be attributed to increased tunneling current at the ITO(n^+)/a-Si:H(p) interface. However, after a certain point, an increase in doping does not effectively contribute to making the transport across the heterointerface less resistive.

To further understand the limiting transport mechanisms across the ITO(n^+)/a-Si:H(p) and the a-Si:H(i)/c-Si, we conducted TLM simulations w.r.t temperature. Figure 3.8a shows that contact resistivity increases with increasing a-Si:H(i) thickness (see section 3.2.1), however the contact resistivity appears to decrease with increasing temperature. This result can be explained by the results in Fig. 3.8b, which shows the simulated contact resistivity (blue) vs. temperature for an 8 nm thick a-Si:H(i) layer, where the a-Si:H(p)

doping is 1.8×10^{19} cm^{-3}. At a first order, the decrease in contact resistivity with increasing temperature can be attributed to an increase in the diode reverse saturation current (J_0). J_0 is directly proportion to the square of the intrinsic carrier concentration, which increases with temperature. Also, the diffusivity of carriers increases with temperature. It can also be observed in Fig. 3.8b that the simulated contact resistivity decreases by almost an order of magnitude when the thermionic emission model is added. Our simulations indicate that there is a significant contribution of thermionic emission at the a-Si:H(i)/c-Si(p) heterointerface, whereas there is no contribution of thermionic emission at the ITO(n^+)/a-Si:H(p) interface. The simulations also indicate that the sheet resistance increases with temperature while the transfer length decreases.

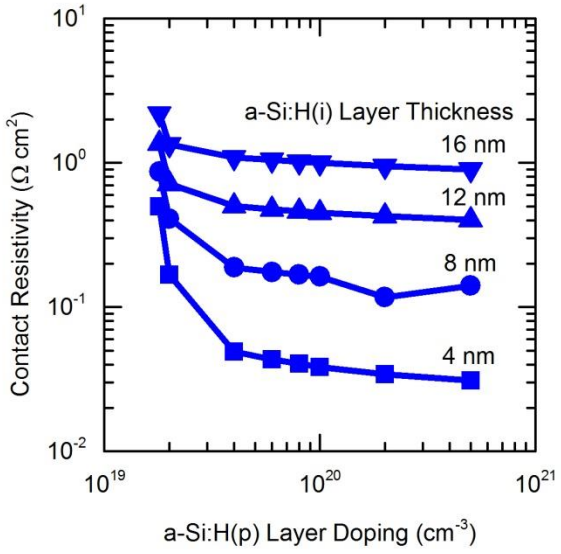

Figure 3.7. Simulated contact resistivity for different a-Si:H(i) layer thicknesses vs. a-Si:H(p) layer doping.

While there is some discrepancy at lower temperature, the simulations match the experimental (red) values almost exactly for high temperatures. The discrepancy in contact

resistivities at low temperatures can be due to the lack of a sophisticated mobility model in the simulation model at lower temperature. Also, our simulations did not consider changes in bandgap that can occur due to temperature variations.

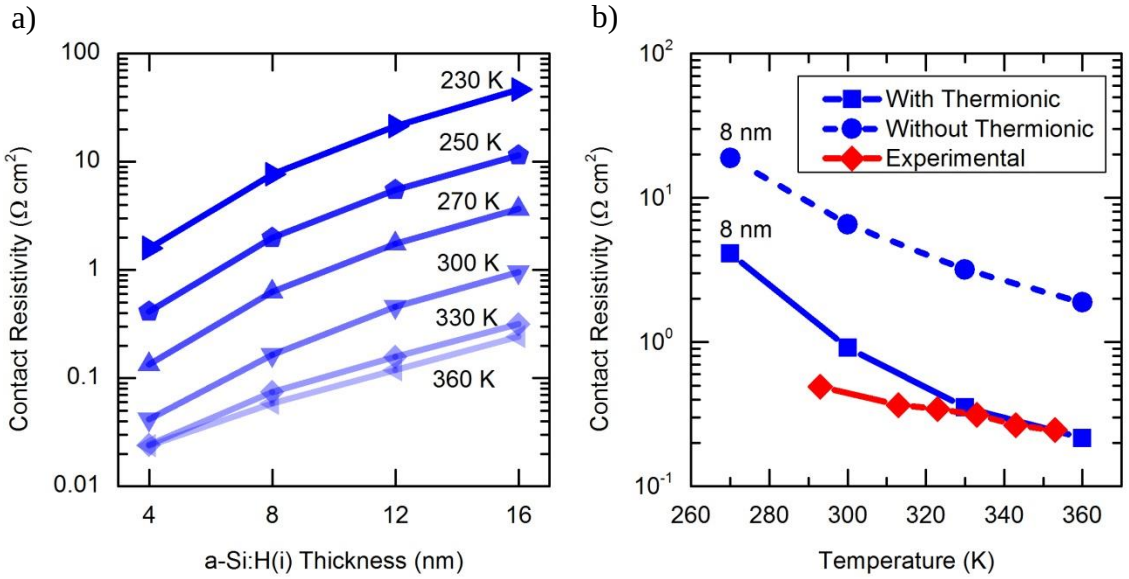

Figure 3.8. a) Simulated contact resistivity (red lines) vs. a-Si:H(i) layer thickness at different temperatures. b) Simulated contact resistivity (blue lines) and experimental contact resistivity (red line) vs. temperature for a a-Si:H(i) layer thickness = 8 nm. Simulated results treat the ITO as a semiconductor.

3.2.2 Variation of Interface State Defect Density at the a-Si:H(i)/c-Si(p) Interface

Figure 3.9 shows that the simulated contact resistivity (blue) vs. interface state defect densities at the a-Si:H(i)/c-Si(p) hetero-interface for a Si:H(i) layer thickness of 8 nm. An increase in the interface state defect density at the a-Si:H(i)/c-Si(p) heterointerface leads to a reduction in the accumulation layer density which makes lateral transport more resistive. It should be noted that even though there is a decrease in the carrier density at the a-Si:H(i)/c-Si(p) heterointerface with increasing interface state defect density, the heterointerface still remains accumulated, i.e. the surface density of holes at the a-Si:H(i)/c-

Si(p) >> acceptor density in the c-Si(p), even for interface state defect densities as high as 10^{13} cm^{-2}. The a-Si:H(i)/c-Si(p) heterointerface only starts to go out of accumulation when the interface state defect density becomes unphysical (~10^{14} cm^{-2}).

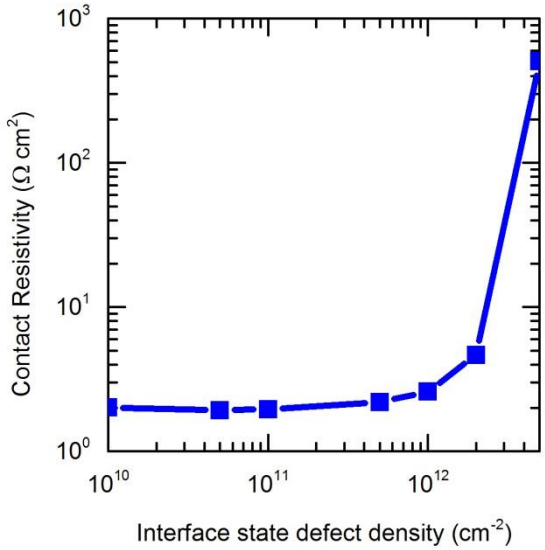

Figure 3.9. Simulated contact resistivities for different interface state defect densities at the a-Si:H(i)/c-Si(p) hetero-interface vs. a-Si:H(i) layer thickness.

3.2.3 Variation of ITO Doping

The decrease in contact resistivity shown in Figure 3.10 occurs due to the steeper band bending in the ITO(n^+)/a-Si:H(p) junction caused by increasing the doping in the ITO(n^+) layer; which in turn leads to increased tunneling current. It must also be noted that low ITO doping (< 10^{19} cm^{-3}) can result in non-linear I-V curves from the TLM structure; which complicates the extraction of the total resistance and makes the process unreliable. We use a slightly higher doping for the a-Si:H(p) (~ 5×10^{19} cm^{-3}) layer than presented in previous sections so that we could simulate a lower ITO doping. It is also important to note that a computational issue associated with using low doped layers in the ITO(n^+)/a-Si:H(p)

junction is that the non-local band to band tunneling model being used suffers from convergence issues when the layers are completely depleted.

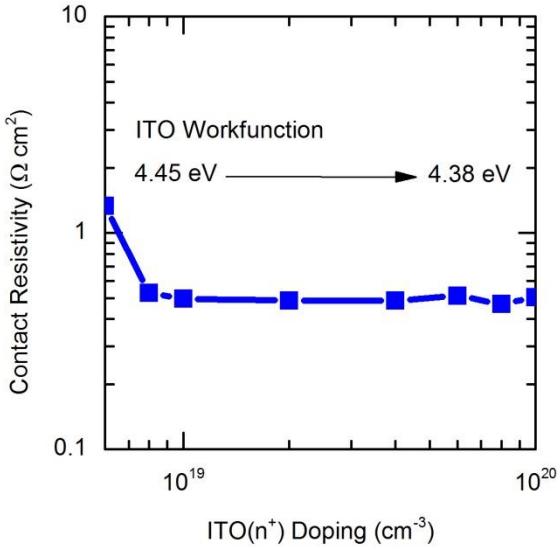

Figure 3.10. Simulated contact resistivity vs. ITO doping. The simulated results treat the ITO as a semiconductor.

Previous simulation studies conducted by Kanevce et al. [44,18] and Kirner *et al.* [52] showed the importance of the tunneling mechanism at the ITO(n^+)/a-Si:H(p) junction. Kanevce *et al.* argued that as a n-type SHJ is forward biased, the ITO(n^+)/a-Si:H(p) junction gets reverse biased resulting in the depletion of the a-Si:H(p) layer, thus, pushing photo-carriers away from the ITO(n^+)/a-Si:H(p) heterointerface. Their PSpice circuit model showed that the only way to reproduce experimental *J-V* curves was to have a tunneling mechanism that allows current transport across the ITO(n^+)/a-Si:H(p) junction.

Experiments conducted by Leilaeioun *et al.* [22] observed a drop in FF from 77.7% → 65% by increasing the oxygen partial pressure from 0.14 → 0.85 mTorr. Increasing the

oxygen partial pressure leads to reduced doping as the oxygen vacancies that act as n-type dopants are removed. This drop in FF can be correlated to an increased ρ_c, which as shown by the simulations, increases from 0.50 Ω-cm^2 → 1.33 Ω-cm^2 when the doping is reduced from 10^{20} cm^{-3} → 6×10^{18} cm^{-3}.

As mentioned previously, experiments indicated that an increase in oxygen partial pressure led to a reduction of FF. A first order analysis might indicate that the increase in ρ_c is due to a reduction in ϕ^{ITO}. However, if we assume that change in oxygen pressure does not affect the electron affinity, a decrease in doping would result in an increase of ϕ^{ITO} as the Fermi-level would move close to the conduction band (see Figs. 3.11a and 3.11b). It is worth noting that for semiconductors, the absolute value of the workfunction is the difference between the vacuum level and the Fermi level. Figure 3.10 shows that ρ_c decreases as ϕ^{ITO} decreases from 4.45 eV → 4.38 eV. In this case, a workfunction decrease is accompanied by a misalignment of the bands at the ITO(n$^+$)/a-Si:H(p) (shown in Fig. 3.11) which leads to reduced tunneling current, which in turn leads to an increase in ρ_c. Thus, we arrive at the conclusion that; 1) a high workfunction achieved by low doping in the ITO(n$^+$) layer will lead to reduced tunneling at the ITO(n$^+$)/a-Si:H(p) interface which will result in an increased ρ_c, and 2) a low workfunction achieved by high doping in the ITO(n$^+$) layer will lead to increased tunneling current and thus a lower ρ_c .

3.2.4 Fill Factor Variation with Contact Resistivity

In this section, the effect of contact resistivity on the FF of a SHJ solar cell is analyzed. These simulations were performed on an entire SHJ cell (see Fig. 3.1) where the a-Si:H(p) layer thickness = 7 nm, the a-Si:H(i) layer thickness is varied and the c-Si absorber is 180

μm. The doping in the a-Si:H(p) layer is = 1.8×10^{19} cm^{-3}. To consider the effect of ρ_c on device performance, we added ρ_c (calculated by the TLM simulations) as an external resistance on the contact.

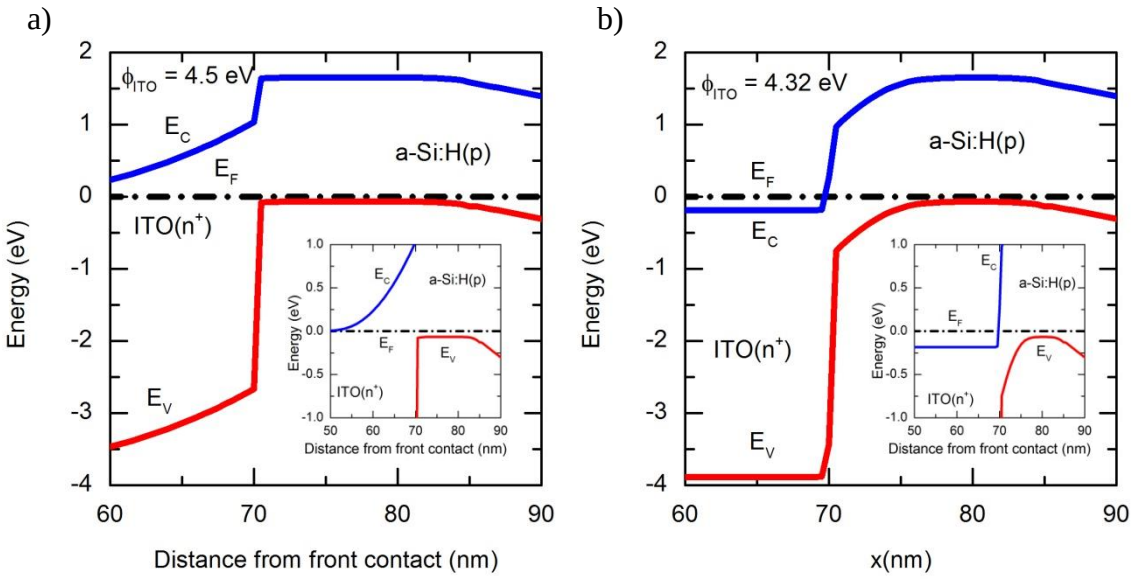

Figure 3.11. a) Equilibrium energy band diagram at the ITO(n^+)/a-Si:H(p) junction for an ITO(n^+) doping = 10^{18} cm^{-3}, ϕ_{ITO} = 4.5 eV. b) Equilibrium energy band diagram at the ITO(n^+)/a-Si:H(p) junction for a ITO(n^+) doping = 10^{21} cm^{-3}, ϕ_{ITO} = 4.32 eV. (Inset) A close up of the ITO(n^+)/a-Si:H(p) heterointerface.

Similar to Section 3.2.2, Fig. 3.12a shows the contact resistivity vs. a-Si:H(i) layer thickness for an interface defect density of 10^{10} cm^{-2} and 10^{12} cm^{-2} at the a-Si:H(i)/c-Si(p) heterointerface. Figure 3.12b shows the corresponding simulated FF vs. a-Si:H(i) layer thickness for a full SHJ cell. The simulated contact resistivities (from Fig. 3.12a) for an interface defect density equal to 10^{12} cm^{-2} are shown next to their corresponding FF's. As can be seen, the FF's reduce as the a-Si:H(i) layer thickness increases (for both cases). However, the FF degrades sharply for a case of interface state defect density = 10^{12} cm^{-2}

after 8 nm. Simulations indicate that FF degradation is small (~0.04) when $\rho_c < 0.8$ Ω-cm^2, however the degradation is significant when $\rho_c > 3$ Ω-cm^2.

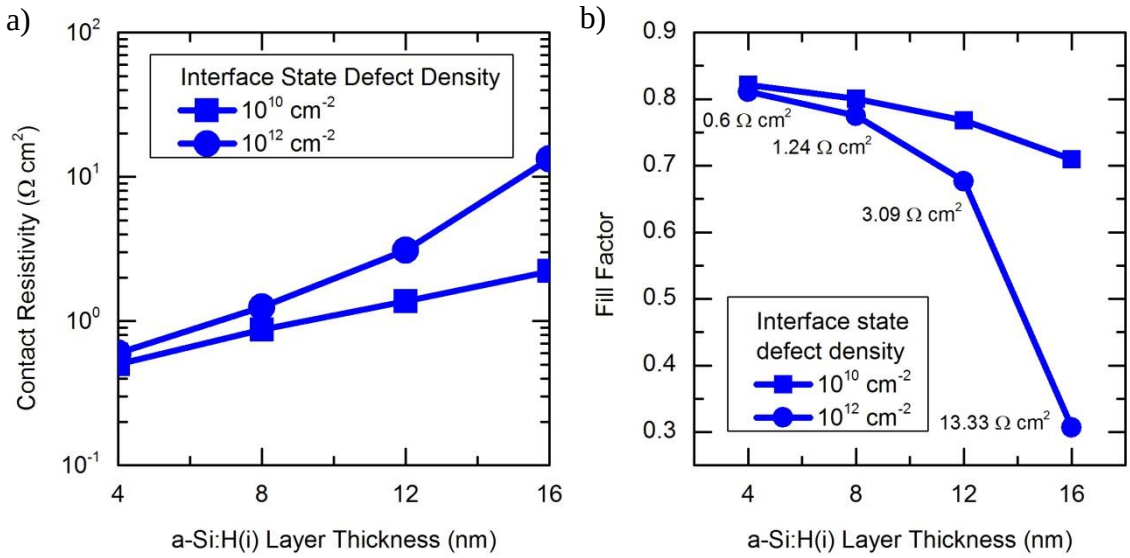

Figure 3.12. a) Simulated contact resistivities for different interface state defect densities at the a-Si:H(i)/c-Si(p) hetero-interface vs. a-Si:H(i) layer thickness. b) Simulated Fill Factor (for different interface state defect densities) vs. a-Si:H(i) layer thickness.

3.3 Conclusion

In this chapter, simulations were conducted using the TCAD tool SILVACO to understand the effect of the ITO/a-Si:H(p) and a-Si:H(i)/c-Si heterointerfaces on transport of carriers and device performance. The ITO was explicitly treated as a n-type doped semiconductor, and hence the effect of the ITO(n^+)/a-Si:H(p) junction on contact resistivity of the hole contact was quantified. Simulations conducted in this chapter determined that band to band tunneling is the dominant transport mechanism at the ITO(n^+)/a-Si:(p) junction. Also, thermionic emission is the limiting transport mechanism across the a-Si:H(i)/c-Si heterointerface at low temperatures.

Several simulation studies conducted previously treated the ITO as a metallic contact with a workfunction. This treatment becomes problematic as the ITO is a low workfunction material which is sputtered on top of a high workfunction a-Si:H(p) layer. This creates a Schottky barrier at the ITO/a-Si:H(p) heterointerface which suppresses transport of carriers. Simulations tend to suffer from convergence issues when experimental values of the ITO workfunction are used (which are low) and unrealistic material parameters are used in order to match experimental trends. However, in this chapter, the treatment of the ITO as a n-type semiconductor reveals that a low workfunction ITO (highly doped) leads to ideal conditions for band to band tunneling. This also leads to a more stringent set of realistic parameters that can be used to conduct the simulations.

While we did pay attention to transport of carriers across the ITO(n^+)/a-Si:H(p) and a-Si:H(i)/c-Si heterointerface, we did not consider the role of defects in transport. Some experimental and simulation studies have suggested the possibility of multi-phonon assisted (hopping) transport across the a-Si:H(i)/c-Si layer; this effect was not included in the simulations conducted in this chapter. The inclusion of defect transport may add another layer of insight to the transport of carriers, as we can further understand when defects act as recombination centers, and if they can be used to improve device performance. The methodology presented in this chapter can be used to investigate novel carrier selective contacts such as MoO_x and WoO_x which are still in the early stages of being evaluated for the purposes of SHJ solar cells.

Even though the simulations conducted in this chapter provide great insight into transport of carriers in hole contacts and their effect on contact resistivity, an inherent

limitation of such simulations arises from the assumptions made to drive a convenient drift-diffusion model. The drift-diffusion model is derived from the Boltzmann transport equation by making several assumptions, such as velocity saturation of carriers, thermal energy distribution of carriers etc. The research conducted in this thesis will attempt to go beyond the limiting assumptions of the drift-diffusion model while studying transport in SHJ solar cells.

Table I

Base parameters used for simulations in Chapter 3

Parameters	ITO	a-Si:H(p/i)	c-Si
χ (eV)	4.5	3.9/3.9	4.05
E_g (eV)	3.7	1.72/1.70	1.12
Conduction Band DOS	7.91×10^{17}	$2.5 \times 10^{20}/2.5 \times 10^{20}$	2.28×10^{19}
Valence Band DOS	7.91×10^{17}	$2.5 \times 10^{20}/2.5 \times 10^{20}$	1.04×10^{19}
Electron Mobility (cm^2/Vs)	50	0.5/0.5	800
Hole Mobility (cm^2/Vs)	50	0.1/0.1	400
Peak Density of Band Tail States (cm^{-3})	10^{18}	$10^{18}/10^{18}$	10^{18}
Peak Density of Mid-Gap States (cm^{-3})	10^{16}	$10^{16}/10^{16}$	10^{16}
Doping (cm^{-3})	10^{20}	$1.8 \times 10^{20}/ 10^{14}$	5×10^{15}
Thickness (nm)	70	15/10	180×10^3

CHAPTER 4

ENSEMBLE MONTE CARLO

In Chapter 2 and Chapter 3, the theoretical framework for drift-diffusion modeling was introduced and used to study cell level properties of SHJ solar cells. It has also been established that the standard drift-diffusion model is limited by the inherent assumptions made while deriving it from the BTE. In particular, the standard drift-diffusion models that are used to study electrical characteristics of solar cells assumes low electric fields. Thus, such a model is not well suited for studying hot carrier effects. In the case of SHJ solar cells, there are two crucial regions where the standard drift-diffusion formulation may break down, and therefore requires a more complete theoretical analysis. Firstly, the high electric field region at the a-Si:H(i)/c-Si heterointerface which results from the band discontinuity, and secondly, the a-Si:H(i) layer where defect assisted transport may be dominant. In this chapter, the implications of high electric fields at the a-Si:H(i)/c-Si heterointerface will be discussed.

Previously, Ghosh *et al.* [53] used ensemble Monte Carlo (EMC) simulations to investigate the effect of high electric fields on photogenerated holes at the a-Si:H(i)/c-Si heterointerface using a single band model. In this chapter, an in-house EMC solver is presented which extends the EMC approach developed by Ghosh *et al.* to model high field effects. A three-band warped non-parabolic model was developed and implemented to accurately simulate high field transport of photogenerated holes. This chapter describes the bulk EMC model and the implementation of a particle-based device simulator to study the effects of high fields at the a-Si:H(i)/c-Si heterointerface on photogenerated holes.

4.1 Bandstructure

The valence band in c-Si consists of a heavy hole, light hole and split off band. As the heavy hole and light hole bands co-exist at the Γ point, this causes warping of the heavy and light hole bands, which is represented by the dispersion relation in Eq. 4.1. It is also important to note that warping of the bands causes the effective mass to have an angular dependence. Figure 4.1 shows a schematic diagram of the 3-band model that has been implemented

$$E(k) = \frac{|A|\hbar^2 k^2}{2m_0}\left[1 \mp g(\theta,\varphi)\right] \tag{4.1}$$

where, $'-'$ refers to heavy holes, $'+'$ refers to light holes and m_0 is the fundamental mass of a free electron The term $g(\theta,\varphi)$ is defined as

$$g(\theta,\varphi) = \left[\left(\frac{B}{A}\right)^2 + \left(\frac{C}{A}\right)^2\left(\sin^2\theta\cos^2\theta + \sin^4\theta\cos^2\varphi\sin^2\varphi\right)\right]^{\frac{1}{2}} \tag{4.2}$$

where θ and φ are the polar and azimuthal angles of the wave vector k. A, B and C are inverse valence band parameters where A = -4.22, B = -0.78 and C = 4.80. The split off band is considered to be parabolic in nature and is 44 meV below the top of the valence band [54] with an effective mass ~ $0.15m_0$.

To consider the effect of non-parabolicity in the heavy and light hole bands, an energy dependent factor $\beta(E)$ is introduced into the dispersion relation [55].

$$E(k) = \left(1-\beta(E)\right)\frac{|A|\hbar^2 k^2}{2m_0}\left[1 \mp g(\theta,\varphi)\right] \tag{4.3}$$

The introduction of the non-parabolicity factor creates an implicit equation. To make things easier, $\beta(E)$ is approximated by a piecewise continuous second order equation

$$1-\beta=\begin{cases}1.0-43.0E+1200\,;0\le \mathrm{E}<0.015\\ 0.8006-14.3632\,\mathrm{E}+177.3117\,\mathrm{E}^2\,;0.015\le E<0.040\\ 0.6434-4.3521E+25.2716E^2\,;0.040\le E<0.100\\ 0.46087\,;E\ge 0.100\end{cases} \tag{4.4}$$

$$1-\beta=\begin{cases}1.0-14.419E+106.7E^2\,;0\le \mathrm{E}<0.050\\ 0.7946-6.295E+26.37E^2\,;0.050\le E<0.100\\ 0.4286\,;E\ge 0.100\end{cases} \tag{4.5}$$

where Eq. 4.4 applies to heavy holes and Eq. 4.5 applies to light holes. In subsequent sections in this chapter 1-β is simply referred to as β.

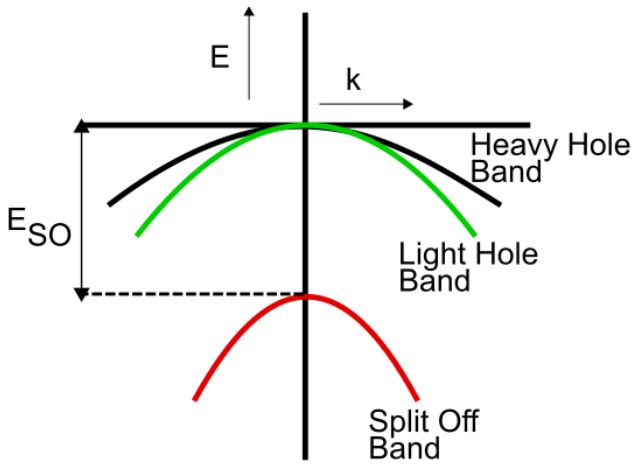

Figure 4.1. Schematic diagram for three band model for the valence band.

4.2 Acoustic Scattering

In this section, a brief derivation for an elastic acoustic scattering rate process considering non-parabolic warped bands is given. This is applicable for heavy and light hole bands, whereas a parabolic scattering rate has been used for the split-off band. To derive the scattering rate associated with acoustic phonons, one starts with the Fermi's golden rule that gives the transition rate from an initial state k to a final state k'

$$\Gamma\left(\mathrm{k}^{'},\mathrm{k}\right)=\frac{2\pi}{\hbar}\left|M_0\right|^2\delta\left(E_{k'}-E_k\right) \tag{4.6}$$

where $\hbar$ is Plank's constant, $\delta(E_{k'}-E_k)$ is the energy conserving delta function and $|M_0|^2$ is the matrix element which is given by

$$\left|M_0\right|^2=\frac{\Xi_{ac}^2 kT}{2\rho V V_s^2} \tag{4.7}$$

where Ξ_{ac} is the deformation potential, V_s is the sound velocity and k is Boltzmann's constant. The total scattering rate out of an initial state k is defined by summing over all possible final states k'. Namely

$$\Gamma\left(E\right)=\sum_{k'}\Gamma\left(k',k\right)=\frac{V}{\left(2\pi\right)^3}\frac{2\pi}{\hbar}\left|M_0\right|^2\iiint \mathrm{k}^{'2}\,\delta\left(E_{k'}-E_k\right)\sin\theta\,\mathrm{d}\theta\,\mathrm{d}\phi\,\mathrm{dk}' \tag{4.8}$$

Differentiating E (Eq. 4.1) w.r.t k we obtain,

$$\frac{dE}{\beta}+E\left(-\frac{1}{\beta^2}\right)\left(b+2CE\right)dE=\frac{\left|A\right|\hbar^2 k\,dk}{m_0}\left[1\pm g\left(\theta,\phi\right)\right] \tag{4.9}$$

$$k\,dk=\frac{m_0}{\left|A\right|\hbar^2}\left[\frac{a-CE^2}{\beta^2}\right]\frac{dE}{1+g\left(\theta,\phi\right)} \tag{4.10}$$

where k can be written as

$$k = \frac{\sqrt{2m_0 E}}{\hbar}\frac{1}{\sqrt{\beta}}\frac{1}{\sqrt{A}}\frac{1}{\sqrt{1 \pm g(\theta,\phi)}} \tag{4.11}$$

Combining Eq. 4.9-4.11, the RHS of Eq. 4.8 can be written as

$$\begin{aligned}\iiint \mathrm{k}'^2\,\delta(E_{k'} - E_k)\sin\theta\,\mathrm{d}\theta\,\mathrm{d}\phi\,\mathrm{dk}' &= \iiint \frac{\sqrt{2m_0 E}}{\hbar}\frac{1}{\sqrt{B}\sqrt{A}\sqrt{1 \pm g(\theta,\phi)}} \\ \times\frac{m_0}{|A|\hbar^2}\left[\frac{a - cE^2}{\beta^2}\right]&\frac{dE}{\left[1 \pm g(\theta,\phi)\right]}\delta(E_{k'} - E_k)\sin\theta d\theta d\phi\end{aligned} \tag{4.12}$$

On further solving we get

$$\begin{aligned}\iiint \mathrm{k}'^2\,\delta(E_{k'} - E_k)\sin\theta\,\mathrm{d}\theta\,\mathrm{d}\phi\,\mathrm{dk}' &= \frac{\sqrt{2}m_0^{3/2}\sqrt{E}}{\hbar^3\beta^{5/2}|A|^{3/2}} \\ \times\left(a - CE^2\right)\iint &\frac{\sin\theta d\theta d\phi}{\left[1 + g(\theta,\phi)\right]^{3/2}}\end{aligned} \tag{4.13}$$

Finally, using Eq. 4.13, we can calculate the total energy dependent scattering rate as

$$\Gamma(E) = \frac{\Xi_{ac}^2 kT\sqrt{E}}{4(2\pi)^2\hbar\rho V_s^2}\left[\frac{2m_0}{\hbar^2|A|}\right]^{3/2}\left[\frac{a - CE^2}{\beta^{5/2}}\right]\iint\frac{\mathrm{G}(\theta)\sin\theta d\theta d\phi}{\left[1 + g(\theta,\phi)\right]^{3/2}} \tag{4.14}$$

where $G(\theta)$ is the overlap integral and it approximated as described by Wiley [56].

4.3 Non-Polar Optical Phonon Scattering

An expression for non-polar optical scattering can be derived by using a similar approach as for acoustic phonons in Section 4.2. The matrix element for non-polar optical phonons is given by

$$|M_0|^2 = \frac{\hbar D_0^2}{2\rho V w}\begin{bmatrix} N_0 \\ N_0 + 1\end{bmatrix}\delta(E_{k'} - E_k \pm h\omega_0) \tag{4.15}$$

where D_0 is the optical deformation potential, ρ is the density, and N_0 is the phonon occupation number which is given by

$$N = \frac{1}{e^{\frac{\hbar\omega_0}{kT}} - 1} \tag{4.16}$$

where $\hbar\omega_0$ is the optical phonon energy. Following a similar procedure as in Section 4.2, the triple integral representing the total scattering from an initial state k' to all final states is given by

$$\begin{aligned} &\iiint \mathrm{k}'^2\, \delta\left(E_{k'} - E_k \pm \hbar\omega_0\right) \sin\theta\, \mathrm{d}\theta\, \mathrm{d}\phi\, \mathrm{dk}' = \frac{\sqrt{2} m_0^{3/2} \sqrt{E'}}{\hbar^3 \beta^{5/2} |A|^{3/2}} \left(a - CE'^2\right) \\ &\times \iint \frac{\sin\theta d\theta d\phi}{\left[1 + g\left(\theta, \phi\right)\right]^{3/2}} \end{aligned} \tag{4.17}$$

where $E' = E \pm \hbar\omega_0$. On solving Eq. 4.17, we obtain the energy dependent scattering rate, given by

$$\Gamma(E) = \frac{D_0^2}{4(2\pi)^2 \rho\hbar\omega} \left[\begin{matrix} N_0 \\ N_0 + 1 \end{matrix}\right] \left[\frac{2m_0}{\hbar^2 |A|}\right]^{3/2} \sqrt{E} \frac{\left[a - CE^2\right]}{\beta^{5/2}} \iint \frac{\mathrm{G}(\theta) \sin\theta d\theta d\phi}{\left[1 + g\left(\theta, \phi\right)\right]^{3/2}} \tag{4.18}$$

where $G(\theta)$ is treated according to [38].

4.4 Selection of Final States

The final states for the scattering mechanisms have to be calculated using a rejection mechanism as all scattering mechanism have an angular dependence [57]. A final angle is selected if it satisfies the condition

$$r \leq \frac{f\left(\theta_r, \varphi_r\right)}{f_{\max}} \tag{4.19}$$

where *r* is a random number from a uniform probability distribution, and *f* is the angular distribution function. More details on the implementation of the rejection mechanism can be found in [39].

4.5 Drift Velocity

Due to the warped non-parabolic nature of valence bands, the drift velocity has an angular and energy dependence. The drift velocity is given by

$$v = \frac{1}{\hbar}\frac{\delta E(k)}{\delta k} \tag{4.20}$$

where $E(k)$ is obtained from the dispersion relation given in Eq. 4.3, where the *1-β* can be represented as β.

$$\frac{\delta E}{\delta k} = \frac{|A|\hbar^2 k}{m_0}\left[1 \pm g(\theta,\phi)\right]\frac{\beta^2}{\left(a - CE^2\right)} \tag{4.21}$$

Substituting Eq. 4.21 in Eq. 4.20.

$$v = \frac{1}{\hbar}\frac{\delta E}{\delta k} = \frac{|A|\hbar k}{m_0}\left[1 \pm g(\theta,\phi)\right]\frac{\beta^2}{\left(a - CE^2\right)} \tag{4.22}$$

4.6 Theoretical Model

In this chapter, a theoretical model is presented to understand the origin of hot carriers in SHJ solar cells. To understand the effect of high electric fields on photogenerated holes, a simulation model is presented that combines the drift-diffusion and bulk EMC methods. Figure 4.2a shows a schematic diagram of a SHJ solar cell, where drift-diffusion simulations were conducted over the entire domain using a commercial TCAD tool (SILVACO), and the EMC solution was applied to a very small area near the a-Si:H(i)/c-

Si heterointerface. The simulations presented in this chapter do not consider the transparent conduction oxide (TCO) and the silver (Ag) contacts.

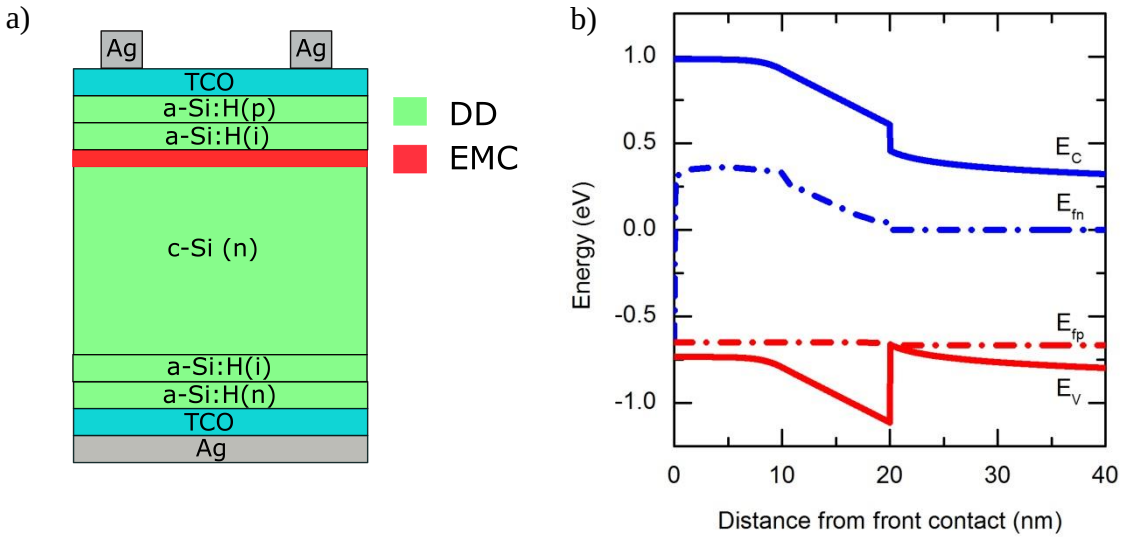

Figure 4.2. a) Schematic diagram of SHJ solar cell with the simulation domains. The EMC solution is applied in the c-Si region near the a-Si:H(i)/c-Si heterointerface. b) Simulated band diagram at maximum power point ~ 0.65 V.

Figure 4.2b shows the simulated band diagram of the SHJ cell at the maximum power point (~0.65 V). The simulated device considers a 10 nm thick a-Si:H(i) passivation layer. In order to generate potentials for a realistic device, the interface defect distribution at the a-Si:H(i)/c-Si heterointerface and the defect distribution in the a-Si:H bulk layers are considered [58]. From Fig. 4.2b we can see that the band bending due to the a-Si:H(i)/c-Si heterointerface extends well into the c-Si layer. Figure 4.3 shows the electric field profile in a strongly inverted SHJ solar cell, which corresponds to the band bending shown in Fig. 4.2b. The photogenerated minority carrier holes traverse this high field or "inversion" region in the c-Si near the a-Si:H(i)/c-Si heterointerface in order to be collected as majority carriers in the a-Si:H(p) emitter layer.

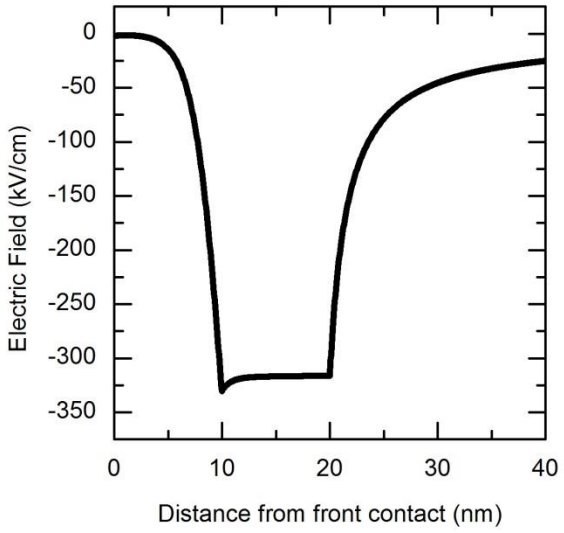

Figure 4.3. Electric field at the front contact for a strongly inverted a-Si:H(i)/c-Si heterointerface in a SHJ solar cell at maximum power point voltage ~ 0.65 V.

Similar to the methodology outlined by Ghosh *et al.* in [35], an Ensemble Monte Carlo (EMC) solver (discussed in the previous section) is employed to study hole transport in the high electric field region in the c-Si near the a-Si:H(i)/c-Si heterointerface. At first the potential and the electric field profiles are calculated at the maximum power point by the drift-diffusion model. Using these parameters as an input, the EMC solution is applied in the c-Si near the a-Si:H(i)/c-Si heterointerface (as shown in Fig. 4.4). The EMC domain extends from the edge of the a-Si:H(i)/c-Si heterointerface into the quasi-neutral regions of the c-Si with low electric fields < 5 kV/cm; thus, the EMC domain ~ 100-200 nm.

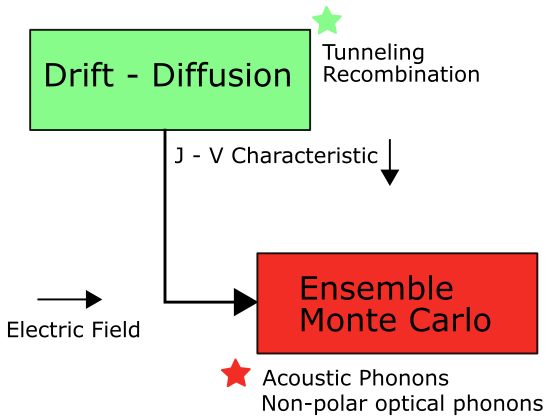

Figure 4.4. Flow of information between the drift-diffusion solver and the EMC solver. Also shown in this figure are the corresponding physical processes incorporated in the theoretical models of the corresponding solvers.

The EMC domain is populated by injecting holes into the domain to replicate a current of 40 mA/cm^2. The injection is performed at the boundary placed in the quasi-neutral c-Si region. A certain number of carriers are injected into the domain every 10 fs with a Maxwellian energy distribution and a half-Maxwellian momentum distribution. Reflective boundary conditions are implemented at this boundary to prevent the carriers from leaving the EMC domain (see Fig. 4.5). The simulation is conducted until the extracted current matches the injected current, and the domain population has stabilized. The extraction boundary is placed at the a-Si:H(i)/c-Si heterointerface. There are two strategies that were implemented to allow carriers to exit the EMC domain via the extraction boundary: 1) a tunneling coefficient was computed using the WKB method, and 2) a fictitious tunneling coefficient was used, i.e. manually setting the tunneling coefficient. A random number was generated, and then compared to the tunneling coefficient to select carriers for extraction. Finally, when steady state is achieved, the energy distribution function of holes at the a-

Si:H(i)/c-Si heterointerface is analyzed. It is important to note that the main purpose of these simulations is to observe the energy distribution function of the holes at the a-Si:H(i)/c-Si heterointerface.

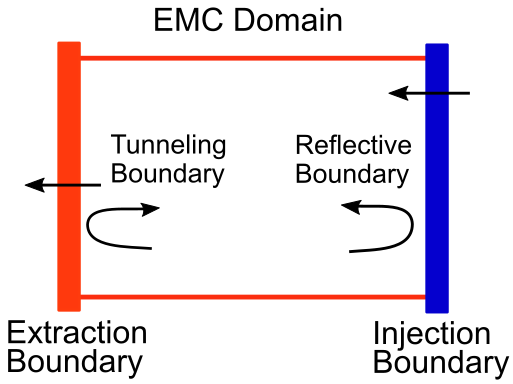

Figure 4.5. Visualization of the boundary conditions of the EMC domain.

It should be noted that certain assumptions need to be made in order to justify the application of an EMC solver in solar cells. The EMC solves for hole transport in the c-Si absorber in the SHJ solar cell which is n-type doped (see Fig. 4.2a). However, due to the properties of the a-Si:H(i)/c-Si heterointerface, the surface density of minority carrier holes is orders of magnitude higher than the majority carrier electrons. The EMC solver is applied in this region where the minority carrier hole density is much higher than the majority carrier electron in the c-Si absorber layer. However, at some point in the quasi-neutral low field region, the majority carrier electron density surpasses the minority carrier hole density. It is assumed that there is no recombination of minority carrier holes in the EMC domain (including at the a-Si:H(i)/c-Si heterointerface); this is a fair assumption as the minority carrier hole density >> majority carrier hole density. Also, it is assumed that most

of the generation takes place outside the inversion region in the quasi-neutral region. The EMC simulator monitors the progress of photogenerated carriers in real space by calculating energy, velocity and real space positions.

4.7 Results and Analysis

As mentioned in Chapter 2, the drift-diffusion model does not account for the non-local effects of high field transport.

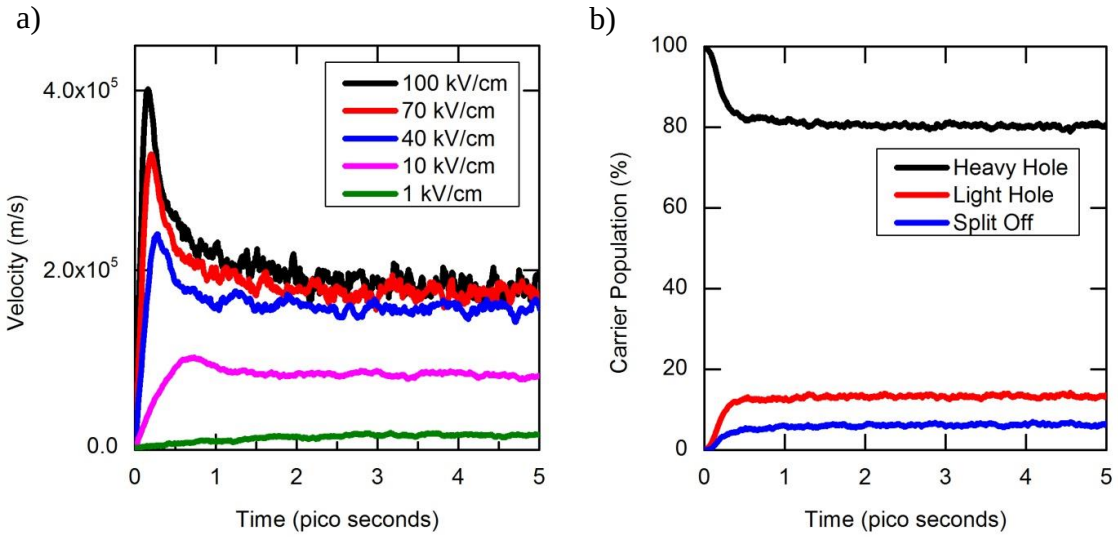

Figure 4.6. Ensemble Monte Carlo simulation results for warped non-parabolic bands: a) Velocity vs. time for different electric fields. b) Population of carriers in each band.

Figure 4.6a shows the transient velocity characteristics of holes for warped non-parabolic bands. Figure 4.6b shows that around 80% of the population resides in the heavy hole band, thus the warping is important to describe valence band transport characteristics.

A SHJ solar cell with a $V_{OC} \approx 730$ mV and an efficiency (η) $\approx 23\%$ was simulated using the drift-diffusion model. The simulated structure considered an a-Si:H(p) emitter layer of 7 nm thickness with doping $N_A \sim 10^{19}$ cm^{-3}, and an a-Si:H(i) passivation layer of 10 nm

thickness. As discussed previously, initially the drift-diffusion model simulates the electrical characteristics of the entire device. Then the EMC is applied at the high electric field a-Si:H(i)/c-Si heterointerface (see Fig. 4.2a). The results presented in this section considered a 3-band warped non-parabolic approach (unless mentioned otherwise) to study the correlation between electric fields at the a-Si:H(i)/c-Si interface on the energy distribution function of the photogenerated holes.

Figure 4.7 shows the energy distribution function (EDF) of the photogenerated carriers at the a-Si:H(i)/c-Si heterointerface for varying passivation at the heterointerface. A high quality heterointerface is achieved by having good chemical passivation, i.e. low interface state defect density. A low interface state defect density facilitates high electric fields at the a-Si:H(i)/c-Si heterointerface. Figure 4.7a shows the EDF of photogenerated holes when the interface state defect density (D_{it}) ~ 10^{10} cm^{-2}, this scenario corresponds to devices with high efficiency. Figure 4.7b and Fig. 4.7c shows the EDF of photogenerated holes for interface state defect densities > 10^{11} cm^{-2}. It is quite clear that the EDF is non-Maxwellian in every case [59]. However, it can be seen that the average energy of the hole distribution decreases with increasing interface state defect density at the a-Si:H(i)/c-Si heterointerface. This is because an increase in the interface state defect density at the a-Si:H(i)/c-Si leads to a reduction of the electric field at the heterointerface. In 0, it is shown that the average energy of the photogenerated carriers affects the transport of photogenerated holes across the a-Si:H(i) passivation layer.

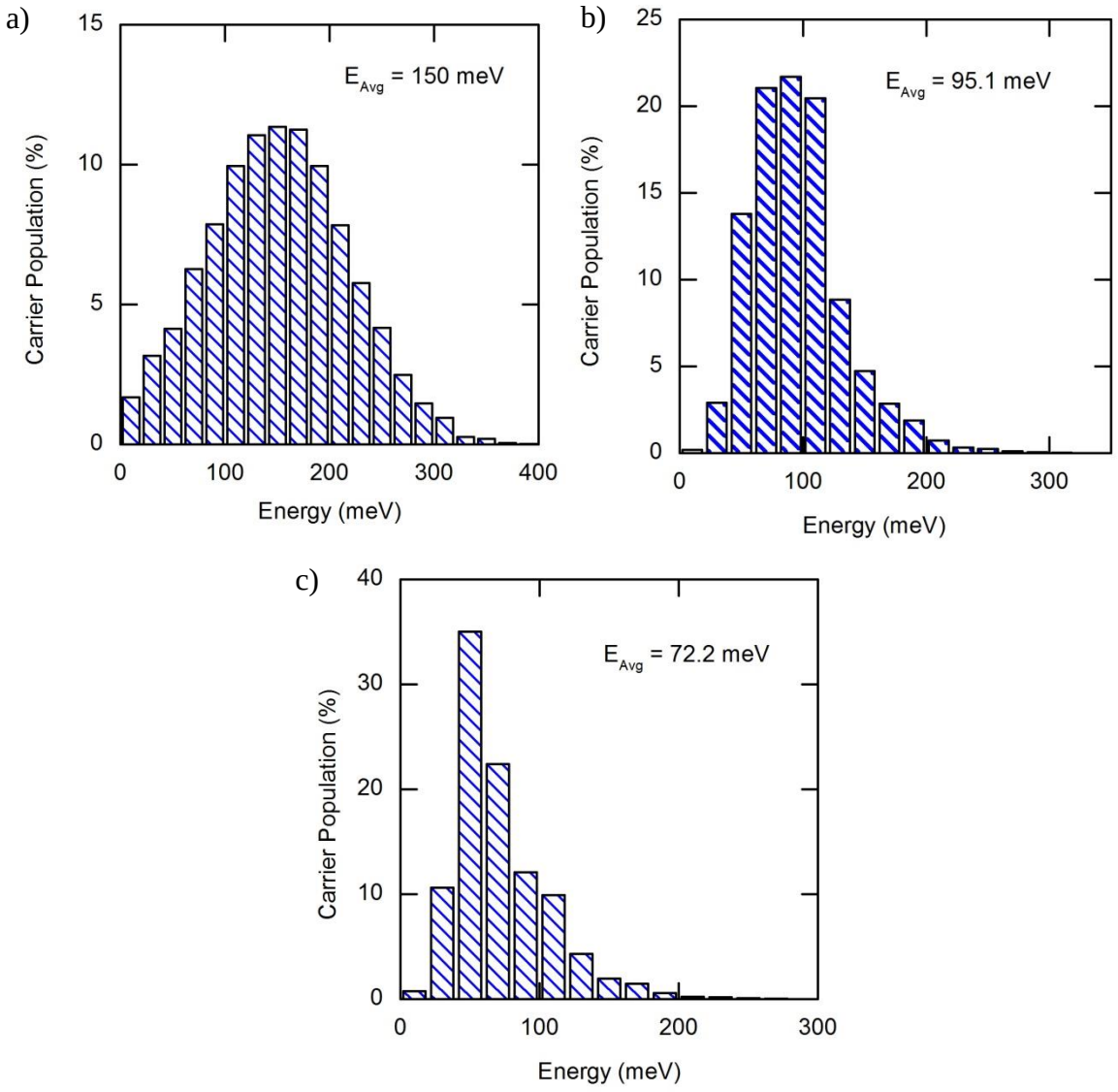

Figure 4.7. Energy distribution function of photogenerated carriers at the a-Si:H(i)/c-Si heterointerface for an interface state defect density of a) 10^{10} cm^{-2}, b) and c) >10^{11} cm^{-2}.

Figure 4.8a shows the EDF of photogenerated holes for a poorly passivated a-Si:H(i)/c-Si heterointerface. The poor passivation (D_{it} ~ 10^{12} cm^{-2}) leads to lower electric fields at the a-Si:H(i)/c-Si heterointerface. However, the average energy of the hole carrier population is still > thermal equilibrium (≈ 38 meV). In contrast, the average energy of the

hole carrier population in the quasi-neutral (low field) region is shown to be ~ 42.4 meV (see Fig. 4.8b), which is similar to the assumption of thermal equilibrium. Thus, it can be concluded that while the Maxwellian assumption works well for low field regions, it is an inaccurate assumption for high field scenarios.

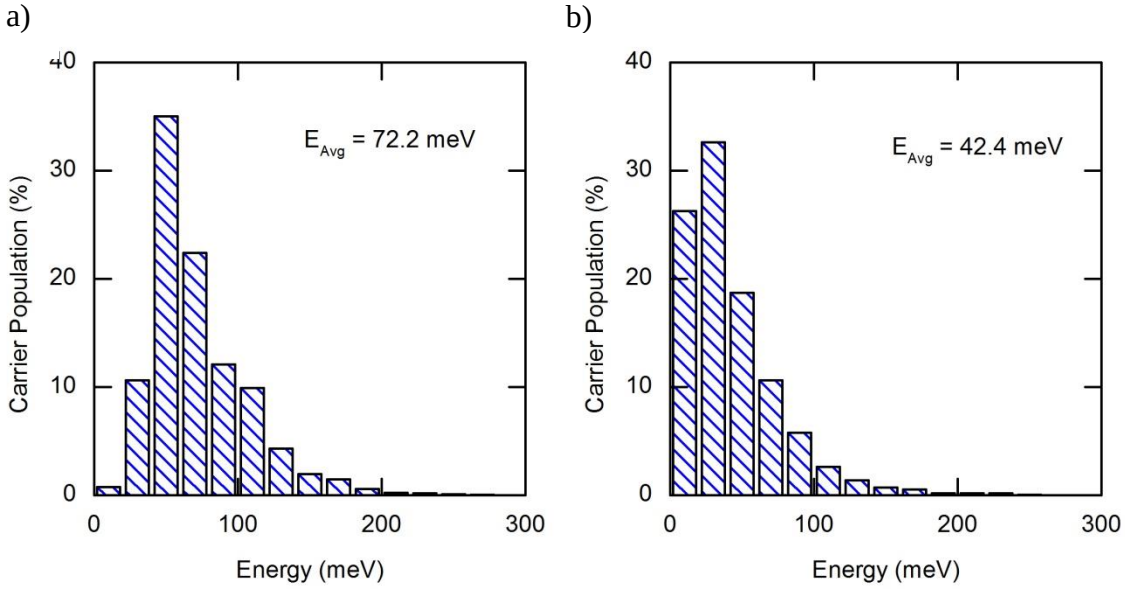

Figure 4.8. a) EDF of the photogenerated carriers at the heterointerface for a weakly inverted device. b) EDF in the quasi neutral region.

Figure 4.9 shows a comparison between the 3-band warped model vs. a single band parabolic model for a poorly passivated (D_{it} ~ 10^{12} cm^{-2}) a-Si:H(i)/c-Si heterointerface. Simulations indicate that the single band model underestimates the energy of the hole carrier population.

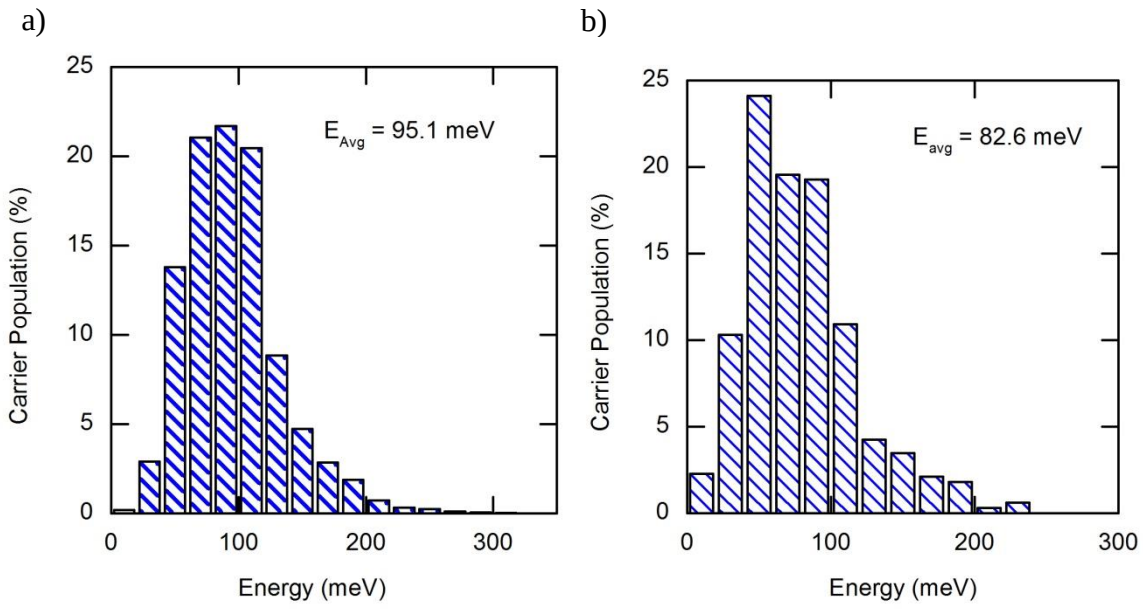

Figure 4.9. a) EDF using the three-band approach. b) EDF using a single parabolic band approach.

4.8 Conclusion

In this chapter, an EMC technique was applied to a SHJ solar cell structure to determine the effect of high electric fields on transport of photogenerated holes at the a-Si:H(i)/c-Si heterointerface. The EMC simulations determined that the high electric fields at the a-Si:H(i)/c-Si heterointerface cause the photogenerated holes to exhibit non-Maxwellian behavior, however, simulations also showed that a Maxwellian distribution in the quasi-neutral regions is accurate. In this chapter, only acoustic phonon and non-polar optical phonon scattering were considered. However, the EMC domain considers the a-Si:H(i)/c-Si heterointerface, where the hole density (minority carrier) is many orders of magnitude higher than the electron density (electron density) at the heterointerface, thus making the

surface "inverted". A carrier-carrier scattering model would be a useful model to include into the bulk EMC to further the understanding of the hole behavior at the heterointerface.

To understand the role of the a-Si:H(i) passivation layer on overall SHJ solar cell device properties, there are two regions that have transport properties that might deviate from semi-classical principles, namely, 1) the high electric field region at the a-Si:H(i)/c-Si heterointerface and 2) the a-Si:H(i) passivation layer itself. While the EMC is a perfect tool to analyze the high field behavior, it is not an ideal methodology to study defect transport. The EMC methodology is a solution to the BTE which is constricted in time by scattering rates which are femtosecond phenomena, however, transport across the a-Si:H layer is described by defect assisted transport which involves capture and emission processes by defects. These mechanisms happen on much larger time scales (10^{-9} - 10^{-3} sec) as compared to scattering phenomena. In the next chapter we introduce the kinetic Monte Carlo and its role in studying defect assisted transport.

CHAPTER 5

KINETIC MONTE CARLO

In Chapter 4, the behavior of photogenerated carriers at the a-Si:H(i)/c-Si heterointerface was studied using the ensemble Monte Carlo technique. This chapter focuses on the transport of photogenerated carriers across the a-Si:H(i) passivation layer. The concept of carrier selective contacts has previously been introduced in this thesis. For the purposes of a SHJ solar cell, a heterojunction stack comprised of a transparent conducting oxide (TCO), doped *a*-Si:H, and *a*-Si:H(i) on top of a *c*-Si absorber forms a contact structure that is selective to the transport of electrons/holes, as shown in Fig. 5.1a. Figure 5.1b shows that for an *a*-Si:H(*p*) emitter layer at the front contact, the *a*-Si:H(*i*) layer forms a potential barrier that impedes the collection of photogenerated holes that are generated in the *c*-Si absorber layer. However, this layer is critical for the performance of SHJ solar cells as it passivates the interface between the doped *a*-Si:H and *c*-Si; this allows the device to obtain high V_{oc}'s and, consequently, high efficiencies [3]. *a*-Si:H is an inherently defective material due to the presence of strained and dangling bonds in the amorphous Si structure, resulting in the formation of band tails comprised of localized states, and mid-gap defect states. Transport of photogenerated holes through this barrier has been a subject of much discussion and research. Temperature dependent current-voltage (J-V) [17] and capacitive decay experiments [15] have led to conclusions that defect assisted transport across the barrier plays a very important role in the collection of photogenerated carriers. However, most simulation studies that analyze the electrical

behavior of SHJ solar cells do not explicitly study defect assisted transport across the *a*-Si:H(*i*) barrier [19,21,41].

In this chapter, multi-phonon defect assisted transport of holes through the *a*-Si:H(*i*) passivation layer in a SHJ solar cell is simulated using an in-house kinetic Monte Carlo (KMC) simulator that was developed as part of this dissertation. The unique problem associated with defect assisted transport is that the time associated with defect capture/emission transitions can vary several orders of magnitude depending upon the nature of defects. The KMC approach allows consideration of processes with widely different time scales because it is an event driven methodology. In recent years, the KMC methodology has been applied to a wide variety of problems such as: processing issues - the creation and migration of defects during various process steps [61], leakage currents through high-κ dielectrics [62], charge transport in organic light emitting diodes [63], current-voltage characteristics of polymer solar cells [64], growth conditions of crystals [65], organic solar cells [66] and polymer solar cells [67]. It has also been used to study transport and leakage mechanisms in dielectric materials that are used in memories [68]. The next generation of materials being investigated for the purposes of forming carrier selective contacts include many transition metal oxides (TMO's). In particular, titanium oxide (TiO_x) has been reported as an electron selective contact [69], and tungsten oxide (WoO_x) and molybdenum oxide (MoO_x) have been investigated as hole selective contacts [63,64]. These materials have unique defect states due to the presence of oxygen. Thus, defect chemistry and defect assisted transport need to be given special consideration in the transport properties of carrier selective contacts. There are several simulation studies in

literature that have investigated novel TMO's for the purposes of CSC solar cells [65,66]. However, these studies use commercial tools that greatly simplify the description of defect assisted transport.

The kinetic Monte Carlo (KMC) algorithm is a stochastic method to solve a Markov chain. This method was initially used to study the physics of surface reactions; a model to describe physics at the atomistic level and relate it to microscopic kinetics. In other words, a study of the individual atoms reacting at the surface and correlating these reactions to macroscopic characteristics such as reaction rates of the adsorbates [74]. Therefore, a unique problem emerged in terms of time scales as the motion of atoms occurs over a period of femtoseconds and the macroscopic properties vary over a much larger time period. Typically, a Molecular Dynamics (MD) approach can be used to study such a system. However, a MD approach discretizes time in equal lengths which is determined by vibration of the chemical bonds. Therefore, even though a MD approach is ideal to study microscopic properties at sub picosecond time scales, it is computationally extremely expensive to study macroscopic behavior at larger time scales [75]. To fully correlate microscopic phenomena at short time scales with macroscopic phenomena at larger time scales it is necessary to bridge the time scales. The KMC proves to be a very effective tool in bridging the information between different time scales [76].

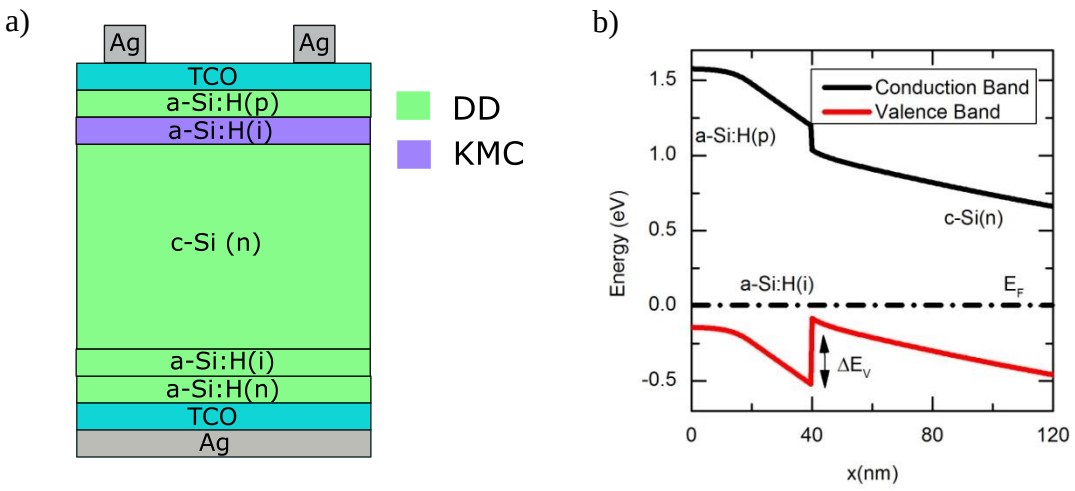

Figure 5.1. a) Schematic diagram of the SHJ solar cell indicating the drift-diffusion and KMC simulation domains and b) the energy band diagram of a SHJ solar cell at equilibrium at the front contact.

5.1 Defect Assisted Transport

Most commercial simulators employ the drift-diffusion model to study the electrical characteristics of solar cells. While this model is more than sufficient for describing low field diffusive transport; any non-idealities or deviation from semi-classical transport is added as a correction factor to the generation-recombination terms or as a boundary condition to the current equations. Trap assisted tunneling is usually added as a correction to the Shockley-Read-Hall recombination term by using a field effect term $'\Gamma'$ (Eq. 5.1).

$$R_{SRH} = \frac{pn - n_i^2}{\frac{\tau_p}{1+\Gamma_p}\left[n + n_i \exp\left(\frac{E_T - E_i}{kT}\right)\right] + \frac{\tau_n}{1+\Gamma_n}\left[p + n_i \exp\left(\frac{E_i - E_T}{kT}\right)\right]} \tag{5.1}$$

where $\tau_{n,p}$ is the minority carrier lifetime, and E_T is the energy of the trap. There are several models to analytically determine the value of Γ [70,71]. Γ is quite often also utilized as a local quantity which is dependent on local variables. While Γ does include some interaction

with phonons it cannot explicitly describe 'hopping'. Hopping transport is crucial in devices where the transport layer is defective.

In this chapter, a combination of drift-diffusion and KMC methods are used to study transport of photogenerated carriers across the a-Si:H(i) passivation layer. As shown in Figure 5.1a, drift-diffusion modeling is employed in the bulk of the device structure, while the KMC method is used to study the transport of photogenerated holes across the a-Si:H(i) passivation layer. At first, drift-diffusion simulations are conducted over the entire device domain to obtain the energy band profiles, quasi-Fermi levels and electric fields for a given voltage. The valence band profile, hole quasi-Fermi level, electric field, and band tail defect distribution in the a-Si:H(i) passivation layer are used to setup the KMC solver domain. A hole carrier distribution is initialized at the a-Si:H(i)/c-Si heterointerface, and then the KMC methodology is used to model the transport of carriers across the a-Si:H(i)/c-Si heterointerface and through the a-Si:H(i) passivation layer. All the simulations presented in this chapter consider an a-Si:H(p) layer thickness ~ 10 nm with a doping ~ 10^{19} cm^{-3}. The drift-diffusion and KMC simulations do not include the TCO and the Ag contact.

5.2 Band-Tail Defects

Due to its amorphous nature, a-Si:H has many defect states that arise due to deviations from the crystalline Si structure, which lead to electronic states in the forbidden gap [79]. Primarily, strained Si-Si bonds lead to localized band-tail defect states, which are below and above the conduction and valence band edges respectively, these localized states below/above the band edge can be described by an exponential decay model.

$$N(E,x) = N_{VBT} \exp\left(\frac{-\left(E - E_V(x)\right)}{E_0}\right) \tag{5.2}$$

where N_{VBT} is the peak valence band density of states (~ 2×10^{21} cm^{-3} eV), E_V is the valence band edge energy and E_0 is the characteristic decay/Urbach energy (~ 45 meV) [60]. The occupation of the band-tail states is decided based on the Fermi-Dirac distribution function where the Fermi level is the device Fermi level (Eq. 2.26).

5.3 Mid Gap Defects

Defects in the amorphous silicon bandgap originate from weak Si-Si bonds and dangling Si bonds. It is widely agreed that the density of dangling bonds is caused due to a chemical equilibrium established between the inter conversion of Si-Si weak bonds and Si dangling bonds. The electronic states due to dangling bonds can take up a range of values and charge states including neutral, positive and negative. Thus, dangling bond states are amphoteric in nature. The defect-pool model is an analytical model that can predict the mid-gap defect density in amorphous silicon. In device grade amorphous silicon, most mid-gap states result from singly hydrogenated Si-Si bonds [24]

$$D(E) = \gamma\left(\frac{2}{f^0(E)}\right)^{\frac{kT}{2E_{v0}}} P\left(E + \frac{\sigma^2}{2E_{v0}}\right) \tag{5.3}$$

where E_{v0} is the characteristic energy, $f^0(E)$ is the occupation function for neutral defects and P is a Gaussian function.

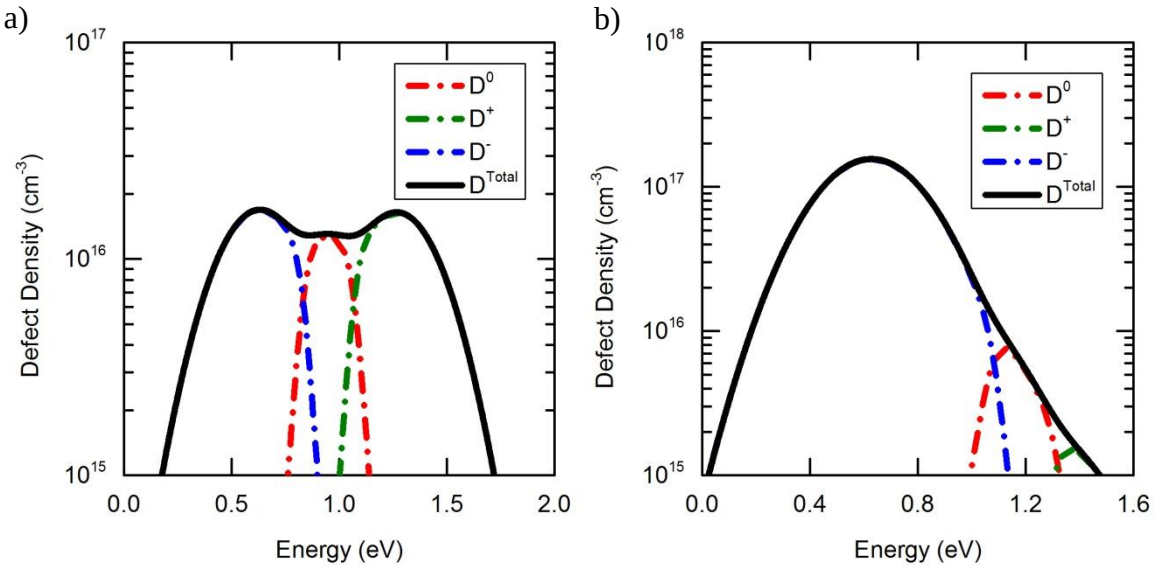

Figure 5.2. Density of mid gap states calculated by the defect-pool model (implemented in Matlab). a) Density of defect states in intrinsic amorphous silicon. b) Density of defect states in n-type silicon.

Figure 5.2 shows the distribution of amphoteric dangling bond states as described by the defect-pool model, where D^0 is a neutral state (occupied by one electron), D^+ is a positively charged state (occupied by zero electrons), and D^- is a negatively charged state (occupied by two electrons). The distribution of mid gap states in a-Si:H(i) is shown in Figure 5.2a where the Fermi level is considered to be 1.05 eV. Figure 5.2b shows the mid gap states of n-type doped a-Si:H with a Fermi level of 1.30 eV. While implementing the defect-pool model, the occupation of the mid-gap states is decided by the device Fermi level (see Eq. 2.29).

5.4 Initialization of the Carrier Distribution

Once the KMC domain is established with the description of band-tail and mid-gap defects in energy space and real space, the carrier distribution of holes at the a-Si:H(i)/c-Si

heterointerface is used as an input. In Chapter 4, an ensemble Monte Carlo method was described which calculates the energy distribution of photogenerated holes at the a-Si:H(i)/c-Si heterointerface [40]. In this section, the initialization of equilibrium (Maxwellian) and far from equilibrium (non-Maxwellian) carrier distributions is described by using analytical techniques.

5.4.1 Maxwellian Distribution

An equilibrium distribution of carriers can be generated by considering a Maxwellian distribution function

$$f(E) = \exp\left(-\frac{E}{E_{av}}\right) \tag{5.4}$$

where E is the energy, and E_{av} is the average energy per particle for a Maxwellian distribution ~ 1.5kT. We apply the inversion method [80] to the normalized cumulative distribution function (shown in Eq. 5.5) in order to use a random number 'r' to generate the Maxwellian distribution

$$\frac{\int_0^E \exp\left(-\frac{E}{E_{av}}\right)}{\int_0^\infty \exp\left(-\frac{E}{E_{av}}\right)} = r \tag{5.5}$$

Solving the integrals in Eq. 5.5 leads to

$$E = -\frac{3}{2} kT \times \ln(r) \tag{5.6}$$

where k is the Boltzmann's constant and T is the temperature and r is random number between 0 and 1.

5.4.2 Gaussian Distribution

A far from equilibrium (non-Maxwellian) distribution can be generated by using a Gaussian distribution function

$$f(E) = \frac{1}{\sqrt{2\pi\sigma^2}} \exp\left(-\frac{(E-\mu)^2}{2\sigma^2} \right) \tag{5.7}$$

where E is the energy, μ is the mean energy of the distribution and σ is the standard deviation. This approach represents a carrier distribution that occurs under the effect high fields (as described in Chapter 4).

5.5 Transition Mechanisms

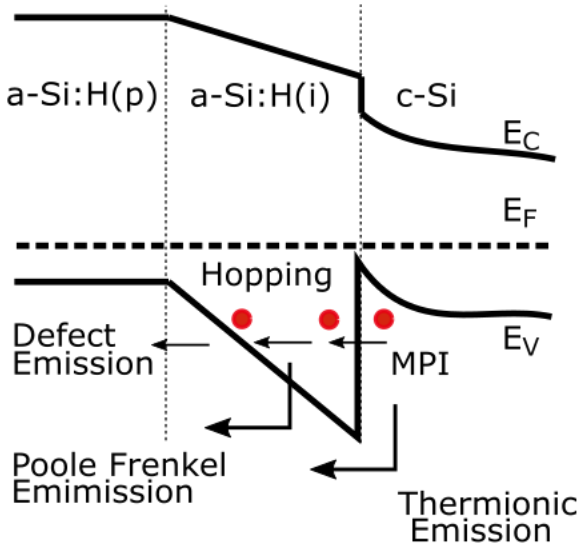

Figure 5.3. Schematic diagram of the various transport mechanisms that assist the photogenerated holes across the barrier layer. We consider multi-phonon injection (MPI) for transitions into the *a*-Si:H(*i*) passivation layer, defect to defect (hopping) mechanisms for transport within the layer, and Poole-Frenkel and multi-phonon defect emission for emission from the layer

In this chapter, the KMC solver simulates quasi-1D transport across the a-Si:H(i) passivation layer. This is done by creating transition rate tables that describe the various physical mechanisms associated with carrier transport. Once the appropriate transition is selected based on the transition tables, we choose the time associated with the selected transition using a second random number. In this section the various transport mechanisms that are considered for injection into the barrier, transport within the barrier, and extraction from the barrier are described (see Fig. 5.3).

5.5.1 Tunneling

In the process of tunneling, a carrier can cross a potential barrier which under semi-classical considerations would otherwise be impossible. This mechanism depends on the height (energy) of the barrier and the thickness (length) of the barrier. In devices at the nano-scale level or devices with novel structures (heterojunctions, quantum wells etc.), tunneling is often a dominant mechanism. Tunneling is often characterized by a tunneling transmission coefficient T(E) which is a measure of the probability that a particle can cross the potential barrier. A simple way of determining the transmission coefficient is given by the Wentzel-Kramers-Brillouin (WKB) method

$$T(E) = e^{-2\int \sqrt{\phi(x)-E}\,dx} \tag{5.8}$$

A more accurate method to describe the transmission coefficient is by using the transfer matrix method [81]. We have implemented the WKB method for simplicity. And after some investigation it was found that for the triangular barrier under consideration, the WKB method and the transfer matrix method gave quite similar results.

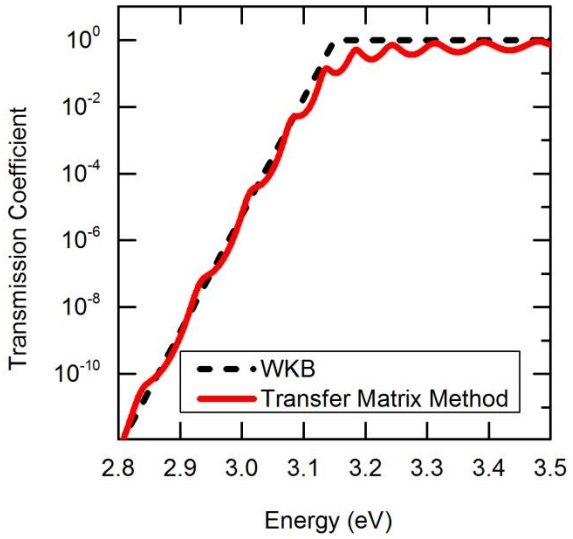

Figure 5.4. Transmission coefficient across a piecewise linear barrier calculated by the WKB method and transfer matrix method.

5.5.2 Elastic Injection and Emission from Traps

The injection of charge from a semiconductor to a defect in an insulator is a crucial mechanism that contributes to current transport in insulators and amorphous materials. In the specific case of the SHJ solar cell being considered in this thesis, a photogenerated hole at the a-Si:H(i)/c-Si heterointerface can be injected into the band-tail states of a-Si:H(i) through an elastic process when energetically allowed. The rate associated with an elastic transition is derived from Fermi's golden rule [82]

$$p = \frac{2\pi}{\hbar}|T|^2 \frac{dn}{dE} \tag{5.9}$$

where T is the matrix element associated with a tunneling transition and dn/dE is the derivative of the density of states. Figure 5.5 shows a schematic diagram of a carrier that is energetically at the same level as the defect state.

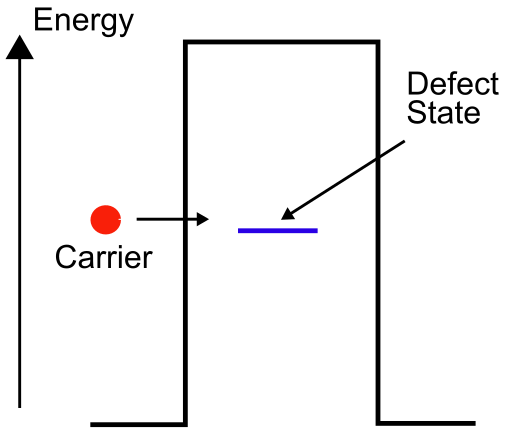

Figure 5.5. Elastic tunneling from conduction band to defect level.

According to Bardeen [83], the matrix element for a tunneling transition can be written as

$$T_{rl} = \int \psi_r^* (H - E_l) \psi_l dr \tag{5.10}$$

where ψ_l is the wave function of the particle, ψ_r is the wave function of the defect, H is the Hamiltonian of the system and E_l is the energy of the particle. The particle (electron/hole) has a plane wave description while the defect is assumed to have an exponentially decaying wave function.

$$\psi_r = \left(\frac{k_D}{2\pi}\right)^{\frac{1}{2}} \frac{e^{-k_D r}}{r} \tag{5.11}$$

where $k_D = 2\pi E_D/\hbar^2$, k_D is the wave vector of the defect and E_D is the energy of the defect w.r.t the band edge. The defect is assumed to have a δ - function like behavior. Figure 5.6 shows the schematic description of wavefunction representation of the carrier and the defect state.

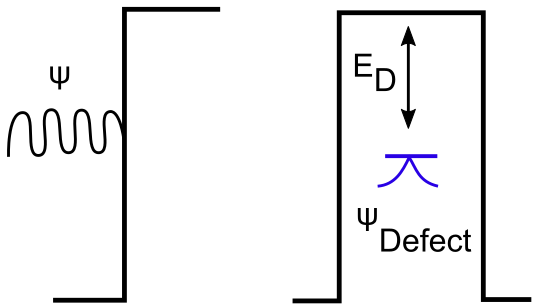

Figure 5.6. Wavefunction description of elastic tunneling.

In Chapter 4, it was shown that in the case of valence bands, the heavy hole and the light hole bands are warped in nature and the split off band is assumed to be parabolic in nature. It was also shown that most of the carriers in the high field region reside in the heavy hole and light hole bands. To accurately represent the physics, the dispersion relation should include the warping of the valence bands. However, warping introduces an angular dependence which makes the derivation quite difficult. Thus, this is a limiting assumption that has been employed in this thesis in order to calculate elastic tunneling of holes into traps. Lundström *et al.* previously showed that the transition rate (Γ) between a semiconductor and a defect in an insulator is given by

$$\Gamma = \tau^{-1} = \left(\frac{m_s}{m_i}\right)^{5/2} \left(\frac{8E_s^{3/2}}{3\hbar\sqrt{E_D}}\right) f\left(E_s\right) T\left(E_s\right) \tag{5.12}$$

where m_s is the effective mass in the semiconductor, m_i is the effective mass in the insulator (a-Si:H(i) in our case), E_s is the energy of the carrier in the semiconductor, E_D is the defect depth, $f(E_s)$ is the Fermi-Dirac probability of an occupied state, and $T(E_s)$ is the transmission coefficient from the energy state in the semiconductor to the defect state in

the insulator. Similarly, the emission rate of a carrier from a defect state to the semiconductor is given by

$$\Gamma = \left(\frac{m_s}{m_i}\right)^{5/2} \left(\frac{8E_s^{3/2}}{3\hbar\sqrt{E_D}}\right)\left[1 - f\left(E_s\right)\right]T\left(E_s\right) \tag{5.13}$$

where $1\text{-}f_s(E)$ is the probability that the energy state E is unoccupied. All other terms retain the same meaning as given in Eq. 5.12.

5.5.3 Inelastic Injection and Emission from traps

The presence of various defect energy levels in the barrier layer provide many options of the final states that are now accessible to the carrier. Carriers can tunnel to these states via a multi-phonon assisted process as shown in Fig. 5.7. Herrmann and Schenk [84] derived a single mode approximation where all the states are coupled to a single phonon mode characterized by an energy $\hbar\omega_0$. The coupling to phonons in the barrier is characterized by an effective phonon energy $n\hbar\omega_0$ (where n is an integer) and two coupling constants (the lattice relaxation energy and the Huang-Rhys factor). Multi-phonon transitions are only allowed for energies that correspond to carrier-phonon coupled states, i.e. $E_m = E + m\hbar\omega$, where m is an integer. Due to the strong scattering present in a-Si:H (as it is an amorphous/defective material), energy is not always conserved. The lack of conservation in energy is accounted for by assuming broadening of the states, which is usually taken to be a Lorentzian distribution in energy. For simplicity, in our simulations we approximate the broadening of the states with a square function with a width of 10 meV centered around the selected energy state E_m.

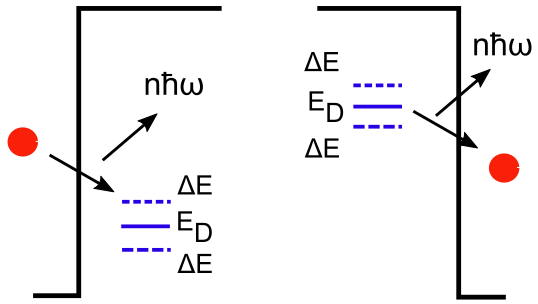

Figure 5.7. Injection and extraction of carriers via multi-phonon tunneling.

The formalism developed by Hermann and Schenk describes the rate of multi-phonon assisted capture by a defect as

$$\Gamma = \tau_m^{-1} = \int_{E_t(x)}^{\infty} N(E) f(E) T(E,x) c_n(E,x) dE \tag{5.14}$$

where $N(E)$ is the 3D density of states in the semiconductor (see Eq. 5.15), $f(E)$ is the occupational probability, $T(E,x)$ is the transmission coefficient from an energy E to the defect state present at a distance x, and c_n is the capture rate given by Eq. 5.16. It is assumed that $N(E)$ implies a 3D density of states with parabolic bands

$$N_{3D}(E) = \frac{1}{2\pi^2}\left(\frac{2m}{\hbar^2}\right)^{\frac{3}{2}} E^{\frac{1}{2}} dE \tag{5.15}$$

$$c_{n(E,x)} = c_0 \sum_{m=0}^{\infty} L_m \delta\left[E - E_m(x)\right] \begin{cases} \exp\left(-\dfrac{E_D - E}{kT}\right), & E_D - E > 0 \\ 1, & \text{otherwise} \end{cases} \tag{5.16}$$

where c_0 is derived from a 3D delta like potential [85] and is given by

$$c_0 = \frac{(4\pi)^2 r_t^3}{\hbar E_g}(\hbar\theta_0)^3 \tag{5.17}$$

where θ_0 is the electro-optical energy in the amorphous silicon barrier (see Eq. 5.18), r_t is the localization radius of the trapped carrier and the E_g is the band gap of the amorphous silicon barrier

$$\hbar\theta_0 = \left(\frac{q^2\hbar^2F^2}{2m}\right)^{\frac{1}{3}} \tag{5.18}$$

where F is the electric field in the barrier.

The multi-phonon transition probability $L_n(z)$ is given by

$$L_n(z) = \left(\frac{f_B+1}{f_B}\right)^{\frac{3}{2}} e^{-S[2f_B+1]} I_n(z) \tag{5.19}$$

where S is the Huang-Rhys factor, $I_n(z)$ is a Bessel function of the order n and $z = 2S\sqrt{f_B(f_B+1)}$, and f_B is the Bose-Einstien distribution function which gives the phonon occupation number. It is important to note that $E_D - E > 0$ corresponds to a scenario where the carriers absorb phonons (gain energy) and is exponentially weighted down as opposed to an emission process. A more detailed explanation of these terms can be found in [65]. Using Eq's 5.14-5.19, we arrive at the total rate of capture by a defect for absorption and emission

$$\begin{aligned}\Gamma_{Capture} &= \sum_{n<0} c_0 N_E(E_n)\,\mathrm{f}(E_n)\,T(E_n,x)L_n(z)e^{\frac{n\hbar\omega}{kT}} \\ &+ \sum_{n>0} c_0 N_E(E_n)\,\mathrm{f}(E_n)\,T(E_n,x)L_n(z)\end{aligned} \tag{5.20}$$

Similar to multi-phonon injection, carriers can also undergo multi-phonon emission from the defects into the extended states of the semiconductor [65]. This transition can be modeled according to

$$\Gamma = \tau_m^{-1} = \int_{E_t(x)}^{\infty} N(E)\left[1 - f(E)\right]T(E,x)e_n(E,x)dE \tag{5.21}$$

where 1-$f(E)$ is the probability that the state is unoccupied and e_n is the emission rate

$$e_n = c_0 \sum_{m=0}^{\infty} L_m \delta\left[E - E_m(x)\right] \begin{cases} \exp\left(-\dfrac{E - E_D}{kT}\right) & , \mathrm{E} - E_D > 0 \\ 1 & , \text{otherwise} \end{cases} \tag{5.22}$$

where all terms have same meaning as Eq. 5.16. The total rate of emission from the defect state to the extended state in the semiconductor is given by

$$\begin{aligned} \Gamma_{Emission} &= \sum_{n<0} c_0 N_E(E_n)[1 - \mathrm{f}(E_n)]T(E_n, x)L_n(z) \\ &+ \sum_{n>0} c_0 N_E(E_n)[1 - \mathrm{f}(E_n)]T(E_n, x)L_n(z)e^{-\frac{n\hbar\omega}{kT}} \end{aligned} \tag{5.23}$$

5.5.4 Defect to Defect

Thus far we have discussed mechanisms that describe charge injection into and charge extraction from a barrier. A core component of transport within an amorphous barrier layer with defects is the 'hopping' of charge between defects. The defect is assumed to have a delta like defect potential whose wavefunction is given by Eq. 5.24.

$$\psi = \sqrt{\frac{r_D}{2\pi}} \frac{e^{-\frac{r}{r_D}}}{r}; r > 0 \tag{5.24}$$

where r_D is the localization radius. The charge transport between defects can be elastic and inelastic (shown in Fig. 5.8). If the initial and final states are at the same energy then the transport will be elastic, whereas, if the initial and final defect are at different energy levels, then the carriers must emit or absorb a phonon in order to make the transition.

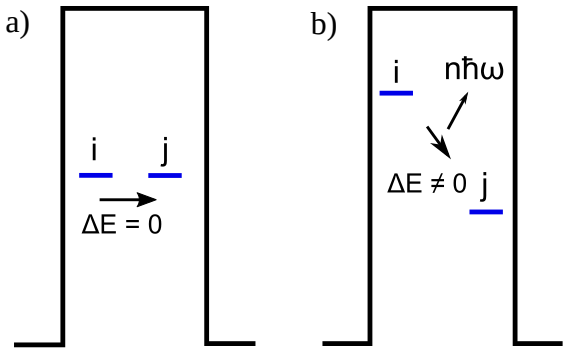

Figure 5.8. a) Elastic defect to defect transition. b) Inelastic defect to defect transition.

The transition rate between defects for elastic and inelastic transitions is given by Miller - Abrams hopping model [86]

$$\Gamma_{ij} = v \times T_{ij} \begin{cases} \exp\left(-\frac{\Delta E}{kT}\right); \Delta E > 0 \\ 1 \qquad\qquad , \text{otherwise} \end{cases} \tag{5.25}$$

where T_{ij} is the transmission coefficient initial defect state 'i' and final defect state 'j', $\Delta E = E_j - E_i$, and v is the lattice vibration frequency ~ 10^{13} Hz, which is a measure of interaction of a carrier with the crystal lattice per second.

5.5.5 Poole Frenkel Emission

Carriers that are trapped in a defect state can be thermally injected into the conduction band under high electric field. It is assumed that the carrier is trapped in a Coulombic potential well. High field conditions can lead to a potential barrier lowering thus increasing

the probability of carrier emission (shown in Fig. 5.9). Frenkel developed a theory to explain the increased conductivity of insulator under a high field [87]

$$\Gamma = \nu \times \exp\left(-\frac{1}{kT}\left(E_D - \sqrt{\frac{e^3 F}{\pi \varepsilon_0 \varepsilon_{opt}}} \right) \right) \tag{5.26}$$

where E_D is the defect depth, F is the electric field, ε_{opt} is the optical permittivity and ν is the lattice vibration frequency. The barrier lowering is given by

$$\Delta E_{PF} = \frac{e^3 F}{\pi \varepsilon_0 \varepsilon_{opt}} \tag{5.27}$$

Equation 5.27 represents a 1D rate, where the carrier is emitted in the direction of the field.

5.6 KMC Algorithm

The kinetic Monte Carlo is used to describe the time evolution of a system. At first the initial state of the system is set up by defining the defect distributions in energy and real space as described by the models in Section 5.2 and 5.3. Using the transition mechanisms defined in Section 5.5, the system can transition from one state to the next. System transitions are defined by two statistical processes, namely, 1) choosing the appropriate transition and 2) the time (Δt) associated with this transition. This process is repeated until enough statistics have been collected in order to analyze system dynamics.

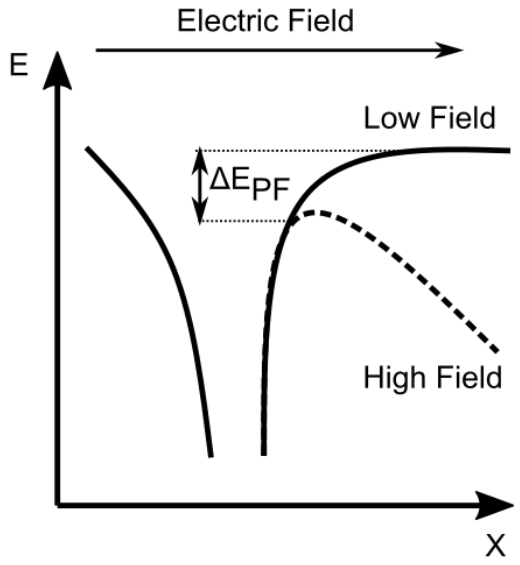

Figure 5.9. Barrier lowering due to high fields in the Poole-Frenkel mechanism.

5.6.1 Transition Table

Thus far the transition rates associated with different mechanisms have been discussed. Here, a single particle KMC algorithm is described which simulates the transition of carriers across the a-Si:H(i)/c-Si heterointerface, through the a-Si:H(i) passivation layer, and finally emission from the a-Si:H(i) passivation layer. At the beginning of the simulation, carriers are initialized at the valence band edge at the a-Si:H(i)/c-Si heterointerface with a Maxwellian energy distribution. For the purposes of injection into the barrier, as described in Section 5.5, multi-phonon and elastic processes are considered. To select the mechanism for injection, a transition table is created which maps the transition rates for all initial carrier energies to all possible final defect states, where transitions into occupied defects are forbidden. Figure 5.10a shows the structure of the transition table

constructed for injection into the a-Si:H(i) passivation layer. The transition rate for each initial energy is a summation over all (n) final possible defects states as shown below

$$\Gamma^{inj}\left(E_i\right)=\sum_{j=1}^{n}\Gamma\left(E_i,E_j\right) \tag{5.28}$$

where E_i is the initial energy, E_j is the final energy, $\Gamma(E_i,E_j)$ is the transition rate from E_i to E_j, and Γ^{inj} is the cumulative transition rate for an energy E_i.

Once the carrier is inside the barrier, it has the possibility of either staying within the barrier (through hopping to another defect state) or exiting the barrier. For simulating these transitions, transition tables are created on the fly, i.e., for a given initial carrier energy, a cumulative transition rate to all possible final states for different transition mechanisms is calculated (shown in Eq. 5.29)

$$\Gamma_k=\sum_{j=1}^{n}\Gamma\left(E_i,E_j\right) \tag{5.29}$$

where $\Gamma(E_i,E_j)$ is the transition rate from initial energy (E_i) to final energy (E_j) and Γ_k is the cumulative transition rate over $'n'$ final states for a given transition mechanism 'k'. Figure 5.10b shows the transition table for the extraction of carriers, where $\Gamma_k(E)$ is the cumulative transition rate for a given initial energy over all final states. Once the transition rate table is created, a transition can be chosen by generating a uniformly distributed random number (r_1) such that

$$\sum_{k=1}^{m-1}\Gamma_k\left(E\right)<r_1\leq\sum_{k=1}^{m}\Gamma_k\left(E\right) \tag{5.30}$$

where m is the total number of transitions available. Once the transition is selected, the time associated with the transition can be calculated by using

$$\tau = -\frac{\ln(r_2)}{\Gamma_{\max}(E)} \tag{5.31}$$

where r_2 is a uniformly generated random number (that is different from r_1), and $\Gamma_{max}(E)$ is the cumulative transition rate for all possible transition mechanism (shown in Eq. 5.32), given by

$$\Gamma_{\max}(E) = \sum_{k=1}^{m} \Gamma_k^{sum}(E_i) \tag{5.32}$$

where Γ_k^{sum} is the cumulative transition rate for an initial energy 'E_i' over all possible final states for a given transition mechanism 'k', and 'Γ_{max}' is the cumulative transition rate over all possible mechanisms for a given energy. A more complete description of the KMC method can be found in [44] and [49].

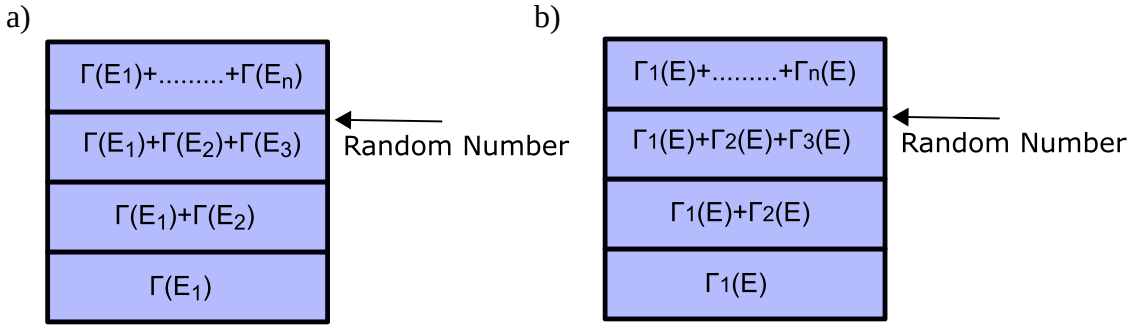

Figure 5.10. Schematic diagram of the transition tables for selecting the final mechanism for (a) multi-phonon injection, and (b) extraction mechanisms which include Poole-Frenkel emission, thermionic emission, direct tunneling and defect emission.

5.6.2 Algorithm

This chapter describes the decoupled use of drift-diffusion and kinetic Monte Carlo simulations to study the transport of photogenerated holes across the a-Si:H(i) passivation layer. The algorithm to conduct the simulations can be described as follows:

1) At first, drift-diffusion simulations are performed over the entire device domain (see Fig 5.1a) to obtain the valence band profile, quasi-Fermi level and electric field for a given device operating point. This information along with parameters describing the band tail and mid-gap defect distributions are used to setup the KMC domain (see Fig. 5.11). The defect distributions in the KMC domain are setup in energy space according to the models described in sections 5.2 and 5.3, whereas the defects are uniformly distributed in real space. To complete the KMC domain, carrier distributions are initialized to mimic equilibrium (see section 5.4.1) or non-equilibrium (see section 5.4.2) situations. An initial carrier distribution can also be obtained from the Monte Carlo solution for the energy distribution function of photogenerated carriers in the high electric field region at the a-Si:H(i)/c-Si heterointerface (described in Chapter 4). Also, the system time is set to zero.
2) Transition rate tables are setup for the injection of carriers into defect states inside the a-Si:H(i) layer. As mentioned previously, once the carrier is in the a-Si:H(i) layer, transition rate tables are created on the fly to simulate transitions within the a-Si:H(i) layer or emission from the a-Si:H(i) layer. Transition tables are created on the fly to save memory.

3) Random numbers from a uniform distribution are used to select a particular transition. Once the transition is selected, a final state is selected, and the system time is incremented.

4) The time taken for each carrier to exit the domain is stored. When all the carriers from the input distribution have exited, an average transit time for the distribution can be calculated. Also, the method of exiting the barrier is stored for analysis.

It should be noted that in this thesis, a single particle KMC has been implemented to simulate transport. While the drift-diffusion model provides the initial condition to setup the KMC domain, the KMC solution is not self-consistently coupled to Poisson's equation. The KMC studies transport across the a-Si:H(i) layer for a given device operating condition assuming that properties, such as electrostatic potential, electric field, quasi-Fermi level, etc., remain constant.

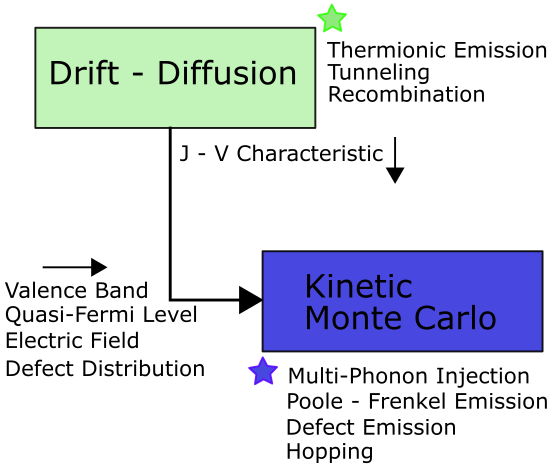

Figure 5.11. Flow of information between the drift-diffusion solver and the KMC solver. Also shown in this figure are the corresponding physical processes incorporated in the theoretical models of the corresponding solvers.

5.7 Results and Discussion

In this section we consider the SHJ solar cell shown in Fig. 5.1a, where drift-diffusion simulations are performed over the entire device domain and the KMC is applied to the a-Si:H(i) layer. At first, we conduct drift-diffusion simulations to obtain the valence band edge, hole quasi-Fermi level and electric field of the device at the maximum power point of the SHJ solar cell.

5.7.1 Variation of a-Si:H(i) Layer Thickness

In this section, two devices are considered, 1) a high fill factor device and 2) a low fill factor device. The high fill factor device has an a-Si:H(p) doping ~ 10^{19} cm^{-3} and the low fill factor has a a-Si:H(p) doping ~ 10^{16} cm^{-3} (both at the front contact). We vary the a-Si:H(i) layer thickness at the front contact from 5 → 30 nm. The n-type c-Si absorber layer is 180 μm and its doping is $N_D = 10^{15}$ cm^{-3}. For the "high fill factor device" we notice a reduction in FF and MPP with increasing a-Si:H(i) thickness. While for the "low fill factor" device, we notice a reduction in FF and MPP, but also observe the S-shape curve in the *J-V* characteristics. Figure 5.12 shows the reduction in MPP for the high and low fill factor device at MPP.

Figure 5.13 shows the average transit time (τ) of the photogenerated holes to cross the a-Si:H(i) barrier as calculated by the KMC. It is assumed that carriers are collected by the Ag contact as soon as they exit the a-Si:H(i) barrier. Also, the results in Fig. 5.13 assume that the carriers at the a-Si:H(i)/c-Si heterointerface have a Maxwellian energy distribution at a lattice temperature of 300 K. As can be in seen in Fig. 5.13, τ increases for both devices as the a-Si:H(i) layer thickness increases. At the first glance, the increase in τ can be

attributed to the fact that a thicker a-Si:H(i) barrier will take a longer time to be traversed by the carriers.

Consider a device with a short circuit current ~ 40 mA/cm^2 and a cross-section ~ 1 μm × 1μm with an inversion layer density ~ 10^{12} cm^{-2}; assuming perfect ohmic transport, the transit time of carriers to reach the metal contact ~ 40 μsec (see Eq. 6.1). The τ calculated by the KMC is the time taken to extract carriers incident on the a-Si:H(i)/c-Si heterointerface to the contact. To obtain perfectly ohmic transport across the a-Si:H(i) layer, the rate of extraction of carriers must be equivalent to the rate of injection of carriers at the a-Si:H(i)/c-Si heterointerface. If the rate of extraction of carriers is slower than the rate of injection of carriers, this implies that the charge is piling up at the a-Si:H(i)/c-Si heterointerface, which is indicative of photocurrent suppression. As described earlier in Section 5.5, the KMC simulates defect assisted transport for holes across the a-Si:H(i) barrier layer. Simulations indicate that photogenerated holes at the a-Si:H(i)/c-Si heterointerface are injected into the a-Si:H(i) barrier through multi-phonon injection [65]. As the thickness of the a-Si:H(i) barrier increases, the valence band gets stretched out, causing the band tail states to be further away from the bottom of the a-Si:H(i)/c-Si heterointerface. Thus, the number of phonons required to inject a carrier into the barrier increases. As the electron-phonon coupling rates are exponentially weighted down by the number of phonons required for absorption transitions, more phonons are required for transitions that take a long time. Finally, increasing the a-Si:H(i) layer thickness causes a reduction in the inversion layer density at the a-Si:H(i)/c-Si heterointerface which also results in a reduction in the electric field (shown in Fig. 5.14).

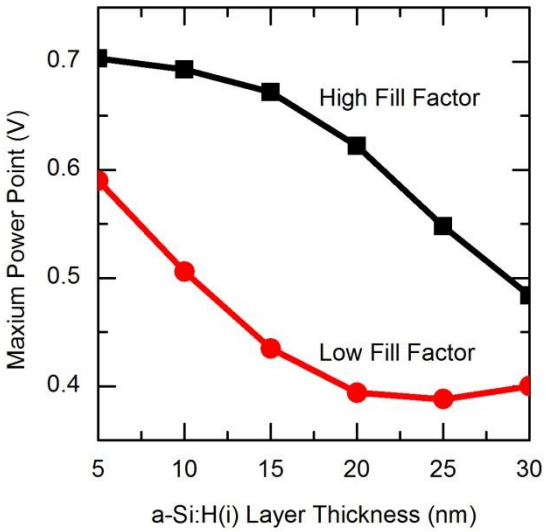

Figure 5.12. Maximum power point vs. a-Si:H(i) layer thickness for a high fill factor and low fill factor device.

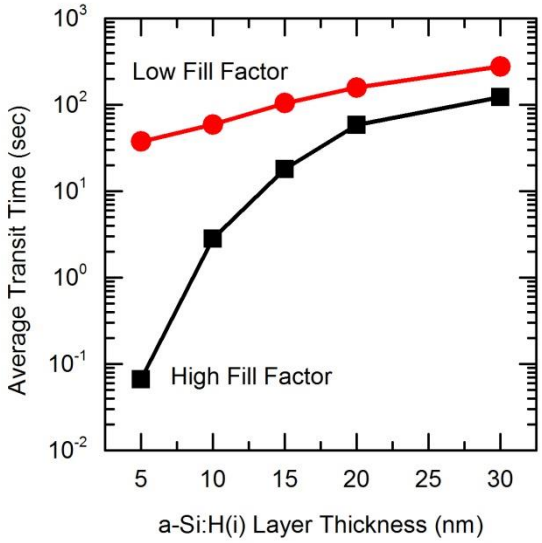

Figure 5.13. Average transit time (τ) for the photogenerated holes to cross the a-Si:H(i) barrier layer vs. a-Si:H(i) layer thickness.

As multi-phonon injection is dependent on the electric field, a weaker field at the heterointerface leads to weaker (longer) multi-phonon transitions. In the case of the low fill factor device, the electric fields at the interface are lower (for a given a-Si:H(i)

thickness) as compared to high fill factor devices. Thus, the average transit time for low fill factor devices is always higher as compared to high fill factor devices. It is also noticeable that, for the high fill factor device, τ increases drastically at first (5 → 20 nm) and then eventually starts (> 20 nm) saturating. There are two reasons for this behavior; first, the electric field decreases sharply at the a-Si:H(i)/c-Si heterointerface for increase in a-Si:H(i) layer thickness (5 → 20 nm) and then gradually begins to saturate (shown in Figure 5.14). The average transit time is inversely proportional to this behavior. Secondly, after a certain thickness a specific phonon transition starts dominating injection transport, which has a characteristic time associated with it.

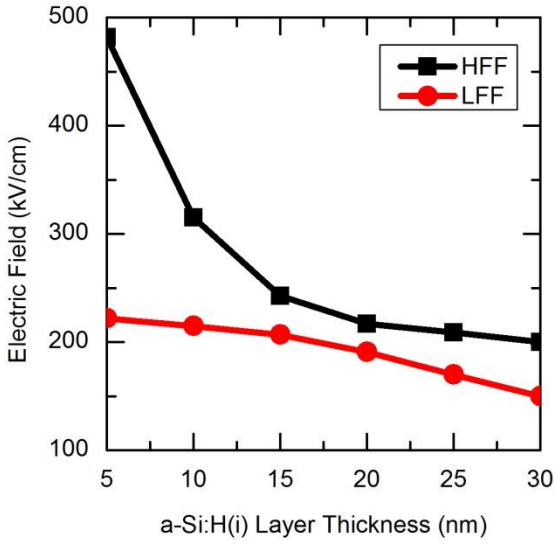

Figure 5.14. Electric field (V/m) at the a-Si:H(i)/c-Si heterointerface vs. a-Si:H(i) layer thickness.

5.7.2 Injection and Extraction Analysis

Figure 5.15 shows the percentage of phonon transitions required to inject holes at the a-Si:H(i)/c-Si interface into the a-Si:H(i) barrier. Simulations indicate that the multi-phonon injection process is the rate limiting step that determines the overall transit time. Hopping within the defects inside the a-Si:H(i) layer and emission of the carriers out of the a-Si:H(i) layer (via Poole-Frenkel and defect emission) are much faster processes.

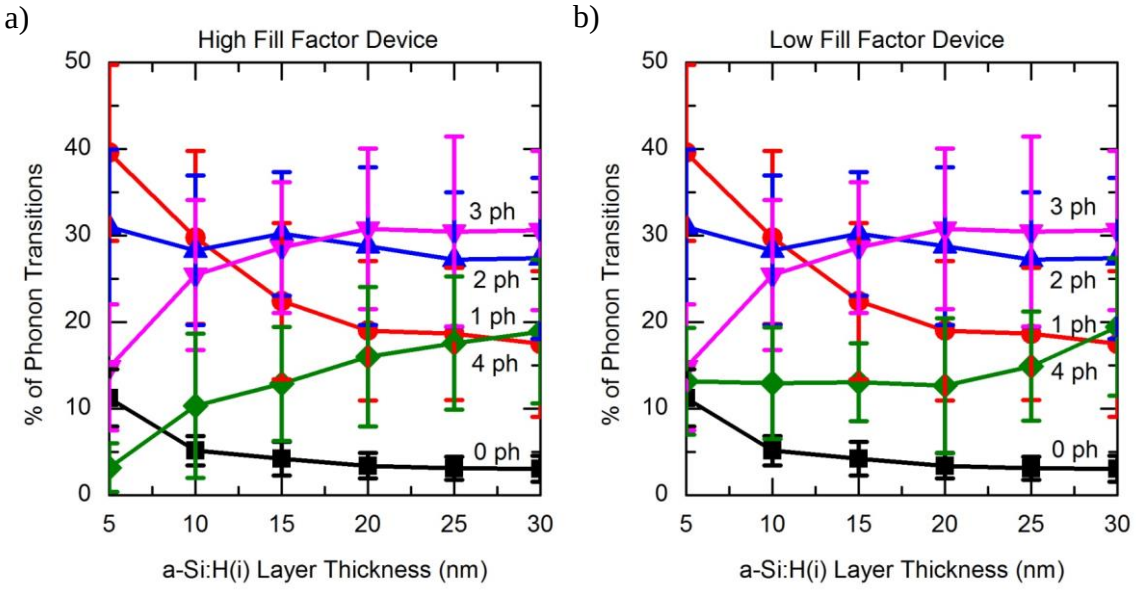

Figure 5.15. Percentage of phonons required for injection into the a-Si:H(i) layer vs. a-Si:H(i) layer thickness for a) high fill factor device and b) low fill factor device.

Figure 5.15 indicates that both devices exhibit very similar phonon dependencies at the heterointerface for both devices, i.e. elastic (0 phonon) processes < 10% and 3 phonon processes dominate after an a-Si:H(i) thickness of 20 nm. However, as the fields at the a-Si:H(i)/c-Si heterointerface are weaker for the low fill factor device as compared to the

high fill factor device, a higher τ is observed. It is important to note that even in the low fill factor device, we still have an inversion layer at the a-Si:H(i)/c-Si heterointerface.

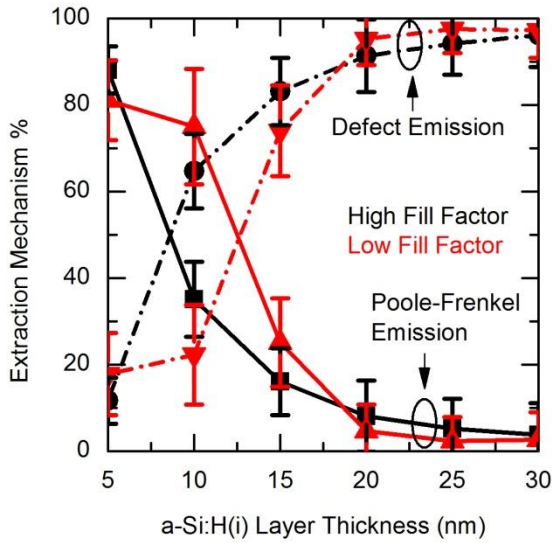

Figure 5.16. Percentage of Poole-Frenkel (solid lines) and multi-phonon defect emission (dashed lines) as extraction mechanisms vs. a-Si:H(i) layer thickness for a high fill factor (black) and low fill factor device (red).

The simulations presented in this chapter consider two extraction mechanisms for the carriers once they are in the a-Si:H(i) barrier, namely, Poole-Frenkel (PF) emission and defect emission. Poole-Frenkel emission is a field assisted emission of a carrier from a defect state into the extended state [69] of a semiconductor, and defect emission is a multi-phonon assisted process similar to multi-phonon injection [65]. Figure 5.16 shows the percentage of extraction for the two mechanisms that are being considered vs. a-Si:H(i) layer thickness. Simulations indicate that for thin a-Si:H(i) layers (<10 nm), Poole-Frenkel emission is the primary extraction mechanism for carriers to exit the barrier. PF emission is a mechanism which is exponentially dependent on the barrier height. It also involves a barrier lowering term which has a strong dependence on electric field. As we have already

established, the peak electric field in the a-Si:H(i) layer is inversely proportional to the thickness of the a-Si:H(i) layer, thus, PF emission is the dominant extraction process for low a-Si:H(i) layer thicknesses. For a-Si:H(i) layers > 10 nm, carriers predominantly exit the barrier via defect emission. It is also evident from Figure 5.16 that for thick a-Si:H(i) barriers (~ 30 nm), Poole-Frenkel emission ~ 0.

5.7.3 Carrier Decay Simulations

Previously, experiments have been conducted to ascertain the transport mechanisms that enable photogenerated holes present at the a-Si:H(i)/c-Si heterointerface to cross the a-Si:H(i) layer and be collected. Crandall *et. al* [15] conducted capacitive decay experiments on SHJ cells and concluded that photogenerated holes hop across the a-Si:H(i) barrier in order to get collected. In the experiment, electron hole pairs were photogenerated at the a-Si:H(i)/c-Si heterointerface via a light flash, and the decay of holes was monitored by measuring the capacitance decay w.r.t time. The simulations recreated the experiment by initializing a hole carrier population at the a-Si:H(i)/c-Si heterointerface and monitored the carrier decay w.r.t time. Simulations indicated that initially the carrier decay slows down with increasing a-Si:H(i) thickness. However, as the a-Si:H(i) layer gets thicker, the rate of carrier decay beings to saturate. Figure 5.17 shows the decay of holes across a a-Si:H(i) barrier vs. time for different a-Si:H(i) layer thicknesses. As can be seen, the carrier decay slows down when the a-Si:H(i) layer thickness is increased from 5 nm (blue) → 25 nm (black). However, the carrier decay is very similar for an a-Si:H(i) layer thickness of 25 nm (black) and 30 nm (green). As discussed earlier, increasing the a-Si:H(i) layer thickness causes the energy bands to get stretched out which results in multi-phonon

injection (of an integer number, $n\hbar\omega$) becoming dominant. Multi-phonon injection limits the overall transit time across the a-Si:H(i) layer and causes the saturation of the transit time. A combination of multi-phonon injection and defect-defect hopping enables the photogenerated holes to get collected. This conclusion agrees well with the conclusions of the experiment conducted in [15], where they observe a saturation in carrier decay and escape time (a parameter extracted from the capacitance measurements) with increasing a-Si:H(i) layer thickness.

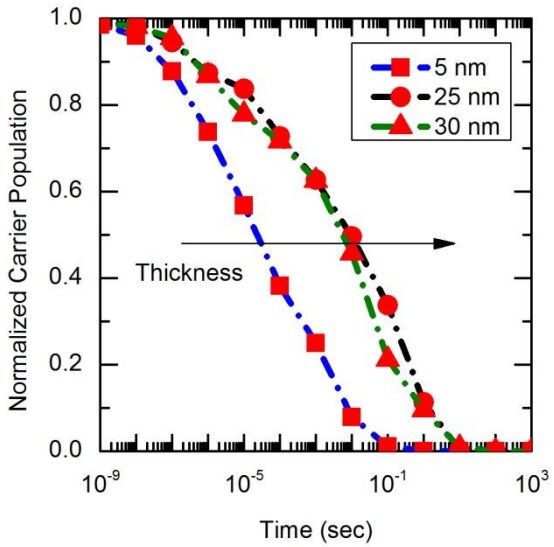

Figure 5.17. Carrier decay of a normalized carrier population of holes at the a-Si:H(i)/c-Si heterointerface for different a-Si:H(i) thicknesses vs. time.

Figure 5.18 shows the carrier decay of holes across the a-Si:H(i) layer vs. time as a function of temperature for a 10nm a-Si:H(i) layer. As discussed previously, multi-phonon injection is the rate limiting process for transport across the a-Si:H(i) layer. The availability of phonons is based on the Bose-Einstein distribution (see Eq. 5.33).

$$f(E) = \frac{1}{e^{\frac{\hbar\omega}{kT}} - 1} \tag{5.33}$$

where $\hbar\omega$ is the phonon energy, k is the Boltzmann constant and T is the temperature. In accordance with Eq. 5.33, the availability of phonons decreases with a decrease in temperature. This leads to an increase in transit time and slower carrier decay with a reduction in temperature.

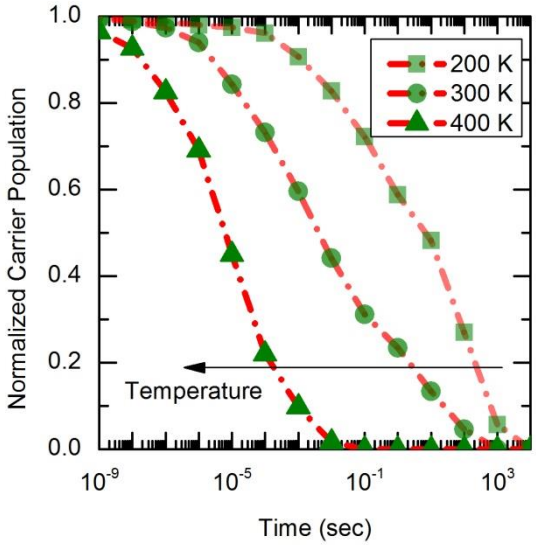

Figure 5.18. Carrier decay of a normalized carrier population of holes at the a-Si:H(i)/c-Si heterointerface various temperatures vs. time.

In Chapter 4, an EMC solver was described that calculated the average energy of the photogenerated carriers at the a-Si:H(i)/c-Si heterointerface under high fields. These simulations indicated that for fields > 100 kV/cm, the carriers exhibit a non-Maxwellian distribution, i.e. average energy > 39 meV. Figure 5.19 shows the average transit time for photogenerated holes to cross the a-Si:H(i) layer vs. average energy of the photogenerated holes at the a-Si:H(i)/c-Si heterointerface. As can be seen, the average transit time

decreases with increasing average carrier energy. Carriers with higher energy can easily access the defect states that are right below the band edge, therefore, transitions into the band tail defect states are going to require lesser number of phonons. As explained in earlier, less phonons correspond to faster transitions.

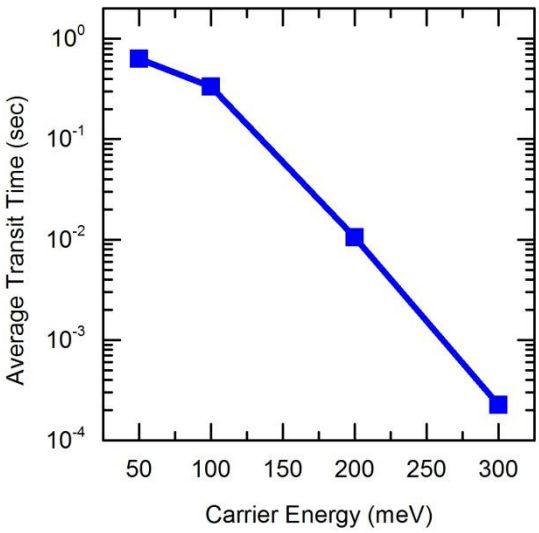

Figure 5.19. Average transit time of photogenerated holes across a 10nm thick a-Si:H(i) layer vs. average carrier energy of photogenerated holes.

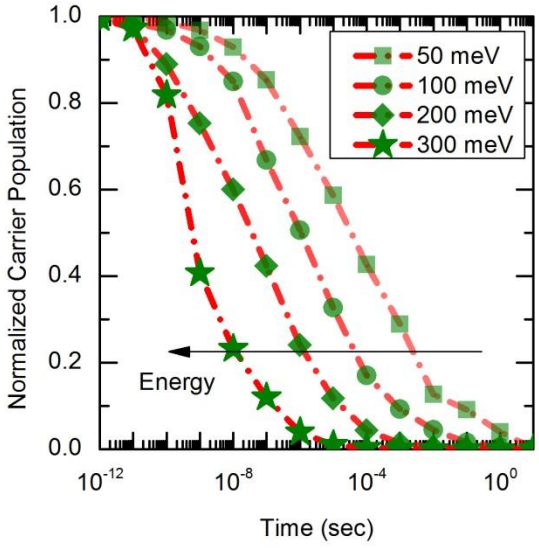

Figure 5.20. Carrier decay of a normalized carrier population of holes at the a-Si:H(i)/c-Si heterointerface for different average carrier energies for photogenerated holes vs. time.

Figure 5.20 shows the decay of photogenerated holes vs. time for carrier distributions with different average energies. It is evident that carrier distributions with higher average energies decays faster. This is due to the fact the rate limiting step of multi-phonon injection is significantly faster for higher carrier energies. As the carrier energy is strongly dependent on the electric field at the a-Si:H(i)/c-Si interface, it can be concluded that passivation at this heterointerface is critical to achieve fast carrier decay.

5.7.4 Effect of the Band Tail Density of States

In this section, a SHJ solar cell (see Fig. 5.1a) with a 10 nm thick a-Si:H(i) passivation layer at the front contact is considered. Drift-diffusion simulations are performed to extract the relevant band profiles at the maximum power point of the SHJ solar cell to set up the KMC domain. Figure 5.21 shows the average transit time (τ) for photogenerated holes at the a-Si:H(i)/c-Si heterointerface to cross the a-Si:H(i) layer as the localized state density of the band tail states is increased. Simulations indicate that holes are injected into the a-Si:H(i) barrier through a multi-phonon injection process, and then move from defect to defect (hopping) before being emitted from the passivation layer.

Primarily, the band tail states assist in the transport of carriers, for both the injection and hopping mechanisms. As mentioned in section 5.2, the localized band tail states are characterized by an exponential decay law (Eq. 5.2). The characteristic decay energy or Urbach energy 'E_{vt}' is determined by the slope of the density of states of defects from experimental measurements, and is an indicator of the band tail state density in the *a*-Si:H(*i*) passivation layer [89]. In Fig. 5.21, the band tail defect density is varied by varying E_{vt} from 20 meV → 80 meV (typically, E_{vt} = 45 meV for device grade *a*-Si:H). Figure 5.21

considers that the holes at the a-Si:H(i)/c-Si heterointerface have a Maxwellian distribution (i.e. average energy ~ 40 meV). It is observed that τ reduces as the defect density in the barrier increases. An increase in defect density in the *a*-Si:H(*i*) barrier results in more low energy defect states being available near the *a*-Si:H(*i*)/*c*-Si heterointerface that carriers can transition into (see Fig. 5.22).

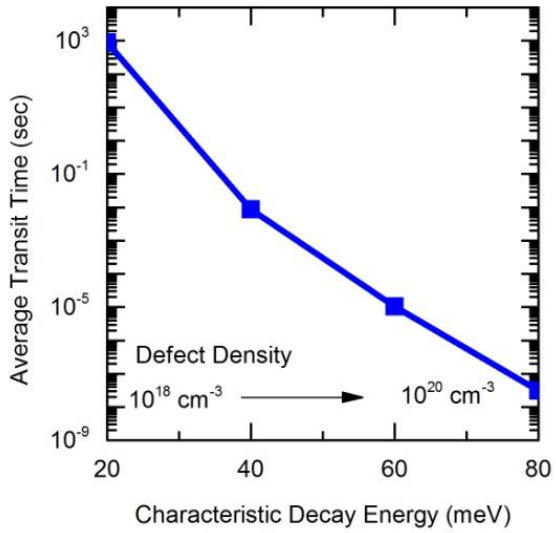

Figure 5.21. Transit time vs. characteristic decay energy (E_{vt}) for a 10 nm *a*-Si:H(*i*) passivation layer.

In Fig. 5.22, the defect-energy space of the a-Si:H(i) barrier for E_{vt} = 20 and 80 meV is shown; where the zero of the energy axis represents the bottom of the valence band at the a-Si/c-Si heterointerface, and the zero of the *x*-axis represents the beginning of the *a*-Si:H(*i*) barrier. Figure 5.22b shows an *a*-Si:H(i) layer with defect density ~ 10^{20} cm^{-3} (E_{vt} = 80 meV). We can observe the presence of low energy defect states implies that fewer phonons are required for injection into the *a*-Si:H(i) passivation layer. Also, the transition time associated with phonon assisted transitions are inversely proportional to the number of

phonons required for the transition (see section 5.5.3). It is also important to note that the defect density in the a-Si:H is strongly correlated with the amount of hydrogenation in the layer, therefore there are some practical limits associated with defect densities that can be achieved in a-Si:H.

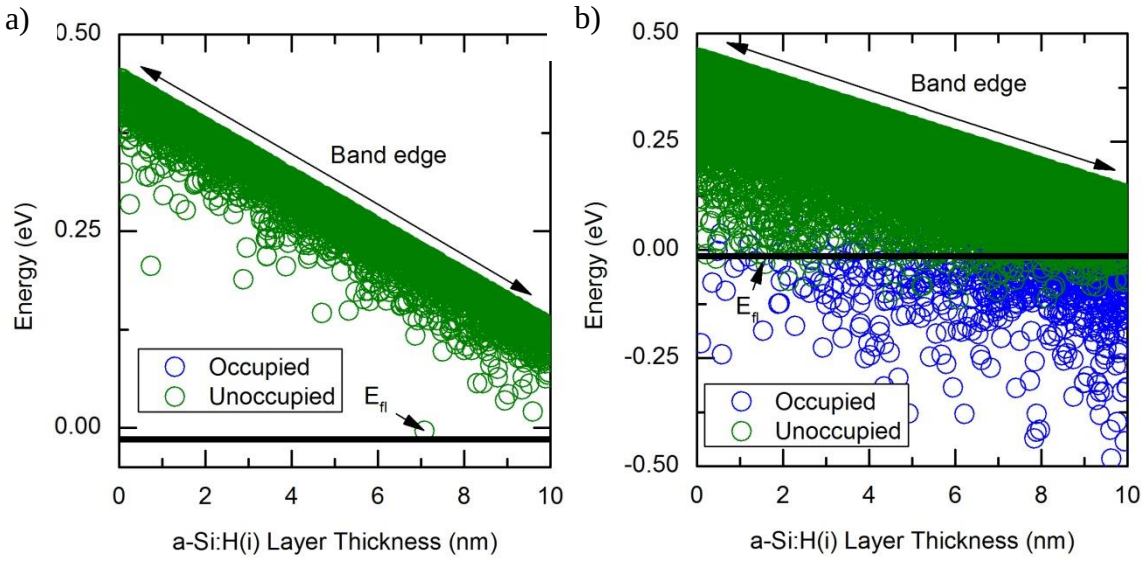

Figure 5.22. Defect energy space in the *a*-Si:H(*i*) passivation layer for an E_{vt} of a) 20 meV and b) 80 meV.

5.7.5 Effect of the Optical Phonon Energy

Drift-diffusion simulations were conducted for a SHJ solar cell with a 10 nm a-Si:H(i) passivation layer at the front contact to extract the relevant band profiles at maximum power point to set up the KMC domain. Figure 5.23 shows the average transit time (τ) taken by photogenerated holes present at the a-Si:H(i)/c-Si heterointerface to cross the a-Si:H(i) passivation layer for different optical phonon energies in the a-Si:H(i). It is observed that the transit time reduces with an increase in optical phonon energy.

The phonons are distributed in accordance with the Bose-Einstein distribution (shown in Eq. 5.33). A higher phonon energy means a lower population of optical phonons at a given temperature. However, the a-Si:H(i) passivation layer forms a triangular barrier. Also, the band tail state density exponentially decays from the *a*-Si:H(*i*) valence band edge, and the photogenerated holes are placed energetically at the valence band edge at the a-Si:H(i)/c-Si heterointerface (see Fig. 5.22) with a Maxwellian distribution; a higher phonon energy would imply that fewer phonons are required to inject carriers into the a-Si:H(i) passivation layer. Also, it is important to note that the optical phonon energy for a-Si:H ~ 60 meV.

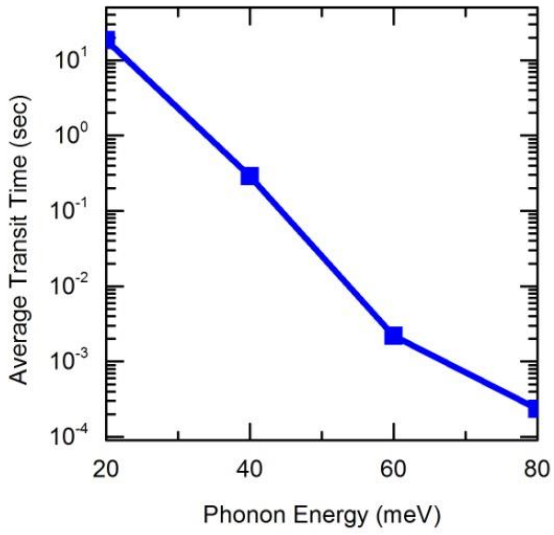

Figure 5.23. Transit time vs. optical phonon energy for a 10 nm *a*-Si:H(*i*) passivation layer.

Figure 5.24 shows the path taken by a few selected carriers across the a-Si:H(i) passivation layer. For Fig. 5.24, a 10 nm thick a-Si:H(i) passivation layer was considered with a carrier distribution with average energy ~ 150 meV and E_{vt} = 45 meV. In Fig. 5.24,

we see that the carriers initially gain energy by absorbing phonons to get to the defect states near the valence band edge and proceed to cascade down the band edge and eventually get collected. However, simulations indicated that the path taken by carriers to cross the a-Si:H(i) barrier layer depends heavily on the properties of the barrier. For layers with low thickness (< 10 nm) and low defect densities, it is more likely that the carriers will undergo single step hopping; i.e. the carriers at the a-Si:H(i)/c-Si heterointerface will undergo a multi-phonon injection mechanism to enter a defect state in the a-Si:H(i) passivation layer, and then exit the a-Si:H(i) via Poole-Frenkel or defect emission. Conversely, for layers with higher thickness (>15 nm) and higher defect densities, the carriers will hop multiple times within the barrier before exiting. In both cases, the total time taken to cross the barrier is strongly controlled by the time taken by the multi-phonon injection transition.

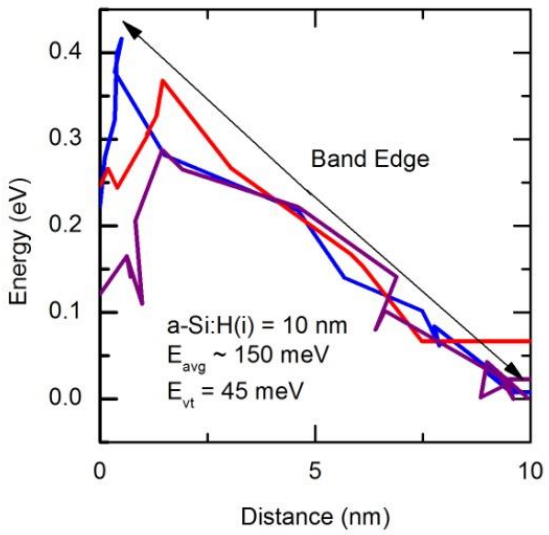

Figure 5.24. Tracking carriers through a 10 nm a-Si:H(i) passivation layer.

5.7.6 Effect of Mid-Gap States and Interface Recombination

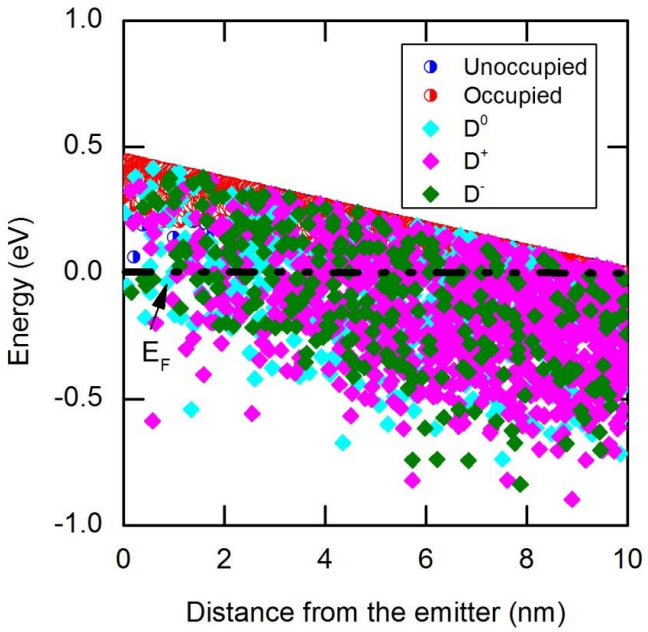

Figure 5.25. The kMC domain (i-aSi) with localized and mid gap states.

A qualitative study was conducted to understand the effect of interface states and midgap states on transport. The interface states were defined as a Gaussian with two peaks and the midgap states were defined according to the defect-pool model. Figure 5.25 shows the KMC domain with the presence of localized and midgap states. Simulations indicated that carrier distributions with low average energies are limited by interface recombination. As mentioned in previous sections, transport across the barrier is strongly controlled by the multi-phonon injection into the a-Si:H(i) layer. In other words, the slowest process is the carrier going from the inverted heterointerface into a defect state in the a-Si:H(i). Therefore, the interface recombination rate can compete with the transport mechanism. However, once the carrier is 'hopping' through the localized defect states, the hopping rates

are much faster than the midgap recombination rates. A poorly passivated device can be driven out inversion due to interface recombination; which will greatly reduce the surface potential at the heterointerface [90].

5.7 Conclusion

The kinetic Monte Carlo is a tool that can go beyond time scale constraints that limits the application of ensemble Monte Carlo techniques to study defect related processes. Defect assisted transport is characterized by defect capture and emission times; these processes can range anywhere from picoseconds to microseconds. The EMC however is limited by scattering times of the carriers which are femtosecond processes. However, there are weighted Monte Carlo techniques [91] which can deal with recombination processes, but it is still immensely complicated to add defect interactions.

In this chapter, a kinetic Monte Carlo methodology is presented that is applied to study transport of photogenerated holes through the a-Si:H(i) passivation layer in a SHJ solar cell. Drift-diffusion simulations are performed to obtain the valence band profile, quasi-Fermi level and electric field in the a-Si:H(i) passivation layer at any given voltage. The results from the drift-diffusion simulations are then used to setup the KMC domain. To model transport through the a-Si:H(i) passivation layer, multi-phonon injection, defect to defect transitions (hopping), multi-phonon defect emission, thermionic emission and Poole-Frenkel emission are considered. Since, the drift-diffusion simulations provide a snapshot of the band profiles, the KMC method is used to correlate transport through the a-Si:H(i) layer for a given device operating condition. Simulations indicate that transport through the a-Si:H(i) passivation layer is strongly dependent on the properties of the a-Si:H

and, the average transit time across the barriers is strongly controlled by multi-phonon injection into the barrier.

The simulations specifically analyzed the effect of various parameters related to the a-Si:H(i) layer and the a-Si:H(i)/c-Si heterointerface on transport of carriers. In the case of the band-tail state density in the a-Si:H(i) layer, simulations showed that an increase in defect density in the a-Si:H(i) passivation layer reduced the number of phonons required to inject a carrier from the a-Si:H(i)/c-Si heterointerface into the a-Si:H(i) passivation layer, resulting in faster transit times. However, varying the defect density in the a-Si:H(i) is achieved by changing the amount of hydrogenation which results in changes of some other material parameters (bandgap etc.) which may not be ideal for the purposes of solar cells. Simulations also indicated that for thin a-Si:H passivation layers and low defect densities, the carriers crossed the passivation layer through single step hopping, whereas for thicker barriers and high defect densities the carriers underwent multi-step hopping to get across the barrier. In both cases, the transit time to cross the barriers was limited by the multi-phonon injection into the barrier. Simulations indicated that for extraction from the a-Si:H(i) layer, Poole-Frenkel emission was the main mode of extraction for thin a-Si:H(i) layers (< 10 nm), whereas defect emission was dominant for a-Si:H(i) layers > 10 nm.

The simulations presented in this chapter conclude that the high electric field at the a-Si:H(i)/c-Si heterointerface is essential for efficient transport of holes across the a-Si:H(i) layer. High electric fields can only be achieved by optimizing the various layers of the heterojunction contact stack. In particular, the a-Si:H(p) layer doping and thickness, the a-Si:H(i) layer thickness, and passivation at the a-Si:H(i)/c-Si layer heterointerface.

Simulations show that increasing the a-Si:H(i) layer thickness results in a reduction of electric fields at the a-Si:H(i)/c-Si heterointerface and subsequently an increase in transit time to cross the a-Si:H(i) layer. Longer transit times are indicative of photocurrent suppression at the a-Si:H(i)/c-Si heterointerface, which can lead to S-shape like behavior in the J-V characteristics and overall degradation of device performance (especially FF) in SHJ solar cells. Also, the carrier decay simulations presented in this chapter were consistent with experimental findings that the carrier decay across the a-Si:H(i) layer saturates with increasing a-Si:H(i) layer thickness.

The KMC simulations presented in this chapter analyze transport for a given device operating condition that is calculated by the drift-diffusion model. These simulations are performed in a de-coupled manner where the KMC results are not fed back into the drift-diffusion simulation. In other words, the KMC solution is not self-consistently coupled with the Poisson's solution. To gain further understanding of the effect of non-equilibrium transport through defects, the KMC can be coupled to the drift-diffusion solution. However, this is a non-trivial task as the KMC will be a sub-domain within the drift-diffusion domain. This introduces many complications in terms of establishing charge and current continuity at the boundaries.

CHAPTER 6

MULTISCALE MODELING

Modern solar cell devices (2^{nd}, 3^{rd} generation and beyond) [92] employ the use of novel heterojunctions, quantum well structures, tandem structures, and utilize new materials which propels the underlying transport physics out of the traditional semi-classical regime. This necessitates the use of atomistic and first principle approaches [93] while trying to understand the properties of new materials or quantum phenomena that occur in novel nanostructured devices. Methods such as non-equilibrium Green's functions (NEGF) [94] and full band Monte Carlo [95] are often utilized to study quantum transport in nanostructured devices; however such approaches are computationally very expensive. Most solar cells (even thin film solar cells) are macroscopic devices (microns) where non-local transport occurs in only a very small region of the device. Therefore, applying full particle-based transport approach to the entire device domain can be very computationally costly. On the other hand, continuum models such as drift-diffusion are very effective in studying semi-classical transport in macroscopic devices. However, as described in Chapter 2, the drift-diffusion model is derived from the BTE after making several assumptions (see Fig. 6.1). Analytical and continuum models eventually breakdown while dealing with non-local phenomena as the basic assumptions inherent to these models are violated.

Another issue while considering a wholistic approach to describe transport in a device is that low field semi-classical behavior and nano-scale quantum behavior occur at vastly different time scales and length scales. An effective method of solving the transport

problem would be to couple different methodologies which resolve varying time and length scales to form a *multiscale* solution to a multiscale problem. However, formulating a multiscale solution is a non-trivial problem, as resolving different mathematical models is quite challenging [85,86]. In a multiscale formulation, the focus is on unifying models self-consistently to facilitate a comprehensive and quantitative analysis of the problem. Figure 6.2 shows the three different solvers that have been developed in this thesis, namely drift-diffusion (Chapter 2), ensemble Monte Carlo (Chapter 4) and kinetic Monte Carlo (Chapter 5), and their interaction over varying time and length scales.

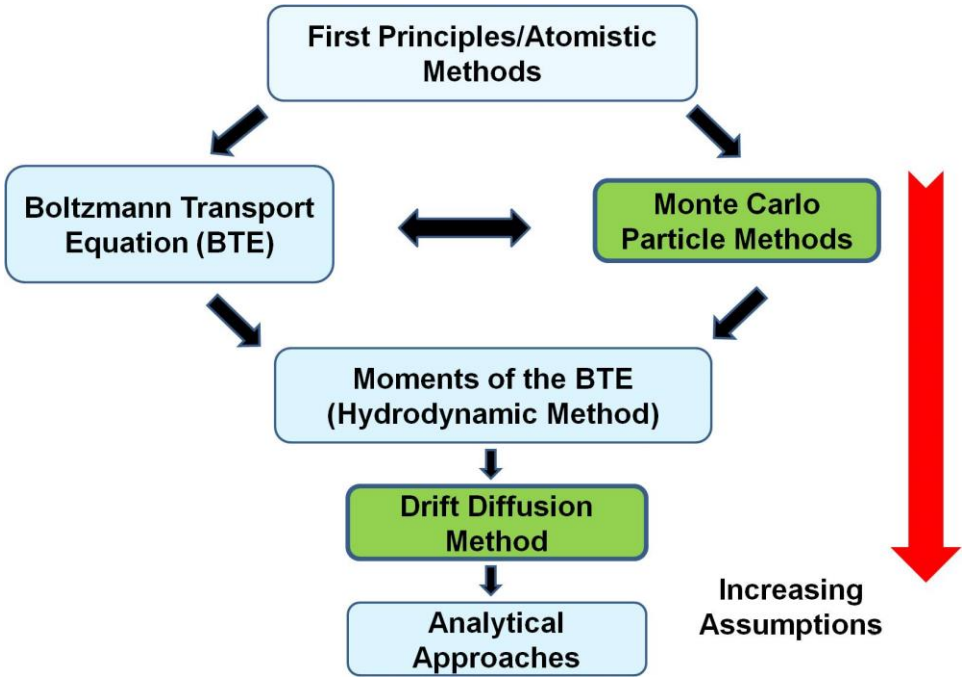

Figure 6.1. Schematic diagram of the hierarchy of simulation models. The boxes shaded in green (Monte Carlo and Drift-Diffusion) are coupled to form a relatively accurate and computationally efficient solution to a high field transport problem.

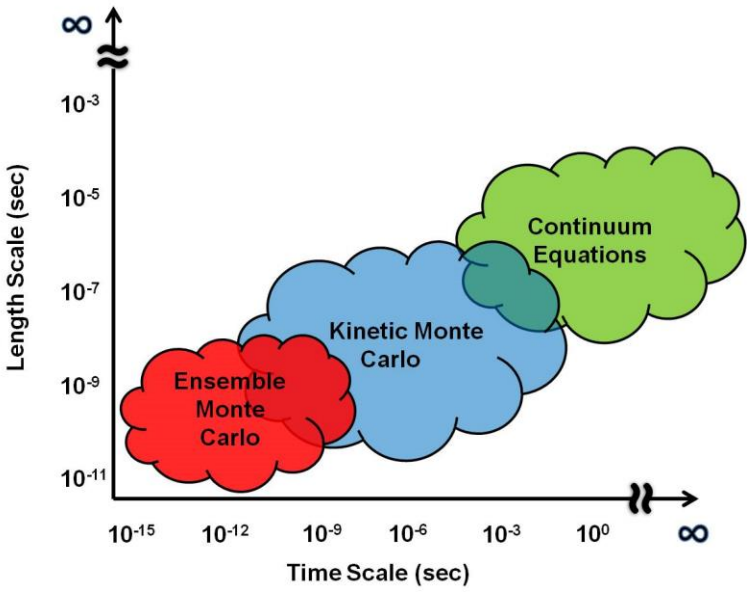

Figure 6.2. Visualization of the interaction of the three solvers in a multiscale framework.

Recently, the multiscale methodology has been applied to address various issues in solar cells such as mechanical properties of materials [98], optical properties [99] and interface phenomena [100]. Using the principle of coupling macroscopic and microscopic models, the multiscale methodology has been used to study the effect of complex interface morphologies and bulk mechanisms in organic solar cells [101]. In this thesis we utilize the multiscale methodology to study transport in SHJ solar cells. In particular, the drift-diffusion model operates in the low field region of the device, the EMC operates in the high field c-Si region adjacent to the a-Si:H(i)/c-Si heterointerface, and the KMC operates solely in the a-Si:H(i) layer. Each individual module was used to study a specific aspect of the multiscale problem in a decoupled manner. In this chapter the process and various challenges of self consistently coupling the drift-diffusion and EMC solvers are described.

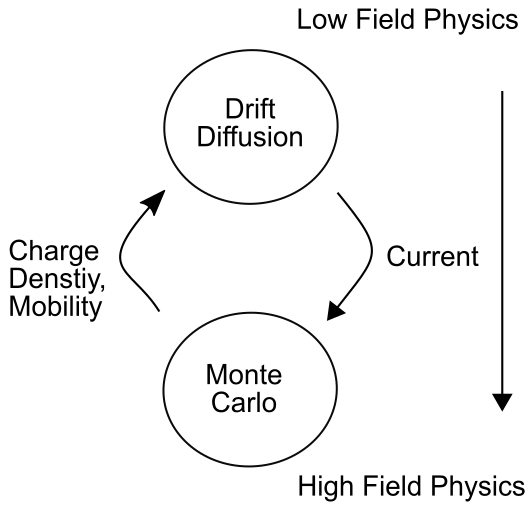

Figure 6.3. Schematic diagram describing the coupling of the drift-diffusion and EMC solver.

6.1 Drift-Diffusion Coupled with a Monte Carlo

In a simple drift-diffusion model, the carrier density and mobility are treated as local functions of the electric field. This assumption is valid and relatively accurate when the electric field is weak and slowly varying. However, in the cases of large and quickly varying electric fields, this assumption is no longer valid. In the high electric field case, the energy distribution function of the carriers can no longer be defined as a local function of the electric field. An EMC solution can be quite inefficient in low field regions, as the carriers can remain virtually stagnant due to the weak driving force. Therefore, a coupled solution where the drift-diffusion model operates in the low field region and the EMC operates in the high field region offers an ideal compromise between accuracy and computational efficiency (see Fig. 6.3). This technique has previously been used to study

hot carrier effects in MOSFET's [95,96]. As described in Chapter 4, the EMC is an ideal tool to study carrier distributions under high electric fields, and therefore it was used to study the behavior of photogenerated carriers under high fields at the a-Si:H(i)/c-Si heterointerface. A crucial point to note here is that EMC solution captures the non-local effects of high fields on the carrier distribution which will differ from predictions of the drift-diffusion model. To consider these non-local effects, there must be some self-consistency between the two solvers. Self-consistency for a coupled drift-diffusion and EMC solver has been addressed previously by Kosina *et al.* [104] for MOSFET devices. The goal of this research work is achieving self-consistency for a bipolar device, i.e. a solar cell.

The subsequent sections of this chapter describe the considerations required to couple an EMC to a drift-diffusion model self consistently (DDEMC). Sections 6.1.1 - 6.1.9 describe the process of setting up the Monte Carlo region once the drift-diffusion model has computed the initial solution.

6.1.1 Injection Boundary

Figure 6.4 shows a SHJ device along with the various simulation domains. The drift-diffusion model calculates the initial solution throughout the entire domain. The primary aim of the EMC is to study the effect of high electric fields at the a-Si:H(i)/c-Si heterointerface on photogenerated holes in the device. The injection boundary of the EMC is placed in a quasi-neutral low field region in the c-Si where the energy distribution function of the holes can be approximated by a Maxwellian distribution. For Si devices the injection boundary can be placed in regions with fields greater than 10 kV/cm. The

sensitivity to the injection boundary is low as the saturation velocity in Si is quite high. Also, placing the injection boundary in regions with electric field ≈ 0 kV/cm can significantly slow down the simulation as the carriers remain virtually stagnant in the absence of a strong driving force, and this can considerably increase the size of the EMC domain. It is important to note that the simulation presented in this chapter do not consider the TCO layer and silver contact. Also, only the coupling between the EMC and drift-diffusion solver is described.

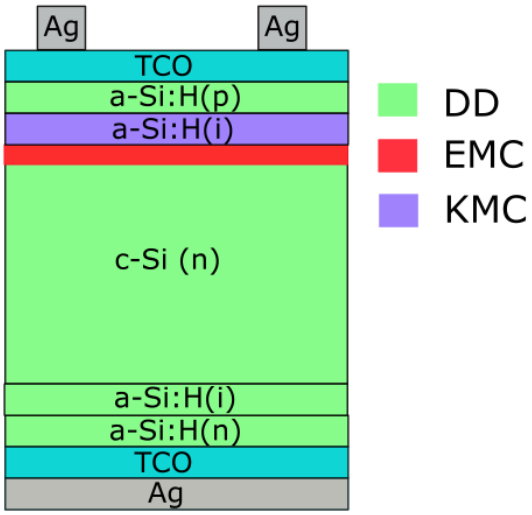

Figure 6.4. Visualization of the simulation domains in SHJ solar cell. The EMC domain that operates at the heterointerface (red) must be coupled to the drift-diffusion domain in the low field regions (green).

6.1.2 Current Injection Boundary Conditions

Once the EMC window is placed within the device, boundary conditions are required to ensure continuity between the two solvers. These boundary conditions must ensure current continuity and charge conservation. At the current injection boundary, the current

calculated by the drift-diffusion model is injected into the EMC domain. The current from the drift-diffusion model is calculated in A/cm^2. The current is defined as the charge per unit time (Eq. 6.1)

$$J = \frac{nq}{\Delta\tau A} \tag{6.1}$$

where n is an integer number of particles, q is the fundamental charge, $\Delta\tau$ is the observation time (0.2 fs) used for the EMC, and A is the cross-sectional area of the device. Using Eq. 6.1, the drift-diffusion current is interpreted as a number of particles that will be injected into the EMC region per unit time.

Currents in single junction solar cells are to order of mA/cm^2. This usually results in $n < 1$. Therefore, to inject particles, a strategy involving random numbers is used. For every $\Delta\tau$, a random number r [0,1] is generated from a uniform distribution. If $r < n$; 1 particle is injected, if $r > n$; 0 particles are injected. Using this scheme, the current J can be injected over a total time τ.

As mentioned before the injecting boundary is placed in a low field region. However, the non-zero fields will cause the velocity distribution of the carriers to be slightly 'drifted'. Thus the injected carriers must have a displaced Maxwellian velocity distribution [105] which is used to generate a 'drifted' wave vector distribution in direction of the field. Calculating velocity for a warped bandstructure can lead to implicit equations due the angular dependence of effective masses. To simplify the velocity calculations, we assume a parabolic bandstructure (Eq. 6.2) to create the 'drifted' velocity distribution.

$$E = \frac{\hbar^2 k^2}{2m^*} \tag{6.2}$$

where k is the wave vector in direction of the field, and m^* is the effective mass of the carrier. Thus, the velocity can now be given by

$$v = \frac{1}{\hbar}\frac{\partial E}{\partial k} = \frac{\hbar k_x}{m} \tag{6.3}$$

To create a drifted distribution, a Maxwellian distribution centered around the drift velocity is assumed. Equation 6.4 is used to create the 'drifted' velocity distribution

$$f(v) = v \times \exp\left(-m^* \times \frac{(v - v_d)^2}{2kT} \right) \tag{6.4}$$

where v is the Maxwellian distribution of the velocity, and v_d is the value of average velocity extracted from the drift-diffusion current. The current can be related to average drift velocity by

$$J = q\, n\, v_d \tag{6.5}$$

where J is the current density, n is the carrier density, and v_d is the average drift velocity. The 'drifted' wave vector (in the direction of the electric field) can be calculated by using the 'drifted' velocity (for parabolic bands)

$$k_{x,drift} = \frac{m v_{drift}}{\hbar} \tag{6.6}$$

An important point to note is that at the injection boundary, carriers are assumed to only be injected. A reflective boundary condition is applied so that carriers cannot leave the domain; they are elastically reflected back into the domain. The carriers are extracted at the collecting boundary as shown in Fig. 6.5. The drift-diffusion solver and the EMC solver are said to be current matched when the extracted current = injected current. Thus, current continuity between the two models is ensured.

6.1.3 Half Maxwellian Charge Injection

Charge at the injection/extraction boundaries must be injected with half-Maxwellian distributions perpendicular to the boundary. If the injected charge is not injected in the direction of the electric field, it can lead to spurious accumulation or depletion of charge in the simulation domain. As the EMC is coupled to a Poisson solver, this can lead to instability in the electrostatic potential in the device. Also, as the EMC solution feeds back into the drift-diffusion model, it is imperative that the charge density from the EMC solution is correct and not discontinuous.

6.1.4 Extraction Boundary (placed at the contact)

According to Fig. 6.4 the extraction boundary of the EMC domain is placed at the a-Si:H(i)/c-Si boundary. To simplify the problem, let us assume that the extraction boundary for the EMC region is placed at the contact; charge neutrality conditions can be enforced on the contact cell. In other words, at every Δt carriers will be injected back into the contact cell to maintain charge neutrality. The amount of charge to be maintained at the contact cell is given by doping under the contact. Figure 6.5 shows the visualization of the EMC domain with the boundary conditions.

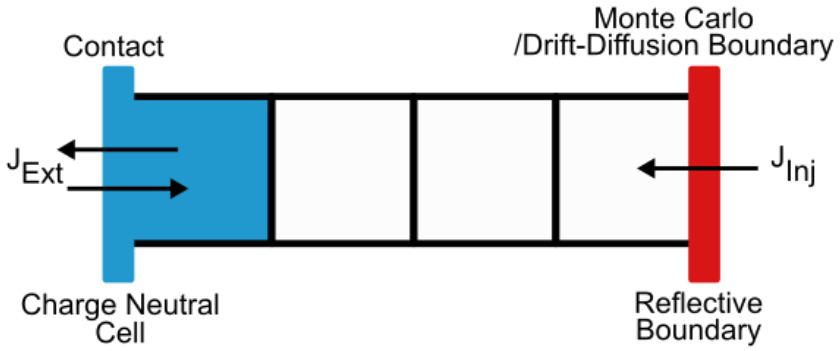

Figure 6.5. Visualization of the MC domain.

6.1.5 Extraction Boundary (placed away from the contact)

As shown in Fig. 6.4 the EMC domain ends at the a-Si:H(i)/c-Si heterointerface. However, matters are complicated when the EMC domain extraction boundary is placed away from a contact (see Fig 6.6) as charge neutrality conditions are no longer valid. To ensure charge continuity across the boundary, we implement a 'fixed charge density' boundary condition. The charge density of the extraction boundary cell is determined by the drift-diffusion solution. Carriers are injected to maintain a constant charge density in the collecting boundary cell. The injected carriers must have a 'drifted' velocity distribution in order to capture the high field effects. The nature of the collecting boundary is characterized by a velocity distribution function. Previously, Nguyen et al. have implemented boundary conditions for a collecting boundary by using a 'Back Diffusion Ratio' [106].

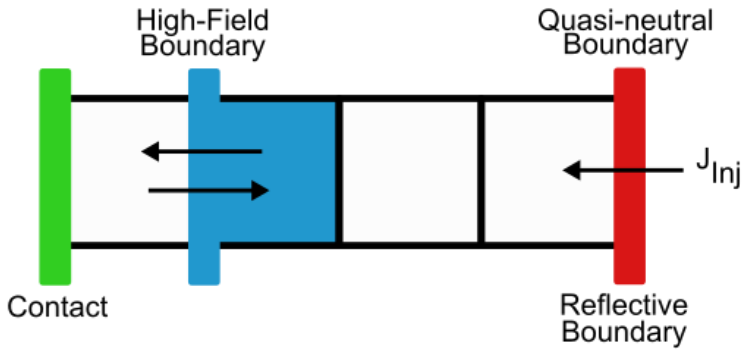

Figure 6.6. Visualization of MC domain where the collecting boundary is placed away from the contact

6.1.6 Current Matching

The EMC solver converts the charge density and fluxes obtained from the drift-diffusion solver into discrete particles. To ensure charge and current continuity across the virtual boundaries, injection and extraction boundary conditions are implemented. The EMC solver is run until it is current matched to the drift-diffusion solver, i.e. the extracted current = injected current. Assuming that there is no recombination in the EMC domain, the solver should be current matched after a few picoseconds. Once the EMC solution is current matched to the drift-diffusion solution, it is an indication that the EMC solver has reached steady state, and thus the charge density is in steady state. At this point the charge distribution in the EMC (represented by discrete particles) is coupled back to the mesh using particle mesh coupling (PMC). There are several schemes to perform PMC such as nearest element center (NEC), nearest grid point (NGP), cloud-in-cell CIC etc. [107]. In this work, the CIC method has been implemented. Figure 6.7 shows all the steps required to current match the MC solver to the drift-diffusion solver.

6.1.7 Robin Boundary Conditions (RBC's)

The EMC solution calculates the correct hole charge distribution under high electric fields. To preserve the physics of the EMC solution, the DD solution no longer operates in the EMC region. For this purpose, the charge density in the EMC domain is frozen, and the continuity equations are then solved only outside the EMC domain (discussed further in Section 6.1.8). As the flux between the DD and EMC regions must remain continuous, a flux boundary condition is implemented at the DDMC boundaries while solving the

continuity equations. This boundary condition is known as a Robin boundary condition whose general form is given by

$$\alpha u + \beta \frac{du}{dx} = \Gamma \tag{6.7}$$

where α and β are constants, u is a function, du/dx is its spatial derivative and Γ is another function. In the case of the DD model, the Robin boundary condition takes the form of the current equations

$$q\mu pE - qD_p \frac{dp}{dx} = J_p \tag{6.8}$$

The discretized form of Eq. 6.8 is given by Eq. 6.9

$$\frac{qD_{pi+1/2}}{\Delta}\left[p_i B\left(\varphi_{i+1} - \varphi_i\right) - p_{i+1} B\left(\varphi_i - \varphi_{i+1}\right)\right] = J_{pi+1/2} \tag{6.9}$$

where '*i*' is the node point and B is the Bernoulli function.

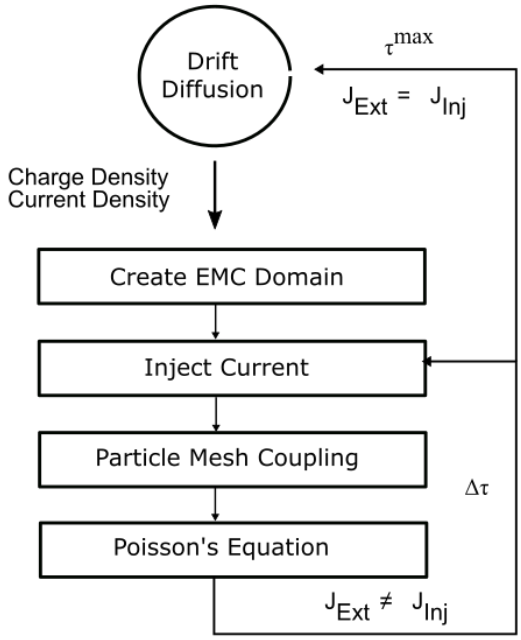

Figure 6.7. Flowchart describing how to current match a MC solver to a drift-diffusion solver.

6.1.8 Gummel Loop

Self-consistent coupling requires that properties calculated by the EMC are utilized by the drift-diffusion solver. At first, the drift-diffusion solution is applied to the entire domain. The charge density calculated by the drift-diffusion solver is used as an initial condition for initializing carriers in the EMC domain, and the current calculated by the drift-diffusion is used as an injection boundary condition (B_2). Once the EMC has reached steady state, the continuity equations are used to recalculate the charge density using RBC's. Finally, Poisson's equation is used to calculate the potential all over the device. Figure 6.8 shows how the entire device domain is divided into various regions where the continuity and the EMC solutions are applied; C_1 and C_2 are the contacts of the device (Dirichlet boundaries), and B_1 and B_2 are the boundaries of the EMC domain.

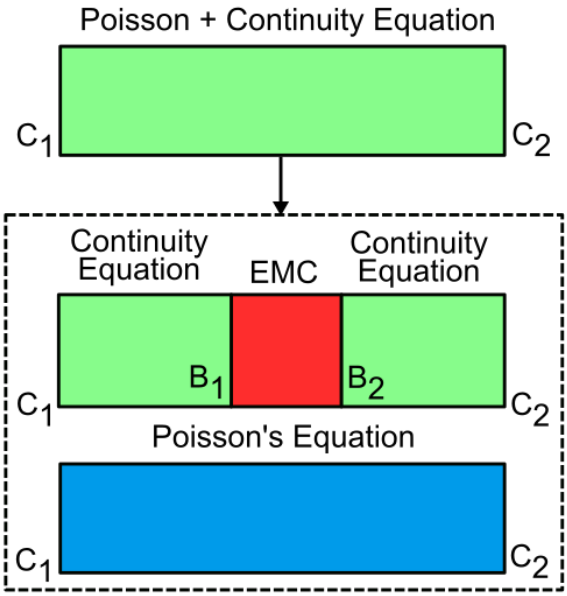

Figure 6.8. Visualization of the coupled DDMC solution, where the continuity equation solves (green) for charge density outside the EMC domain (red) and Poisson's equation is solved over the entire device domain. C_1 and C_2 are the contacts of the device, and B_1 and B_2 are the shared boundaries of the drift-diffusion and EMC domains.

Figure 6.9 shows a flow chart of the process flow of the Gummel loop. The drift-diffusion solution provides all the initial conditions in terms of charge density, potentials, electric fields and current density. These parameters set up the initial conditions for the EMC. The EMC solution coupled with the Poisson solution runs until it is current matched with the drift-diffusion solver, and steady state conditions for the hole density are reached; then the program flow returns to the drift diffusion domains. It is important to note that there are two drift-diffusion domains in the device which operate on either side of the EMC domain (see Fig. 6.8). Once the program flow exits the EMC domain, the continuity equations for holes are solved outside the EMC domain, while the charge in the EMC domain remains frozen. The electron charge density is computed by solving the continuity equations over the entire domain; finally, Poisson's equation is solved over the entire domain.

As the EMC is coupled to a Poisson solver, the fields are recalculated for each time step. Once steady state is reached, the EMC recalibrates the mobilities for the high field and low field regions which are used to calculate the current. The coupling of the drift-diffusion to the EMC leads to new currents which can be used as injection conditions for the EMC. Now, the EMC and the drift-diffusion must be current matched for the new injection condition. Once the injection condition stabilizes, the EMC and drift-diffusion solvers have been self-consistently coupled.

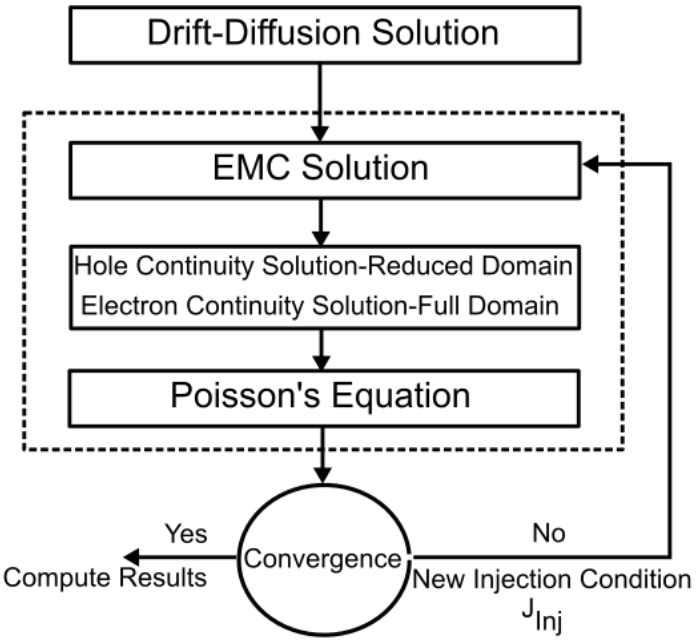

Figure 6.9. Flow chart of the Gummel loop employed by the multiscale solver.

6.1.9 Mesh

The SHJ solar cell under consideration has a heavily doped a-Si:H(p) emitter layer (≈ 10^{19} cm^{-3}), an a-Si:H(i) passivation layer and a low doped absorber (≈ 10^{16} cm^{-3}) c-Si absorber. In such a design, the electric field will vary rapidly in the depletion region and eventually go to zero in the quasi neutral regions. Therefore, a fine mesh should be used for the regions where the fields vary rapidly, and a coarse mesh can be used for low field areas. However, having different meshes for the EMC and drift-diffusion solver would lead to a few complications. The results from the EMC mesh would have to be interpolated back on to the drift-diffusion mesh. It is much simpler to adopt a single meshing strategy for both the solvers. For simplicity we use a fine uniform mesh in the region where the EMC

operates (i.e. the high field region at the interface) and a non-uniform coarse mesh in the low field regions. A uniform mesh in the EMC region is used to avoid complications arising from self-forces.

6.2 Results and Analysis

To understand current matching between the EMC and drift-diffusion solvers, a silicon homojunction solar cell was used as a test structure. As shown in Fig. 6.10, a simple silicon *pn* homojunction solar cell was used with a thin emitter (20 nm) and a thick absorber (3 µm). Most silicon based solar cells use absorbers which are ~ 100 µm. A smaller absorber is used for computational efficiency as the purpose of this section is to explain the schemes employed to obtain current matching between the EMC and the drift-diffusion solvers. In the following sections, two scenarios are explored where, 1) the EMC extraction boundary is placed at the contact and 2) the EMC extraction boundary is placed in the depletion region.

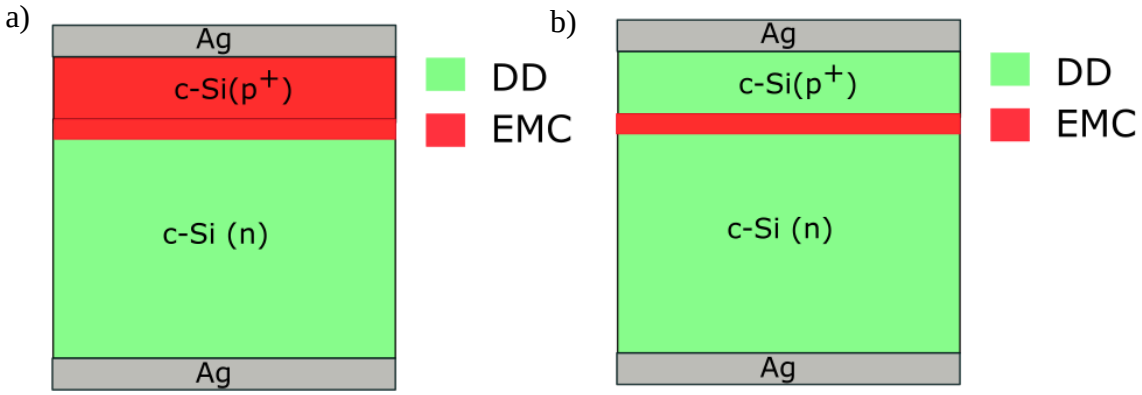

Figure 6.10. A *pn* junction test structure to study the coupling of the drift-diffusion and EMC solvers where: a) the EMC extraction boundary is placed at the contact, and b) the EMC extraction boundary is placed away from the contact.

6.2.1 Collecting Boundary at the Contact

In this section, the EMC extraction boundary is placed at the front contact of the solar cell (shown in Fig 6.10a). As mentioned earlier in this chapter, the number of particles injected into the EMC domain is obtained from the current calculated by the drift-diffusion equation. However, the short circuit current density in a solar cell is usually quite low, even world record efficiency cells, such as the 25.6% cell from 2015 has a short circuit current ≈ 41 mA/cm^2 [7]. To increase the injection statistics, the test structure is illuminated with 1000 suns, as can be seen in the charge density profile shown in Fig. 6.11. While this scenario is impractical in reality; it is an acceptable mathematical trick to establish the current matching process between the EMC and drift-diffusion solvers as a proof of concept.

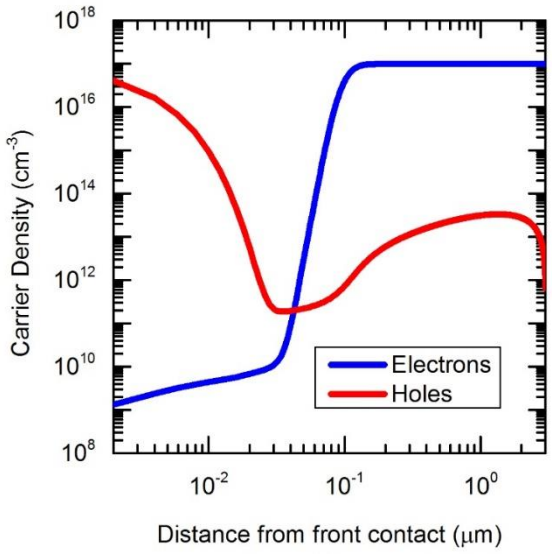

Figure 6.11. Charge density profile of the test structure under a 1000 suns illumination.

Figure 6.12 shows the current density profile for both electrons and holes in the device, where the EMC window extends from the front contact to some point at the edge of the depletion region (shown by dashed line in Fig. 6.12), where the electric fields < 10 kV/cm. As the carrier density varies rapidly in magnitude across the depletion region, the cells of the EMC window near the contact are extremely dense, whereas, the cells in the depletion region are extremely sparse (as shown in Fig. 6.13). As the doping density is high in the emitter, the contact cell population can be ~ 10^6 carriers, whereas, some cells at the edge of the depletion region might have a carrier population ~ 0. This can lead to significant statistical noise in the EMC simulations as the amount of charge being injected over a period of time (picoseconds) is orders of magnitude lower than the charge present in the contact cell.

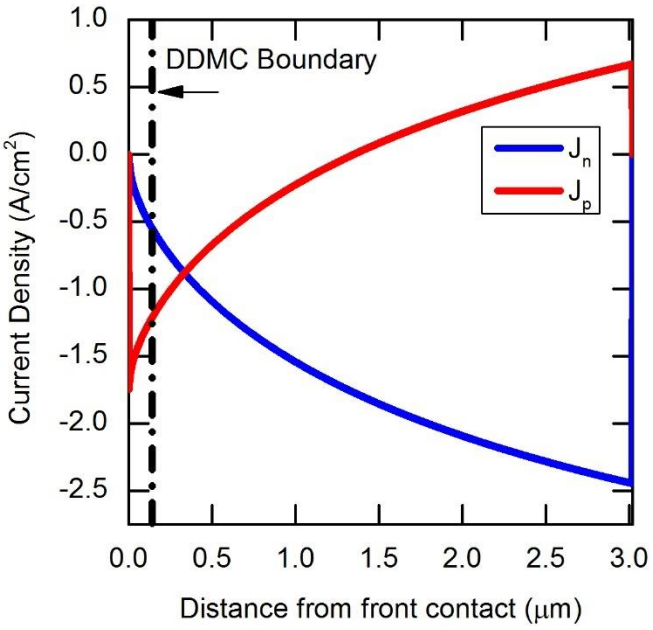

Figure 6.12. Electron and hole current density profile. The dashed line indicates the Monte Carlo/drift-diffusion boundary.

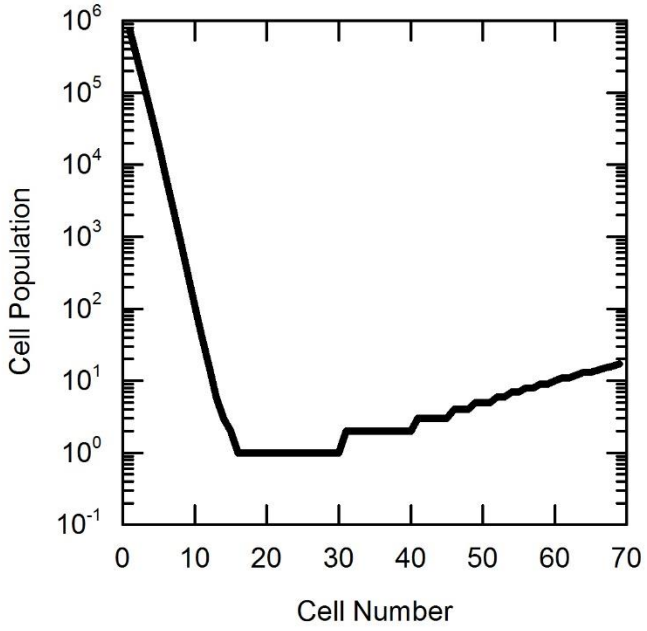

Figure 6.13. Cell population for every cell in the Monte Carlo domain.

To understand the effect of injection statistics, a current of 100 A/cm^2 (see Fig. 6.14) was injected into the EMC, and its characteristics were compared to an injection level of 50 mA/cm^2. Figure 6.14a shows the cumulative charge extracted at the front contact vs. time. The slope (*dq/dt*) gives us the magnitude of the current being extracted. It is evident from the figure that the cumulative charge increases linearly after about 2 picoseconds, thus the current can be extracted accurately. Figure 6.14b shows that the total amount of charge present in the EMC domain saturates and reaches steady state after 2 picoseconds. Similarly, Figure 6.14c shows that the flux being extracted at every time step at the left contact has a transient feature from 0 - 1 picosecond but quickly settles into steady state like behavior.

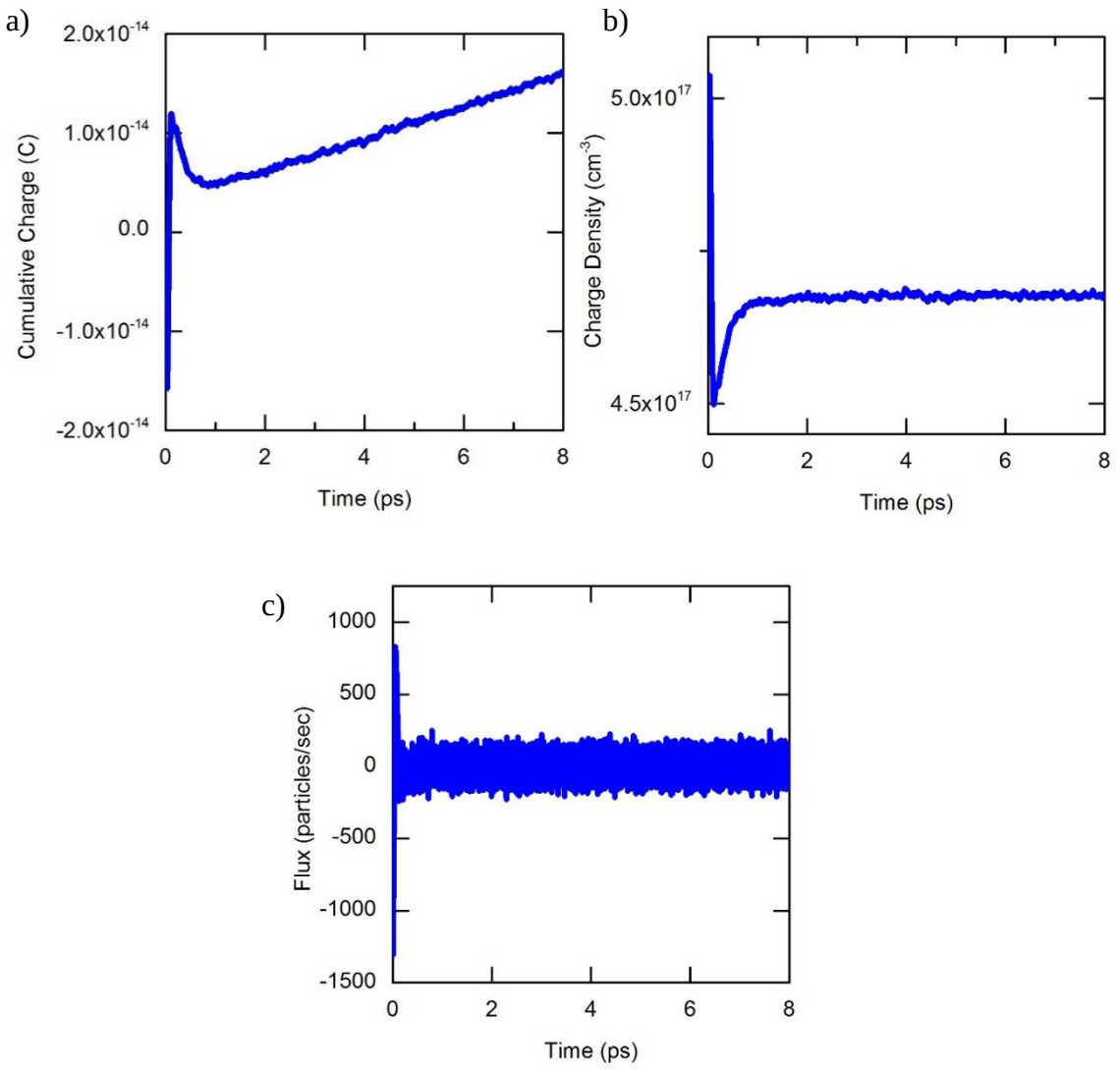

Figure 6.14. EMC charge characteristics corresponding to an injection of 100 mA/cm^2. a) Cumulative charge extracted at the front contact vs. time. b) Total charge density in the EMC domain vs. time. c) Flux extracted at the front contact per Δt (0.2 femto seconds) vs. Time.

Figure 6.15 shows the EMC characteristics for an injection level of 50 mA/cm^2. As we can see in Fig. 6.15a, the cumulative charge is observed over 40 picoseconds, but there is no noticeable slope. This is because the injected charge is orders of magnitude lesser than

the charge present in the contact cell, and as compared to the charge present in the EMC domain. When the charge in the contact cell far exceeds the amount of charge being injected into the EMC domain, the net flux at the contact cell caused by the charge neutrality boundary condition induces a significant amount of noise in the current calculations.

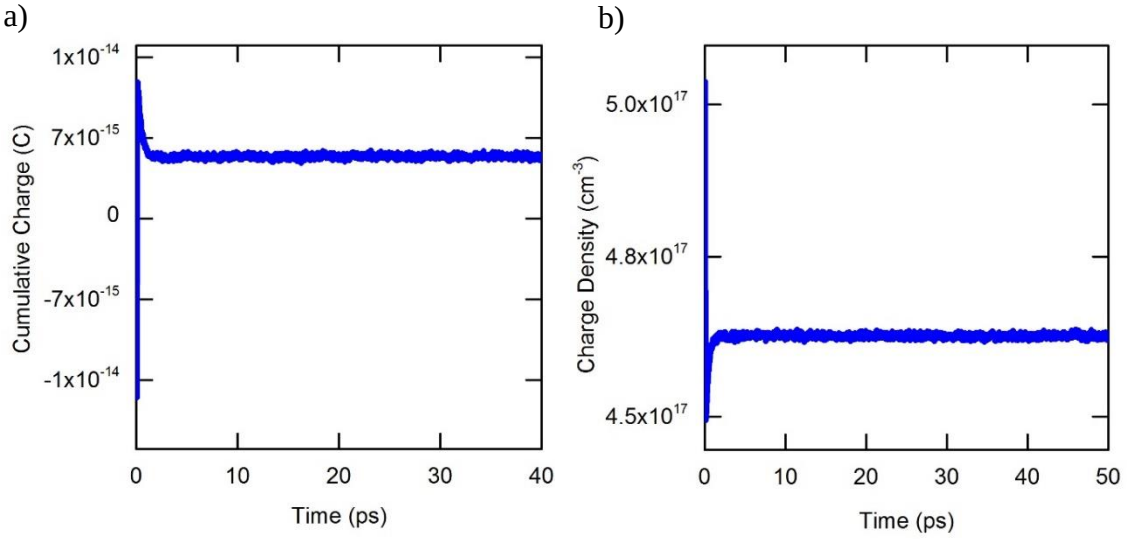

Figure 6.15. EMC characteristics for an injection level of 50 mA/cm^2. a) Cumulative charge extracted at the front contact vs. time. b) Total charge present in the EMC domain vs. time.

There are some charge enhancement techniques that can be used to boost poor injection statistics. However, in this case, the most effective strategy to represent the current proved to be data collection over longer periods of time (30 - 100 ps). It is possible to use weighted carriers [91] to improve the statistics of the EMC. In this case, the use of weighted carriers does not change the fact that the amount of charge being injected is far less than the charge present in the simulation domain. To put things into perspective, while injecting 100 A/cm^2, $\approx 10^5$ carriers can be injected over 8 picoseconds, whereas, while injecting 50

mA/cm^2, ≈500 carriers are injected over 50 pico seconds. Therefore, to represent lower currents, longer simulation runs are needed to collect the required statistics; and the application of data processing techniques can be used to extract the current. Figure 6.16 shows the cumulative charge vs. time after the application of a moving average filter. This shows the existence of a slope and a liner fit predicts an extracted current ~ 49.8 mA/cm^2 which is very close to the injected current (54 mA/cm^2). Even a linear fit through the noisy data in Fig. 6.16 gives a current of 46.4 mA/cm^2. However, after data processing, the slope becomes visible due to the removal of all the high frequency noise.

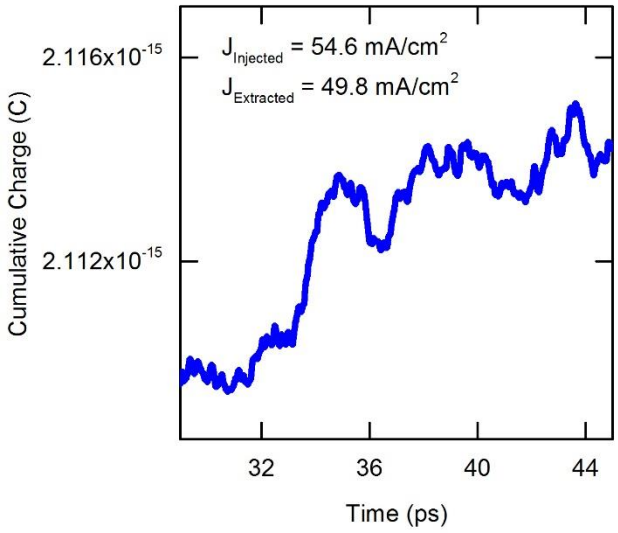

Figure 6.16. A moving average filter can be applied to the noisy cumulative charge data. a) Cumulative charge vs. time after using a moving average filter.

The hole current calculated by drift-diffusion for the test structure (Fig 6.16a) under a 1000 suns ≈ 1.2 A/cm^2 and can be matched by the EMC in ~ 20 pico seconds. It should be noted that the EMC is self-consistently coupled with the Poisson's equation, i.e. the Poisson's equation recalculates the field on the charge distribution calculated by the EMC

at every time step ($\Delta t = 0.2$ fs). Also, the electron charge remains frozen for the duration that the EMC is calculating the hole distributions. Once the EMC is current matched to the drift-diffusion, the electron continuity equation is solved over the entire domain to calculate the electron charge density, and the hole continuity equation is solved only outside the EMC domain, i.e. the hole density calculated by the EMC remains frozen. In this case, the hole density calculated by the EMC at the edge of the depletion region was used as a boundary condition for the hole continuity equation. The electron and hole densities are then used by Poisson's equation to recalculate the potentials. This describes the entire iterative process (Gummel's loop) of coupling the drift-diffusion to the EMC.

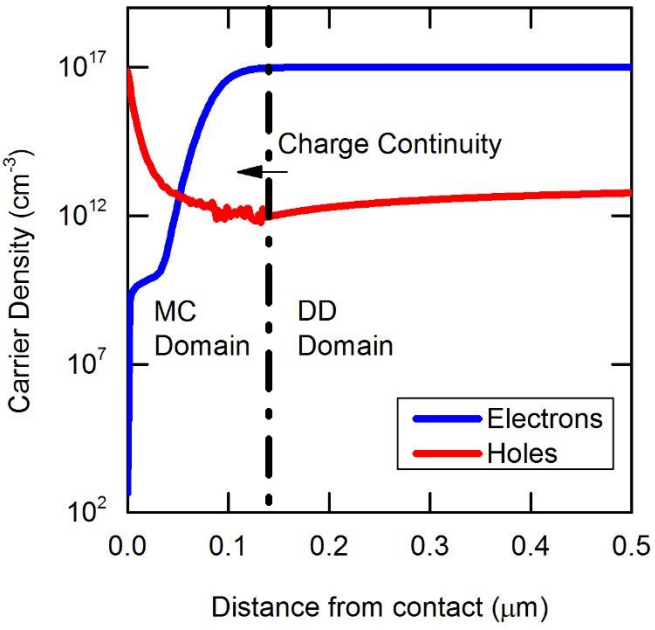

Figure 6.17. Charge density profile given by the self-consistent DDEMC solver.

Figure 6.17 shows that charge density is continuous across both domain after the self-consistent DDEMC solution. Minor fluctuations can also be noticed in the hole density

which is introduced by the stochastic nature of the EMC. It is imperative that there be charge continuity between across the two domains; any discontinuity will affect the potential. This will lead to spurious depletion of charge which will cause instability in the Poisson solution. Figure 6.18 shows the current density profile before and after the coupling of the drift-diffusion and EMC solvers. The aim of the self-consistent solution is to calculate the total current in the device with the inclusion of high field physics through the EMC solution. The total current is a factor of both the electron and hole currents. Only the holes are treated with the EMC solution, thus the electron current is still described over the entire domain by the drift-diffusion model. It is important to note that the total current must always be constant in the device. Figure 6.18a shows the total current density (calculated by drift-diffusion) over the entire device whereas Fig. 6.18b shows the total current density (calculated by the DDEMC) from the edge of DDEMC window across the drift-diffusion region. A slight slope can be observed in total current of the device (Fig. 6.18b). This slope is a function of the tolerance to which the solver has converged. Lower tolerances show higher slopes. A very low tolerance has to be used in order obtain a perfectly flat total current density profile. While this is easily achievable, it does add to the total computational time. For the purposes of computational efficiency, a lower tolerance can be used provides that the total current doesn't deviate more than few σ (standard deviations).

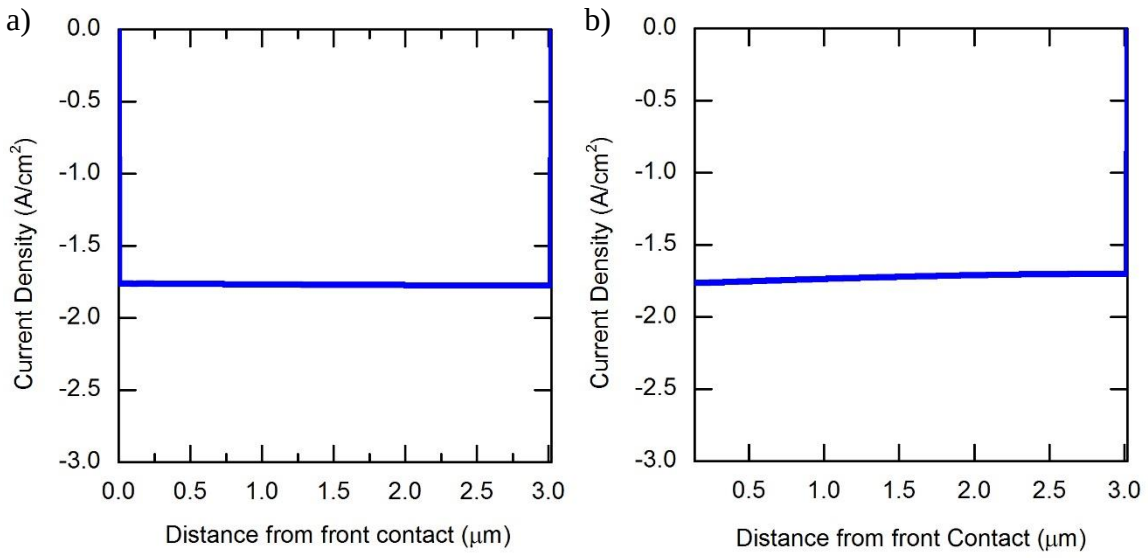

Figure 6.18. a) Total current density profile calculated by drift-diffusion. b) Total current density profile calculated by the DDMC.

Similarly, Fig. 6.19a and Fig. 6.19b shows the electron and hole current densities as calculated by drift-diffusion and DDEMC respectively. Figures 6.18 and 6.19 show the current densities that are obtained after one Gummel loop. In other words, the EMC has calculated a new injection conditions only once. To truly self-consistently couple both solvers, the injection condition must be calculated several times. Eventually, when the current stabilizes, it can be said that the two solvers have been self-consistently coupled. Figure 6.20 shows the hole current density that is calculated by the drift diffusion and is used as an injection condition for the EMC. Despite a slight initial increase, the current reaches a stable state within a few iterations. As described earlier, the use of EMC in dense regions of the depletion region leads to a domain with a large number of particles which leads to computational inefficiency. In this situation, the EMC is the rate limiting step of the solver due to which only a limited number of Gummel cycles can be performed.

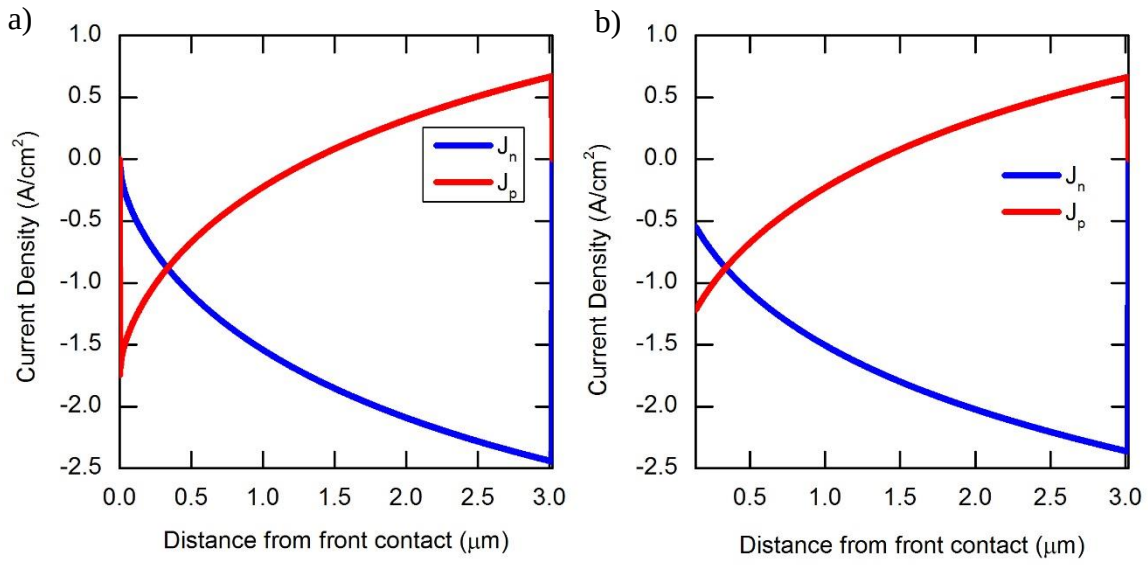

Figure 6.19. a) Electron and hole current density calculated by drift-diffusion. b) Electron and hole density calculated by the DDEMC (from the edge of the DDEMC window).

However, since the i^{th} Gummel cycle uses information such as charge densities, potentials and injection current from the $(i\text{-}1)^{th}$ Gummel cycle, a better initial guess reduces the amount of time required for current matching. As is evident from Fig. 6.21 ($J_{Extracted}$ = 1.22 A/cm^2), the EMC characteristics no longer have a transient trend where the cumulative charge and domain charge increases rapidly and then decreases to a steady state value. However, there is still significant noise in the characteristics which can only be overcome with longer simulation runs. Long simulation runs combined with a dense EMC domain means that even during successive Gummel cycles the EMC is still the rate limiting step.

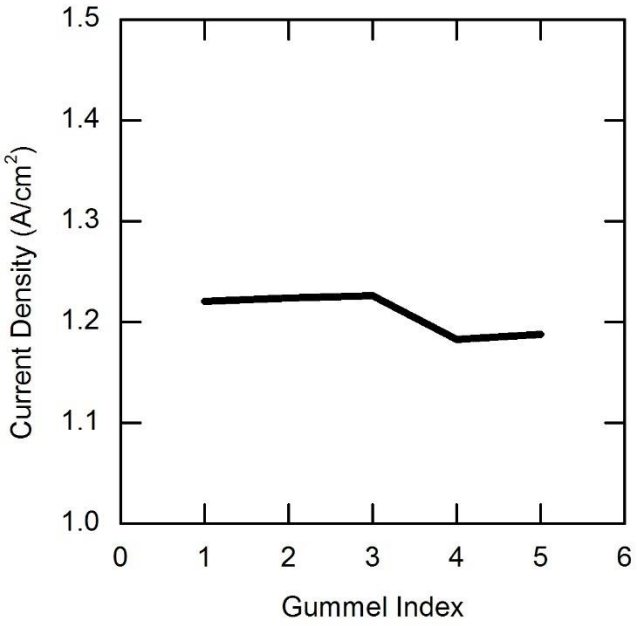

Figure 6.20. Hole current density injected into the EMC domain vs. Gummel Index (The index on the x scale represents the i^{th} iteration of the Gummel Loop).

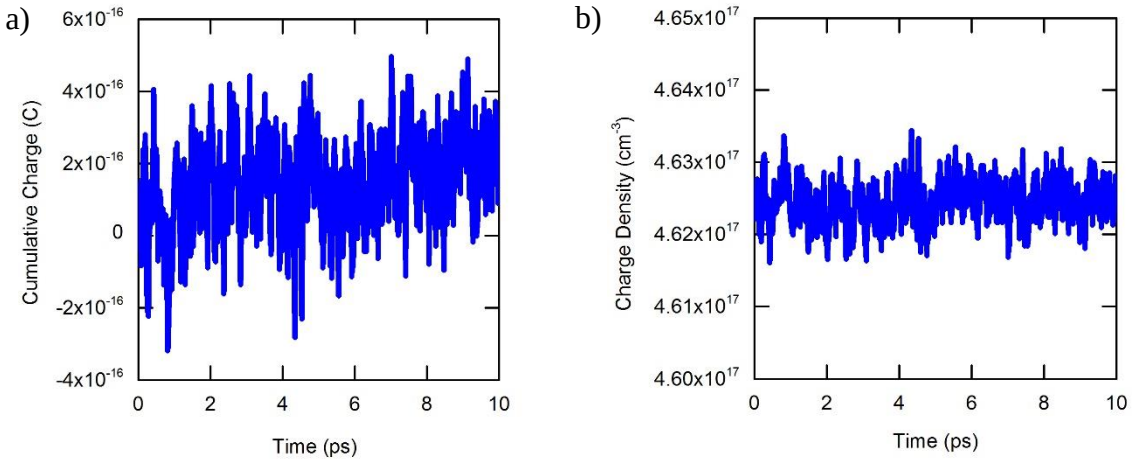

Figure 6.21. a) Cumulative charge density vs. time for i^{th} Gummel cycle. b) Total charge in the Monte Carlo domain vs. time for i^{th} Gummel cycle.

6.2.2 Weighted Carriers

A single carrier with a charge 'q' can be represented by 10 carriers with a charge ~ '$0.1q$'. By weighting carriers, 1 carrier can be replaced by 10 smaller carriers of equivalent charge or vice versa. This is also referred to as the super particle approach. In the previous section it was concluded that the weighted carrier scheme was not appropriate to boost injection statistics, as multiplying the number of carriers injected would not change the amount of charge being injected. Also, the source of the noise in the EMC was attributed to the large mismatch between the charge being injected and the charge present in the dense contact cells. However, this approach can be used to boost the population of cells present in the depletion region. A charge enhancement scheme which uses weighted carriers to increase the number of carriers representing the low depletion region charge [108] has been implemented. This improves the statistics representing the charge density in the EMC domain and improves the stability of the DDEMC.

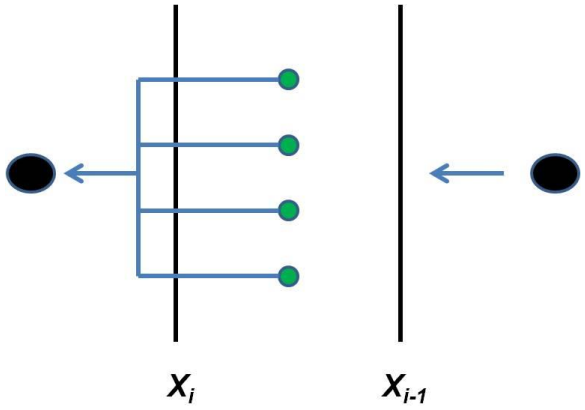

Figure 6.22. Visualization of charge enhancement in regions with low charge density.

6.2.3 Collecting Boundary Away from the Contact

In section 6.2.1, the extraction boundary of the EMC was placed at the contact. This led to the EMC domain encompassing the entirety of the heavily doped emitter which led to very a high EMC domain population, resulting in poor computational efficiency and noise issues while extracting current. In this section, the extraction boundary is placed away from the contact as show in Figure 6.10b. Since the EMC domain encompasses only the depletion region, the overall domain population is reduced (Fig. 6.23b), which allows accurate extraction of current (as shown in Fig. 6.23a). In this situation the convergence time of the drift-diffusion solver becomes the rate limiting step. By implementing this strategy, more Gummel iterations can be run in a shorter amount of time (as shown by Fig. 6.24). Figure 6.24 shows that hole injection current doesn't change drastically and is quite stable.

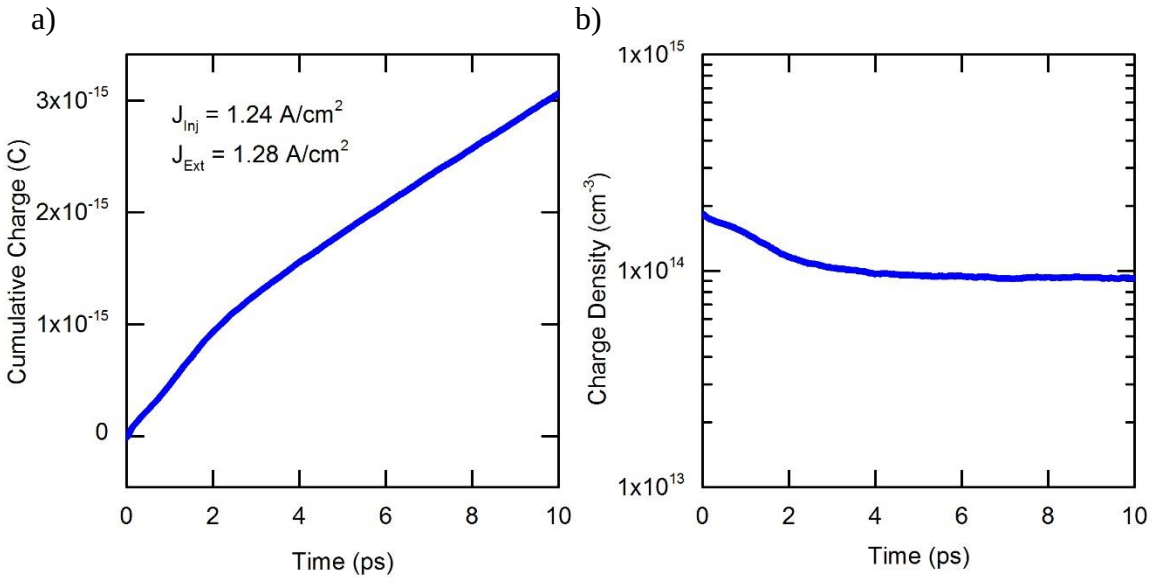

Figure 6.23. Cumulative charge (a) and total device charge (a) vs. time when the collecting boundary is placed away from the contact.

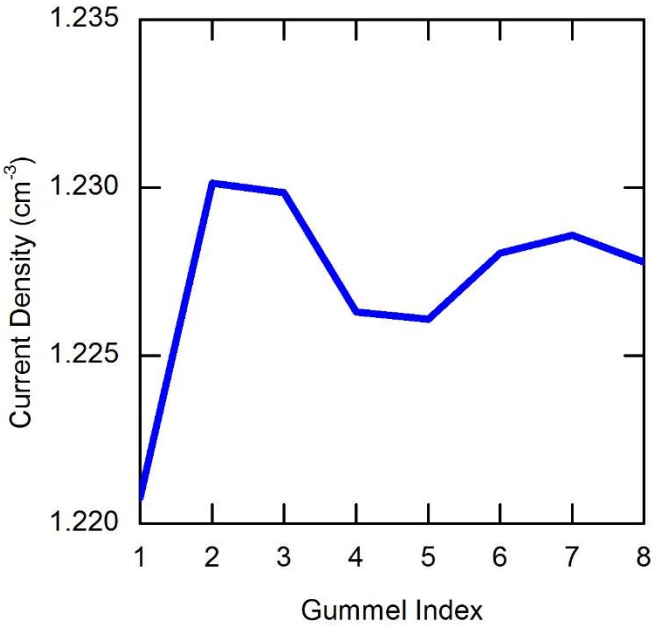

Figure 6.24. Hole injection current vs. i^{th} Gummel iteration.

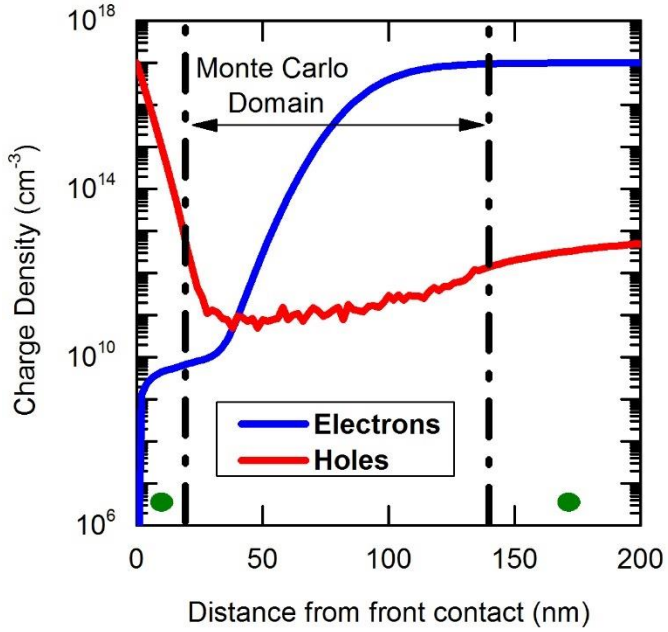

Figure 6.25. Charge density profile using a collecting boundary placed away from the contact. The Monte Carlo domain lies between the black dashed lines, whereas the green circles indicate the drift-diffusion regions.

Figure 6.25 shows the charge density calculated by the DDEMC solver with the collecting boundary placed away from the contact. To achieve charge continuity across the drift-diffusion and EMC domains, the EMC solver used an injection boundary condition at the collecting boundary, and a "fixed charge density" boundary condition at the extraction boundary. The hole continuity equation was solved outside the EMC domain, where Dirichlet boundary conditions were implemented at the contact boundaries C_1 and C_2. Fixed charge boundary conditions were implemented at boundaries B_1 and B_2 where the value of charge was calculated by the EMC solution.

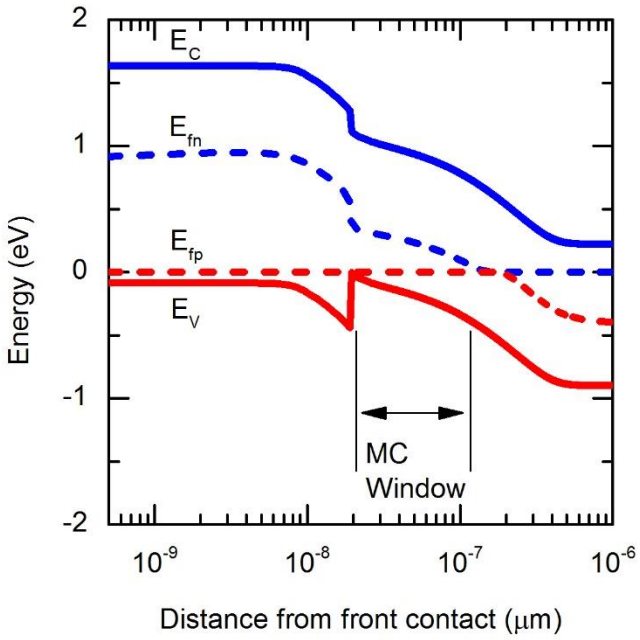

Figure 6.26. Band diagram at the front contact of a SHJ under short circuit conditions as calculated by the drift-diffusion solver. The figure also indicates the region in which the EMC is implemented.

The DDEMC methodology was also applied to a SHJ test structure with an a-Si:H(p) layer ~ 40 nm with doping ~ 10^{19} cm^{-3}, an a-Si:H(i) layer ~ 10 nm, and an n-type c-Si

absorber ~ 3 μm in thickness. Figure 6.26 shows the equilibrium band diagram of the front contact of a SHJ solar cell at short circuit conditions as calculated by the drift-diffusion solver. The EMC solution was applied to a small window near the a-Si:H(i)/c-Si heterointerface as shown in Fig. 6.26. Due to the nature of the "inversion" region in the SHJ cell, the hole carrier density decays by orders of magnitude within a few nm's, i.e. 10^{19} cm^{-3} – 10^{14} cm^{-3} within 40 nm. Thus, a smaller window ~ 10 nm is applied at the a-Si:H(i)/c-Si heterointerface in order to reproduce the injection current accurately. This approach does require careful consideration, which is further discussed in Section 6.3.

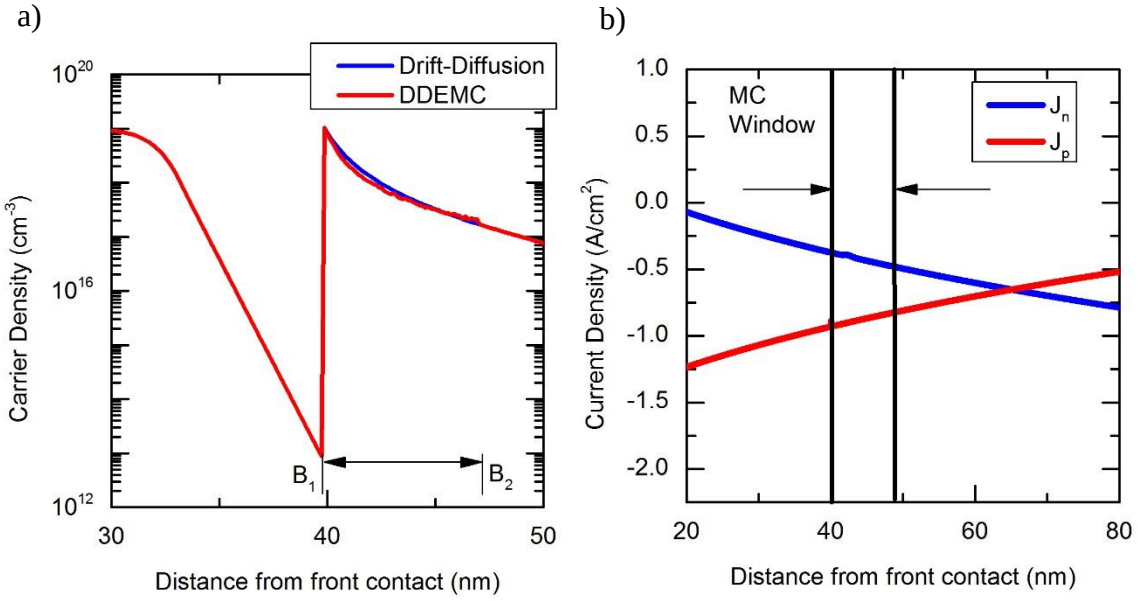

Figure 6.27. a) Hole charge density as calculated by the drift-diffusion (blue) and DDEMC (red). b) Hole current (red) and electron current (blue) as calculated by the DDEMC.

Figure 6.27a shows the hole charge density at the a-Si:H(i)/c-Si heterointerface, and Fig. 6.27b shows the electron and hole current profiles as calculated by the coupled DDEMC solution. For the results in Fig. 6.27 the EMC used an injection boundary

condition at boundary B_2. At the boundary B_1, carriers were extracted based on direct tunneling and thermionic emission, and reinjection was performed according to the "fixed charge" boundary condition.

6.3 Conclusion

In this chapter, a strategy was presented to couple an EMC solver to a drift-diffusion solver to study high field effects in silicon heterojunction solar cells. Previously, studies that have coupled drift-diffusion to EMC solvers use parameters (charge density, carrier velocity) obtained from the EMC solution, and use it in a "modified" drift-diffusion equation; this modified drift-diffusion equation is then solved over the entire domain [93,98]. The approach presented in this chapter differs from previous approaches as the charge calculated by the EMC domain is frozen, so that the integrity of the EMC solution is preserved. However, this approach creates two drift-diffusion domains that are separated by the EMC domain (see Figure 6.8). The hole continuity equations are solved in the drift-diffusion domains while sharing a boundary with the EMC domain. Using the correct boundary conditions is imperative to ensure continuity of charge and current across the shared boundaries of the drift-diffusion and EMC solvers.

The EMC has two boundaries, namely 1) the injection boundary that is placed in the low field quasi-neutral region of the c-Si, and 2) the extraction boundary that is placed at the a-Si:H(i)/c-Si heterointerface. At the injection boundary, current calculated by the drift-diffusion is injected into the EMC domain. However, the extraction boundary is a complicated matter. Carrier are extracted based on a tunneling probability. A "fixed charge density" boundary condition is used to ensure that extraction boundary cell does not get

depleted by extracted carriers. This implies that carriers are injected into the extraction boundary cell to maintain a "fixed charge density". It is unclear what the energy distribution of the reinjected carriers should be. Reinjecting a Maxwellian distribution into the extraction boundary cell might lead to 'cooling' of the carrier distribution at the a-Si:H(i)/c-Si heterointerface. At present, the carriers at the a-Si:H(i)/c-Si heterointerface are being extracted using a simple WKB based tunneling probability which does not factor in the phonon assisted transport across the a-Si:H(i) layer described Chapter 5.

Once the EMC solution determines the hole charge density, the hole continuity solution must recalculate the hole density on either side of the EMC domain. Dirichlet boundary conditions can be used at the contacts C_1 and C_2 (see Fig. 6.8). There are two types of boundary conditions that were used at the internal boundaries B_1 and B_2. At B_2 (also the injection boundary for the EMC), a "fixed charge density" boundary condition was used. This charge density was determined by the EMC solution. However, we also used a RBC at B_2, where the current flux at the boundary is the initial flux calculated by the drift-diffusion. Similarly, a "fixed charge density" boundary condition and a RBC was used at B_1. In both scenarios, the charge density at B_1 was preserved across multiple Gummel cycles. Even though a stable solution was achieved using both types of boundary conditions, it is unclear which boundary conditions should be used to see a real change in hole current density. It would appear that by using the suggested boundary conditions, the DDEMC solver is pathologically recreating the initial flux conditions calculated by the drift-diffusion solver.

As described earlier in this thesis, the EMC solution captures the effect of high electric fields on the hole carrier population; and the DDEMC solution integrates the EMC solution into a drift-diffusion framework. The electron density in the SHJ is treated with the drift-diffusion model over the entire domain. The total current density in the device is the sum of electron and hole current densities; which must be constant over the entire domain. In results presented in this chapter, the hole current density at the injection (B_2) and extraction (B_1) boundaries were discussed. It is unclear how to treat the hole current density within the EMC domain and therefore the entire hole current density profile in the device. In this chapter, the total current density was calculated at injection boundary (B_2). A scheme must be developed to address current density of electrons/holes and resolve it with the total current density of the device.

There are several non-trivial numerical challenges that must be overcome when coupling an EMC solution to a drift-diffusion solver in a bipolar device. The application of the EMC window must be compatible with several assumptions, such as, no recombination in the EMC domain, and the distribution function at the boundaries of the EMC must be near equilibrium. However, due to the unique structure and hole charge density profile of the SHJ solar cell, the conditions above cannot be strictly adhered to. The extraction boundary (B_1) of the EMC is placed in a high field region at the a-Si:H(i)/c-Si heterointerface, as the EMC cannot operate in the a-Si:H(i). The injection boundary (B_2) of the EMC cannot be placed in the quasi-neutral region in the c-Si where electric fields < 10 kV/cm as it results in disproportionately dense extraction boundary cells.

CHAPTER 7

CONCLUSIONS AND FUTURE WORK

The research work presented in this thesis investigates the transport of photogenerated holes in a SHJ solar cell structure. In particular, the impact of the a-Si:H(i)/c-Si heterointerface, and the a-Si:H(i) passivation layer on transport properties was investigated. Several theoretical methodologies were developed to gain insight into transport behavior and device properties of the SHJ solar cell. In Chapter 3, a commercial TCAD tool was utilized to study the impact of the ITO(n^+)/a-Si:H(p) and a-Si:H(i)/c-Si heterointerfaces on the contact resistivity of a SHJ solar cell. To investigate the contact resistivity behavior of carrier-selective contacts in SHJ solar cells, the TLM measurement technique was simulated. Using the drift-diffusion model of a commercially available TCAD tool (Silvaco), it is possible to simulate other measurement techniques that are used to characterize solar cells, such as various contactless measurements and lifetime measurements. Though there are limitations in applying the drift-diffusion model to study novel device structures where this model is not valid, it is possible to add several corrections to the drift-diffusion model, and thus gain insight into the device properties of solar cells.

In Chapter 4, an EMC solver was developed to investigate the effect of high electric fields on the energy distribution function of photogenerated holes at the a-Si:H(i)/c-Si heterointerface. The EMC solution established the presence of a non-Maxwellian energy distribution function of injected photogenerated carriers at the a-Si:H(i)/c-Si heterointerface; this violates the assumption made in the drift-diffusion model. However,

the EMC solution also showed that the energy distribution function of carriers in low-field areas of the device is Maxwellian. Acoustic phonon and non-polar optical phonon models were used to describe scattering of holes in c-Si, while also considering warping and non-parabolicity of the valence band. Considering that the a-Si:H(i)/c-Si heterointerface has a high-density inversion layer of holes, a carrier-carrier scattering model can offer further insight into the energy distribution function at the heterointerface. As the photogenerated holes must traverse the potential barrier created by the a-Si:H(i)/c-Si heterointerface, an 'energized' or 'hot-carrier' population at the heterointerface can be beneficial for efficient transport.

To investigate hole transport across the a-Si:H(i) layer, a KMC solver was developed (described in Chapter 5). The KMC solution showed that multi-phonon injection of holes into the a-Si:H(i) layer is the rate limiting step for transport across the barrier; this injection process is critical to avoid photocurrent suppression in the SHJ structure. Photocurrent suppression at the a-Si:H(i)/c-Si barrier can be viewed as a charge pileup, where photogenerated carriers that are incident on the a-Si:H(i)/c-Si heterointerface do not get extracted quickly. In other words, the rate of incidence of photocarriers at the a-Si:H(i)/c-Si heterointerface is much faster than the rate of extraction of carriers. The rate of incidence of carriers at the a-Si:H(i)/c-Si barrier is function of the short-circuit current in the device. The rate of extraction of carriers across the a-Si:H(i) barrier is computed by the KMC, where carriers traverse the barrier via multi-phonon injection into the a-Si:H(i) layer, hopping via defect states in the a-Si:H(i) layer, and finally exit the a-Si:H(i) layer into the a-Si:H(p) layer via Poole-Frenkel emission and defect emission. The KMC simulations

show that the average transit time of carriers across the a-Si:H(i) can vary orders of magnitude depending on properties of the a-Si:H(i) layer, such as, thickness, band-tail defect density, electric field and optical phonon energy. Therefore, it is essential to optimize the a-Si:H(i) layer to obtain efficient electrical transport across this layer. As mentioned earlier, photocurrent suppression occurs when the rate of extraction of carriers from the a-Si:H(i)/c-Si heterointerface $\ll$ rate of incidence of carriers at the a-Si:H(i)/c-Si heterointerface. An imbalance in the rates causes transport across the a-Si:H(i)/c-Si heterointerface to be more resistive, which is expected to cause a degradation in the fill factor and hence a degradation in the overall device performance. This work can be extended by coupling the KMC self-consistently to a standard drift-diffusion model, which would enable one to see the effect of the microscopic transport mechanisms (described in Chapter 5) on macroscopic device performance parameters such as fill factor.

The KMC method can also be extended to study transport properties of novel materials that are being investigated for the purposes of forming a new generation of electron (TiO_x) and hole selective (MoO_x and WoO_x) contacts. There are several studies that show that defect-assisted transport is going to be crucial for electrical transport of photocarriers in these carrier-selective contacts, and thus the KMC is an ideal method to study this behavior.

As an extension to this work, the results of the KMC simulations can also be added to the drift-diffusion model non-self-consistently. Deviations from drift and diffusion current can be added as corrections to the drift-diffusion model. In particular, thermionic emission and field emission can be added to the drift-diffusion model as a boundary condition to the current equations. The field emission is generally characterized by a transmission

coefficient ‘δ’ representing direct tunneling. Similarly, the ‘δ’ term can be extended to represent a hopping transmission coefficient, which can be calculated by the KMC. The KMC solver presented in this thesis can easily be extended to study other novel materials that are being explored to improve the carrier selective contact structure.

In Chapter 6, a novel strategy to couple an EMC to a drift-diffusion solver was presented. To fully solve the multiscale problem present in the SHJ solar cell, it is imperative to self-consistently couple all the three modules presented in this thesis. The decoupled simulations presented in this thesis provides great resolution in the physics of transport of photogenerated carriers. A fully self-consistent model can correlate the overall effect microscopic physical mechanisms to device performance parameters. However, to achieve complete self-consistency is a non-trivial task that requires a rigorous mathematical analysis of boundary conditions that connects continuum models to discrete models.

REFERENCES

[1] A. B. Arons and M. B. Peppard, “Einstein’s Proposal of the Photon Concept - A Translation of the Annalen der Physik Paper of 1905,” *Am. J. Phys.*, vol. 33, no. 5, 1965.

[2] A. Chodos, “APS news,” *Am. Phys. Soc.*, vol. 18, no. 4, p. 2, 2009.

[3] W. Shockley and H. J. Queisser, “Detailed Balance Limit of Efficiency of p-n Junction Solar Cells,” *J. Appl. Phys.*, vol. 32, no. 3, pp. 510–519, 1961.

[4] A. Richter, M. Hermle, and S. W. Glunz, “Reassessment of the Limiting Efficiency for Crystalline Silicon Solar Cells,” *IEEE J. Photovoltaics*, vol. 3, no. 4, pp. 1184–1191, 2013.

[5] M. A. Green, A. W. Blakers, J. Zhao, A. M. Milne, A. Wang, and X. Dai, “Characterization of 23-Percent Efficient Silicon Solar Cells,” *IEEE Trans. Electron Devices*, vol. 37, no. 2, pp. 331–336, 1990.

[6] J. Zhao, A. Wang, and M. A. Green, “24% Efficient PERL Structure Silicon Solar Cells.” pp. 333–335, 2002.

[7] B. Steinhauser *et al.*, “Large Area TOPCon Technology Achieving 23.4% Efficiency,” *2018 IEEE 7th World Conf. Photovolt. Energy Conversion, WCPEC 2018 - A Jt. Conf. 45th IEEE PVSC, 28th PVSEC 34th EU PVSEC*, pp. 1507–1510, 2018.

[8] M. Tanaka *et al.*, “Development of New a-Si/c-Si Heterojunction Solar Cells : ACJ-HIT (Artificially Constructed Junction-Heterojunction with Intrinsic Thin-Layer),” *Jpn. J Appl. Phys*, vol. 31, pp. 3518–3522, 1992.

[9] M. Taguchi *et al.*, “24.7% Record Efficiency HIT Solar Cell on Thin Silicon Wafer,” *IEEE J. Photovoltaics*, vol. 4, no. 1, pp. 96–99, 2014.

[10] K. Masuko *et al.*, “Achievement of More Than 25% Conversion Efficiency With Crystalline Silicon Heterojunction Solar Cell,” *IEEE J. Photovoltaics*, vol. 4, no. 6, pp. 1433–1435, 2014.

[11] K. Yamamoto, K. Yoshikawa, H. Uzu, and D. Adachi, “High-Efficiency Heterojunction Crystalline Si Solar Cells,” *Jpn. J Appl. Phys*, vol. 57, 2018.

[12] J. Liu, Y. Yao, S. Xiao, and X. Gu, “Review of Status Developments of High-Efficiency Crystalline Silicon Solar Cells,” *J. Phys. D. Appl. Phys.*, vol. 51, no. 12, 2018.

[13] S. W. Glunz *et al.*, "The irresistible charm of a simple current flow pattern - 25% with a solar cell featuring a full area back contact," in *31st European Photovoltaic Solar Energy Conference and Exhibition*, 2015, no. September.

[14] M. J. Kerr, A. Cuevas, and P. Campbell, "Limiting Efficiency of Crystalline Silicon Solar Cells Due to Coulomb-Enhanced Auger Recombination," *Prog. Photovoltaics Res. Appl.*, vol. 11, no. 2, pp. 97–104, 2003.

[15] J. Melskens, B. W. H. Van De Loo, B. Macco, L. E. Black, S. Smit, and W. M. M. E. Kessels, "Passivating Contacts for Crystalline Silicon Solar Cells : From Concepts and Materials to Prospects," *IEEE J. Photovoltaics*, vol. 8, no. 2, pp. 373–388, 2018.

[16] A. Cuevas, "The recombination parameter J0," in *Energy Procedia*, 2014, vol. 55, pp. 53–62.

[17] M. A. Green, "The Passivated Emitter and Rear Cell (PERC): From conception to mass production," *Sol. Energy Mater. Sol. Cells*, vol. 143, pp. 190–197, 2015.

[18] A. Cuevas, T. Allen, and J. Bullock, "Skin care for healthy silicon solar cells," *2015 IEEE 42nd Photovolt. Spec. Conf.*, no. 1, pp. 1–6, 2015.

[19] S. de Wolf *et al.*, "High-efficiency Silicon Heterojunction Solar Cells: A Review," *Green*, vol. 2, no. JANUARY, pp. 7–24, 2012.

[20] K. K. Ng and H. C. Card, "Asymmetry in the SiO2 tunneling barriers to electrons and holes," *J. Appl. Phys.*, vol. 51, no. 4, pp. 2153–2157, 1980.

[21] M. Taguchi, A. Terakawa, E. Maruyama, and M. Tanaka, "Obtaining a Higher Voc in HIT Cells," *Prog. Photovoltaics Res. Appl.*, vol. 13, no. 6, pp. 481–488, 2005.

[22] D. K. Ferry, *Semiconductors*. 1991.

[23] R. E. . Schropp and M. Zeman, *Amorphous and Microcystalline Solar Cells: Modeling, Materials and Device Technology*. Kluwer Academic Publishers, 1998.

[24] R. L. Anderson, "Germanium-Gallium Arsenide Heterojunctions [Letter to the Editor]," *IBM J. Res. Dev.*, vol. 4, no. 3, pp. 283–287, 1960.

[25] M. S. Lundstrom and R. J. Schuelke, "Modeling Semiconductor Heterojunctions in Equilibrium," *Solid State Electron.*, vol. 25, no. 8, pp. 683–691, 1982.

[26] M. S. Lundstrom and R. J. Schuelke, "Numerical Analysis of Heterostructure Semiconductor Devices," *IEEE Trans. Electron Devices*, vol. 30, no. 9, pp. 1151–1159, 1983.

[27] U. Wurfel, A. Cuevas, and P. Wurfel, "Charge Carrier Separation in Solar Cells," *IEEE J. Photovoltaics*, vol. 5, no. 1, pp. 461–469, 2015.

[28] R. Brendel and R. Peibst, "Contact Selectivity and Efficiency in Crystalline Silicon Photovoltaics," *IEEE J. Photovoltaics*, vol. 6, no. 6, pp. 1413–1420, 2016.

[29] D. K. Schroder and D. L. Meier, "Solar Cell Contact Resistance - A Review," *IEEE Trans. Electron Devices*, vol. ED-31, no. 5, pp. 637–647, 1984.

[30] D. Lachenal *et al.*, "Heterojunction and Passivated Contacts : A Simple Method to Extract Both n/tco and p/tco Contacts Resistivity," *Energy Procedia*, vol. 92, pp. 932–938, 2016.

[31] S. Lee *et al.*, "Analysis of a-Si:H/TCO Contact Resistance for the Si Heterojunction Back-Contact Solar Cell," *Sol. Energy Mater. Sol. Cells*, vol. 120, pp. 412–416, 2014.

[32] D. L. Meier and D. K. Schroder, "Contact Resistance: Its Measurement and Relative Importance to Power Loss in a Solar Cell," *IEEE Trans. Electron Devices*, vol. 31, no. 5, pp. 647–653, 1984.

[33] R. S. Crandall, E. Iwaniczko, J. V. Li, and M. R. Page, "A Comprehensive Study of Hole Collection in Heterojunction Solar Cells," *J. Appl. Phys.*, vol. 112, no. 9, 2012.

[34] P. Muralidharan, S. Bowden, S. M. Goodnick, and D. Vasileska, "A Kinetic Monte Carlo Approach to Study Transport in Amorphous Silicon HIT Cells," *Photovolt. Spec. Conf. (PVSC), 2015 IEEE 42nd*, pp. 743–758, 2015.

[35] M. Taguchi, E. Maruyama, and M. Tanaka, "Temperature Dependence of Amorphous/Crystalline Silicon Heterojunction Solar Cells," *Jpn. J. Appl. Phys.*, vol. 47, no. 2, pp. 814–818, 2008.

[36] A. Kanevce and W. K. Metzger, "The role of amorphous silicon and tunneling in heterojunction with intrinsic thin layer (HIT) solar cells," *J. Appl. Phys.*, vol. 105, no. 9, pp. 1–7, 2009.

[37] R. Lachaume, W. Favre, P. Scheiblin, and X. Garros, "Influence of a-Si:H/ITO Interface Properties on Performance of Heterojunction Solar Cells," *Energy Procedia*, vol. 38, pp. 770–776, 2013.

[38] N. Hernández-Como and A. Morales-Acevedo, "Simulation of Hetero-Junction Silicon Solar Cells with AMPS-1D," *Sol. Energy Mater. Sol. Cells*, vol. 94, no. 1, pp. 62–67, 2010.

[39] R. Varache, J. P. Kleider, M. E. Gueunier-Farret, and L. Korte, "Silicon Heterojunction Solar Cells: Optimization of Emitter and Contact Properties from Analytical Calculation and Numerical Simulation," *Mater. Sci. Eng. B Solid-State Mater. Adv. Technol.*, vol. 178, no. 9, pp. 593–598, 2013.

[40] M. Leilaeioun *et al.*, "TLM Measurements Varying the Intrinsic a-Si:H Layer Thickness in Silicon Heterojunction Solar Cells," *Photovolt. Spec. Conf. (PVSC), 2017 IEEE 44th*, pp. 1790–1793, 2017.

[41] A. Klein *et al.*, "Transparent Conducting Oxides for Photovoltaics: Manipulation of Fermi Level,Work Function and Energy Band Alignment," *Materials (Basel).*, vol. 3, no. 11, pp. 4892–4914, 2010.

[42] M. Powell and S. Deane, "Defect-Pool Model and the Hydrogen Density of States in Hydrogenated Amorphous Silicon," *Phys. Rev. B*, vol. 53, no. 15, pp. 10121–10132, 1996.

[43] K. Horio and H. Yanai, "Numerical Modeling of Heterojunctions Including the Thermionic Emission Mechanism at the Heterojunction Interface," *IEEE Trans. Electron Devices*, vol. 37, no. 4, pp. 1093–1098, 1990.

[44] MeiKei Ieong, P. M. Solomon, S. E. Laux, H.-S. P. Wong, and D. Chidambarrao, "Comparison of Raised and Schottky Source/Drain MOSFETs Using a Novel Tunneling Contact Model," *Int. Electron Devices Meet. 1998. Tech. Dig. (Cat. No.98CH36217)*, pp. 733–736, 1998.

[45] K. Matsuzawa, K. Uchida, and A. Nishiyama, "A Unified Simulation of Schottky and Ohmic Contacts," *IEEE Trans. Electron Devices*, vol. 47, no. 1, pp. 103–108, 2000.

[46] A. Klein *et al.*, "Surface Potentials of Magnetron Sputtered Transparent Conducting Oxides," *Thin Solid Films*, vol. 518, no. 4, pp. 1197–1203, 2009.

[47] Y. Park, V. Choong, Y. Gao, B. R. Hsieh, and C. W. Tang, "Work Function of Indium Tin Oxide Transparent Conductor Measured by Photoelectron Spectroscopy," *Appl. Phys. Lett.*, vol. 68, no. 19, pp. 2699–2701, 1996.

[48] X. Xie, G. Liu, C. Xu, S. Li, Z. Liu, and E. C. Lee, "Tuning the Work Function of Indium-Tin-Oxide Electrodes for Low-Temperature-Processed, Titanium-Oxide-Free Perovskite Solar Cells," *Org. Electron. physics, Mater. Appl.*, vol. 44, pp. 120–125, 2017.

[49] M. Bivour, C. Reichel, M. Hermle, and S. W. Glunz, "Improving the a-Si:H(p) Rear Emitter Contact of n-Type Silicon Solar Cells," *Sol. Energy Mater. Sol. Cells*, vol.

106, pp. 11–16, 2012.

[50] D. Psych, C. Meinhard, N.-P. Harder, M. Hermle, and S. W. Glunz, “Analysis and Optimization Approach for the Doped Amorphous Layers of Silicon Heterojunction Solar Cells,” *Phys, J Appl*, vol. 094516, no. May 2011, 2015.

[51] A. Kanevce and W. K. Metzger, “Device Physics of Heterojunction with Intrinsic Thin Layer (HIT) Solar Cells,” *Mater. Res.*, vol. 1153, pp. 1–6, 2009.

[52] S. Kirner *et al.*, “The Influence of ITO Dopant Density on J-V Characteristics of Silicon Heterojunction Solar Cells: Experiments and Simulations,” *Energy Procedia*, vol. 77, no. i, pp. 725–732, 2015.

[53] K. Ghosh, S. Bowden, and C. Tracy, “Role of Hot Carriers in the Interfacial Transport in Amorphous Silicon/Crystalline Silicon Heterostructure Solar Cells,” *Phys. Status Solidi Appl. Mater. Sci.*, vol. 210, no. 2, pp. 413–419, 2013.

[54] P. Lawaetz, “Valence-Band Parameters in Cubic Semiconductors,” *Phys. Rev. B*, vol. 4, no. 10, pp. 3460–3467, 1971.

[55] J. Dewey and M. A. Osman, “Monte Carlo Study of Hole Transport in Silicon,” *J. Appl. Phys.*, vol. 74, p. 3219, 1993.

[56] J. D. Wiley, “Polar Mobility of Holes in III-V Compounds,” *Phys. Rev.*, vol. 4, 1971.

[57] N. Nintunze and M. a Osman, “Hole Drift Velocity in the Warped Band Model of GaAs,” *Semicond. Sci. Technol.*, vol. 10, no. 1, pp. 11–17, 1999.

[58] Y. Hayashi, D. Li, A. Ogura, and Y. Ohshita, “Role of i-aSi:H Layers in aSi:H/cSi Heterojunction Solar Cells,” *IEEE J. Photovoltaics*, vol. 3, no. 4, pp. 1149–1155, 2013.

[59] P. Muralidharan, K. Ghosh, D. Vasileska, and S. M. Goodnick, “Hot Hole Transport in a-Si / c-Si Heterojunction Solar Cells,” in *Photovoltaic Specialist Conference (PVSC), 2014 IEEE 40th*, 2014.

[60] P. Luppina, P. Lugli, and S. M. Goodnick, “Modeling of Silicon Heterojunction Solar Cells,” *2015 IEEE 42nd Photovolt. Spec. Conf.*, pp. 1–6, 2015.

[61] I. Martin-bragado, R. Borges, J. Pablo, and M. Jaraiz, “Progress in Materials Science Kinetic Monte Carlo simulation for semiconductor processing : A review,” *Prog. Mater. Sci.*, vol. 92, pp. 1–32, 2018.

[62] M. Carlo, G. Jegert, A. Kersch, W. Weinreich, U. Schröder, and P. Lugli, “Modeling

of Leakage Currents in High-k Dielectrics : Three-Dimensional Approach via Kinetic Monte Carlo," *Appl. Phys. Lett.*, vol. 96, 2010.

[63] J. J. M. van der Holst, "Three-dimensional modeling of charge transport, injection and recombination in organic light-emitting diodes," Technische Universiteit Eindhoven, 2010.

[64] T. Albes, B. Popescu, D. Popescu, M. Loch, F. Arca, and P. Lugli, "Kinetic Monte Carlo Modeling of Low-Bandgap Polymer Solar Cells," *2014 IEEE 40th Photovolt. Spec. Conf.*, pp. 57–62, 2014.

[65] K. G. Reyes, "Fast Kinetic Monte Carlo Simulations : Implementation, Application, and Analysis," The University of Michigan, 2013.

[66] U. Neupane, B. Bahrami, M. Biesecker, M. F. Baroughi, and Q. Qiao, "Kinetic Monte Carlo Modeling on Organic Solar Cells: Domain Size, Donor-Acceptor Ratio and Thickness," *Nano Energy*, vol. 35, no. November 2016, pp. 128–137, 2017.

[67] P. M. Baidya, K. Bayat, M. Biesecker, and M. F. Baroughi, "Kinetic Monte Carlo modeling of dark and illuminated current-voltage characteristics of Kinetic Monte Carlo modeling of dark and illuminated current-voltage characteristics of bulk heterojunction solar cells," *Appl. Phys. Lett.*, vol. 103, p. 063305, 2013.

[68] G. C. Jegert, "Modeling of Leakage Currents in High -k Dielectrics," Technische Universitat Munchen, 2012.

[69] X. Yang, P. Zheng, Q. Bi, and K. Weber, "Silicon Heterojunction Solar Cells with Electron Selective TiOx Contact," *Sol. Energy Mater. Sol. Cells*, vol. 150, pp. 32–38, 2016.

[70] M. Bivour, F. Zähringer, P. Ndione, and M. Hermle, "Sputter-Deposited WOx and MoOx for Hole Selective Contacts," *Energy Procedia*, vol. 124, pp. 400–405, 2017.

[71] C. Battaglia *et al.*, "Hole Selective MoOx Contact for Silicon Solar Cells," *Nano Lett.*, vol. 14, no. 2, pp. 967–971, 2014.

[72] C. Messmer, M. Bivour, J. Schön, S. W. Glunz, and M. Hermle, "Numerical Simulation of Silicon Heterojunction Solar Cells Featuring Metal Oxides as Carrier-Selective Contacts," *IEEE J. Photovoltaics J. Photovoltaics*, vol. 8, no. 2, pp. 456–464, 2018.

[73] R. A. Vijayan *et al.*, "Hole-Collection Mechanism in Passivating Metal-Oxide Contacts on Si Solar Cells: Insights from Numerical Simulations," *IEEE J. Photovoltaics*, vol. 8, no. 2, pp. 473–482, 2018.

[74] A. P. J. Jansen, *An Introduction to Kinetic Monte Carlo Simulations of Surface Reactions*. Springer, Berlin, Heidelberg, 2012.

[75] B. J. Garrison, "Molecular Dynamics Simulations of Surface Chemical Reactions," *Chem. Soc. Rev.*, vol. 21, p. 155, 1992.

[76] G. Kabbe, C. Wehmeyer, and D. Sebastiani, "A Coupled Molecular Dynamics/Kinetic Monte Carlo Approach for Protonation Dynamics in Extended Systems," *J. Chem. Theory Comput.*, vol. 10, pp. 4221–4228, 2014.

[77] G. A. M. Hurkx, D. B. M. Klaassen, and M. P. G. Knuvers, "A New Recombination Model for Device Simulation Including Tunneling," *IEEE Trans. Electron Devices*, vol. 39, no. 2, pp. 331–338, 1992.

[78] A. Schenk, "A Model For The Field And Temperature Dependence Of Schockley-Read-Hall Lifetimes in Silicon," *Solid State Electron.*, vol. 35, no. 11, pp. 1585–1596, 1992.

[79] R. A. Street, *Hydrogenated Amorphous Silicon*. Cambridge University Press, 1991.

[80] D. T. Gillespie, "A General Method for Numerically Simulating the Stochastic Time Evolution of Coupled Chemical Reactions," *J. Comput. Phys.*, vol. 22, no. 4, pp. 403–434, 1976.

[81] W. W. Lui and M. Fukuma, "Exact Solution of the Schrodinger Equation Across an Arbitary One Dimensional Piecewise-Linear Barrier," *J. Appl. Phys.*, vol. 60, pp. 1555–1559, 1986.

[82] I. Lundström and C. Svensson, "Tunneling to Traps in Insulators," *J. Appl. Phys.*, vol. 43, no. 12, pp. 5045–5047, 1972.

[83] J. Bardeen, "Tunneling from a Many Particle Point of View," *Phys. Rev. Lett.*, vol. 6, no. 2, pp. 57–59, 1961.

[84] M. Herrmann and A. Schenk, "Field and High-Temperature Dependence of the Long Term Charge Loss in Erasable Programmable Read Only Memories: Measurements and Modeling," *J. Appl. Phys.*, vol. 77, no. 9, pp. 4522–4540, 1995.

[85] V. G. Robles and G. G. De La Cruz, "Photoionization of Deep Impurity Centers in Semiconductors," *Phys. Rev. B*, vol. 3, pp. 299–302, 1965.

[86] A. Miller and E. Abrahams, "Impurity Conduction at Low Concentrations," *Phys. Rev.*, vol. 120, no. 3, pp. 745–755, 1960.

[87] J. Frenkel, “On Pre-Breakdown Phenomena in Insulators and Electronic Semi-Conductors,” *Phys. Rev.*, vol. 54, no. 8, pp. 647–648, 1938.

[88] J. L. Hartke, “The Three-Dimensional Poole-Fenkel Effect,” *J. Appl. Phys.*, vol. 39, no. 10, pp. 4871–4873, 1968.

[89] M. E. Stückelberger, “Hydrogenated Amorphous Silicon : Impact of Process Conditions on Material Properties and Solar Cell Efficiency,” Ecole Polytechnique Federale De Lausanne, 2014.

[90] P. Muralidharan, S. Bowden, S. M. Goodnick, and D. Vasileska, “Modeling of Silicon Heterojunction Solar Cells,” *Photovolt. Spec. Conf. (PVSC), 2016 IEEE 43rd*, pp. 3547–3551, 2016.

[91] F. Rossi, P. Poli, and C. Jacoboni, “Weighted Monte Carlo Approach to Electron Transport in Semiconductors,” *Semicond. Sci. Technol.*, vol. 7, pp. 1017–1035, 1992.

[92] M. A. Green, “Third Generation Photovoltaics: Solar Cells for 2020 and Beyond,” *Phys. E*, vol. 14, no. 1–2, pp. 65–70, 2002.

[93] G. S. Gautam, T. P. Senftle, N. Alidoust, and E. A. Carter, “Novel Solar Cell Materials : Insights from First-Principles,” *J. Phys. Chem. C*, vol. 122, pp. 27107–27126, 2018.

[94] S. Datta, “Nanoscale Device Modeling: The Green’s Function Method,” *Superlattices Microstruct.*, vol. 28, no. 4, pp. 253–278, 2000.

[95] M. Fischetti and S. Laux, “Monte Carlo Analysis of Electron Transport in Small Semiconductor Devices Including Band-Structure and Space-Charge Effects,” *Phys. Rev. B*, vol. 38, no. 14, pp. 9721–9745, 1988.

[96] M. Auf Der Maur, G. Penazzi, G. Romano, F. Sacconi, A. Pecchia, and A. Di Carlo, “The Multiscale Paradigm in Electronic Device Simulation,” *IEEE Trans. Electron Devices*, vol. 58, no. 5, pp. 1425–1432, 2011.

[97] W. E and B. Engquist, “Multiscale modeling and computation,” *Not. Am. Math Soc.*, vol. 50, no. 9, pp. 1062–1070, 2003.

[98] S. Urata and S. Li, “A Multiscale Model for Amorphous Materials,” *Comput. Mater. Sci.*, vol. 135, pp. 64–77, 2017.

[99] G. Bao, D. Liu, and S. Luo, “Multiscale Modeling and Computation of Optically Manipulated Nano Devices,” *J. Comput. Phys.*, vol. 316, pp. 558–572, 2016.

[100] D. H. Foster, T. Costa, M. Peszynska, and G. Schneider, "Multiscale Modeling of Solar Cells with Interface Phenomena," *J. Coupled Syst. Multiscale Dyn.*, vol. 1, no. 2, pp. 179–204, 2013.

[101] C. Falco, M. Porro, R. Sacco, and M. Verri, "Multiscale Modeling and Simulation of Organic Solar Cells," *Comput. Methods Appl. Mech. Eng.*, vol. 245–246, pp. 102–116, 2012.

[102] J. M. Higman, K. Hess, C. G. Hwang, and R. W. Dutton, "Coupled Monte Carlo-Drift Diffusion Analysis of Hot-Electron Effects in MOSFET's," *IEEE Trans. Electron Devices*, vol. 36, no. 5, pp. 930–937, 1989.

[103] F. Venturi, R. K. Smith, E. C. Sangiorgi, M. R. Pinto, and B. Ricco, "A General Purpose Device Simulator Coupling Poisson and Monte Carlo Transport with Applications to Deep Submicron MOSFET's," *IEEE Trans. Comput. Des. Integr. Circuits Syst.*, vol. 8, no. 4, pp. 360–369, 1989.

[104] H. Kosina and S. Selberherr, "A Hybrid Device Simulator that Combines Monte Carlo and Drift-Diffusion Analysis," *IEEE Trans. Comput. Des. Integr. Circuits Syst.*, vol. 13, no. 2, pp. 201–210, 1994.

[105] D. Y. Cheng, C. G. Hwag, and R. W. Dutton, "PISCES-MC: A Multiwindow, Multimethod 2-D Device Simulator," *IEEE Trans. Comput. Des. Integr. Circuits Syst.*, vol. 7, no. 9, 1988.

[106] P. T. Nguyen, D. H. Navon, and T. W. Tang, "Boundary Conditions in Regional Monte Carlo Device Analysis," *IEEE Trans. Electron Devices*, vol. 32, no. 4, pp. 783–787, 1985.

[107] S. E. Laux, "On Particle-Mesh Coupling in Monte Carlo Semiconductor Device Simulation," *IEEE Trans. Comput. Des. Integr. Circuits Syst.*, vol. 15, no. 10, pp. 1266–1277, 1996.

[108] R. J. Mills *et al.*, "Monte Carlo Simulation of Wide AlGaAs Barriers," *Proc. IEEE/Cornell Conf. Adv. Concepts High Speed Semicond. Devices Circuits*, pp. 448–457, 1993.

[109] S. Bandyopadhyay, M. E. Klausmeier-Brown, C. M. Maziar, S. Datta, and M. S. Lundstrom, "A Rigorous Technique to Couple Monte Carlo and Drift-Diffusion Models for Computationally Efficient Device Simulation," *IEEE Trans. Electron Devices*, vol. 34, no. 2, pp. 392–399, 1987.